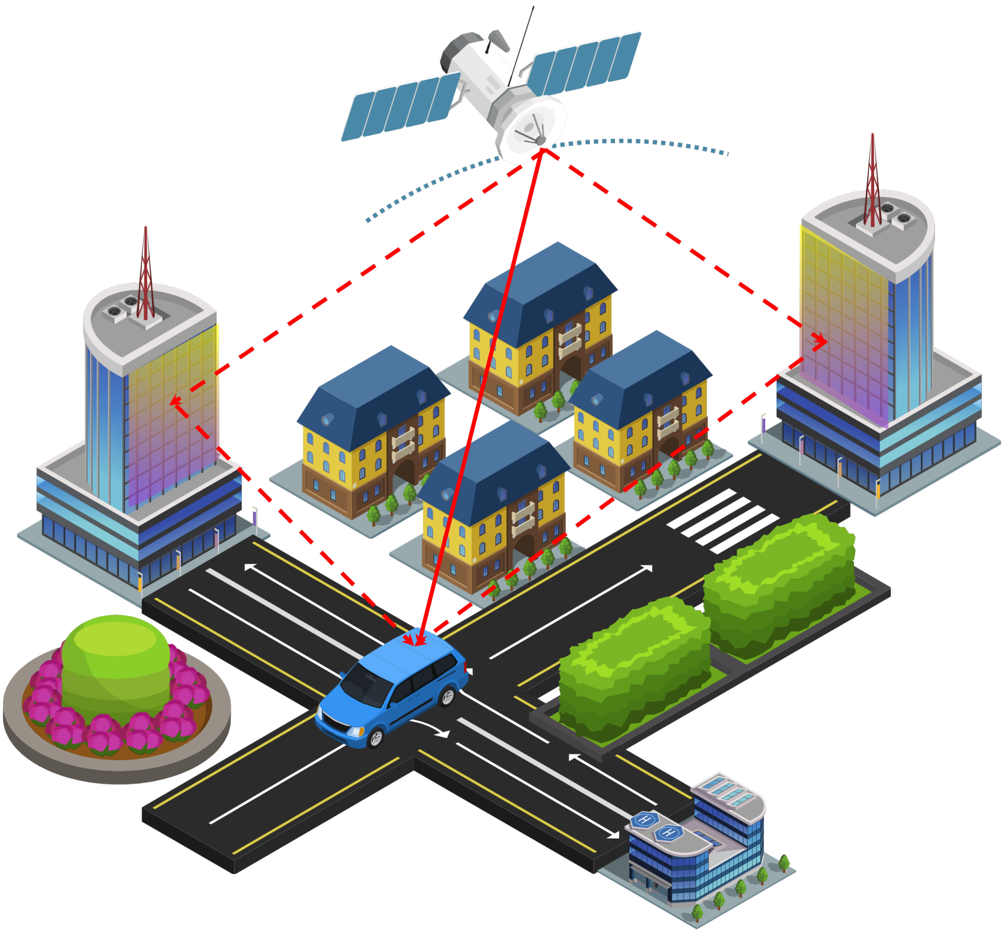

Localization via 6G LEO Satellites and RISs

Master's thesis in Information and Communication Technology

CI GAO

DEPARTMENT OF ELECTRICAL ENGINEERING
CHALMERS UNIVERSITY OF TECHNOLOGY
Gothenburg, Sweden 2026
www.chalmers.se

Master's thesis 2026

Localization via 6G LEO Satellites and RISs

CI GAO

Department of Electrical Engineering
Information Communication and Technology
Chalmers University of Technology
Gothenburg, Sweden 2026

Localization via 6G LEO Satellites and RISs
Ci Gao

Supervisor: Sharief Saleh, Department of Electrical Engineering
Examiner: Henk Wymeersch, Department of Electrical Engineering

Master's Thesis 2026
Department of of Electrical Engineering
Information Communication and Technology
Chalmers University of Technology
SE-412 96 Gothenburg
Telephone +46 31 772 1000

Typeset in LaTeX
Gothenburg, Sweden 2026

Localization via 6G LEO Satellites and RISs
CI GAO
Department of Electrical Engineering
Chalmers University of Technology

Abstract

Modern autonomous applications, such as intelligent transportation, unmanned aerial vehicles, and remote sensing systems, require accurate and uninterrupted positioning services. These requirements are no longer met via conventional satellite localization systems, such as the global navigation satellite system (GNSS), as they suffer from weak received signals which can be easily jammed and/or spoofed, limited geometric diversity, and severe blockage in complex propagation environments. Compared with GNSS, 6G low-earth-orbit (LEO) satellites can provide lower propagation delay, stronger received signals, and richer Doppler information due to the LEO orbit. However, LEO-satellite-based localization still faces significant challenges, particularly in single-LEO scenarios where the line-of-sight (LoS) signal may be weak, obstructed, or insufficient to provide reliable localization geometry. 6G's emerging reconfigurable intelligent surfaces (RISs) provide a promising solution by creating controllable reflected paths that can act as virtual anchors for localization. Although prior studies have investigated single-RIS-assisted LEO localization, the RIS-assisted path is usually weak and sensitive to noise and interference, which may cause severe performance degradation in low signal-to-noise-ratio (SNR) scenarios. To improve localization robustness, this thesis investigates a multi-RIS-assisted single-LEO localization framework. Multiple RISs are exploited to provide additional geometric constraints, while a joint positioning method is adopted to enhance positioning robustness. Moreover, a time-orthogonal RIS coding scheme is applied to separate different RIS branches and mitigate inter-RIS interference during channel parameter estimation. Simulation experiments are conducted to evaluate the localization performance of the proposed framework by comparing the theoretical Cramer–Rao bound (CRB) with the corresponding estimation results. The results demonstrate that double-RIS setup drops the 3D position error from 10^4 m level to 10 m level compared to single-RIS setup in low-SNR region, which provides a useful basis for future LEO-NTN localization systems.

Keywords: LEO localization, RIS, OFDM, Doppler, Fisher Information Matrix.

Acknowledgements

I would like to express my sincere gratitude to my supervisor, Sharief Saleh, for his valuable support, encouragement, and guidance throughout this project. His expertise and insightful advice have greatly deepened my understanding of the subject and played an important role in shaping the direction of this work.
I would also like to extend my appreciation to my examiner at the Department of Electrical Engineering, Henk Wymeersch, for his thoughtful feedback, constructive suggestions, and continuous encouragement throughout the project.

CI GAO, Gothenburg, June 2026

List of Acronyms

Below is the list of acronyms that have been used throughout this thesis listed in alphabetical order:

3GPP	third generation partnership project
6G	sixth generation
AoA	angle of arrival
AoD	angle of departure
AoD-H	angle of departure horizontal
AoD-V	angle of departure vertical
AWGN	additive white Gaussian noise
BL	bearing line
CFO	carrier frequency offset
CP	cyclic prefix
CRB	Cramér–Rao bound
CRLB	Cramér–Rao lower bound
FFT	fast Fourier transform
FIM	Fisher information matrix
GCS	global coordinate system
GEO	geostationary Earth orbit
GNSS	global navigation satellite system
HEO	highly elliptical orbit
IFFT	inverse fast Fourier transform
LCS	local coordinate system
LEO	low earth orbit
LoS	line-of-sight
MEO	medium earth orbit
MIMO	multiple-input multiple-output
ML	maximum likelihood
MLE	maximum likelihood estimation
MP	multipath component
NF	noise figure
NLoS	non-line-of-sight
NTN	non-terrestrial network
OFDM	orthogonal frequency division multiplexing
PNT	positioning, navigation, and timing

PSD	power spectral density
RCS	radar cross section
RIS	reconfigurable intelligent surface
RMSE	root mean square error
SNR	signal-to-noise ratio
SP	scatter point
STD	standard deviation
TDOA	time difference of arrival
TN	terrestrial network
TOA	time of arrival
TP	time positioning
UAV	unmanned aerial vehicle
UE	user equipment
URA	uniform rectangular array

Nomenclature

Below is the nomenclature of indices, sets, parameters, and variables that have been used throughout this thesis.

Indices

i, j	Generic indices for anchors, RIS bearing lines, or array elements
k	Subcarrier index, $k = 0, \ldots, K-1$
κ	Fast-time sample index after CP removal, $\kappa = 0, \ldots, K-1$
ℓ, l	OFDM symbol or slow-time index, $\ell, l = 0, \ldots, L-1$
$\tilde{\ell}$	OFDM symbol index within one time-orthogonal block
r	RIS index, $r \in \{1, 2\}$ for the double-RIS case
m	Multipath component or scatter-point index
n	RIS reflecting-element index
Γ	Index or number of time-orthogonal blocks

Sets

$\mathcal{R}$	Set of RISs
$\mathcal{K}$	Set of OFDM subcarriers
$\mathcal{L}$	Set of OFDM symbols
$\tilde{\mathcal{L}}$	Set of OFDM symbols within one time-orthogonal block
$\mathcal{N}_r$	Set of reflecting elements of the r-th RIS
$\mathcal{M}_0$	Set of direct satellite–scatter point–UE multipath components
$\mathcal{M}_r$	Set of RIS-related multipath components associated with the r-th RIS

Parameters

c	Speed of light
f_c	Carrier frequency
λ	Carrier wavelength, $\lambda = c/f_c$
Δf	OFDM subcarrier spacing
T	Useful OFDM symbol duration, $T = 1/\Delta f$
T_{CP}	Cyclic-prefix duration
T_{sym}	Total OFDM symbol duration
K	Number of OFDM subcarriers
L	Number of OFDM symbols
$\tilde{L}$	Number of OFDM symbols in one time-orthogonal block
Γ	Number of time-orthogonal time blocks
P_{tot}	Total transmit power
N_0	Thermal noise power spectral density
N_f	Receiver noise figure
σ^2	Receiver noise variance
σ^2_{eff}	Effective noise variance including Multipath power
P_{MP}	Average multipath-component power
h	LEO satellite orbital altitude
$\mathbf{p}_{\text{sat}}$	LEO satellite position
$\mathbf{v}_{\text{sat}}$	LEO satellite velocity vector
$\mathbf{p}_{R,r}$	Position of the r-th RIS
$\mathbf{R}_r$	Rotation matrix from the LCS of the r-th RIS to the GCS
$\mathbf{I}$	Identity matrix
$\mathbf{F}$	FFT matrix
$\mathbf{M}$	time-orthogonal code matrix for time-orthogonal RIS profile design
$m_{i,r}$	time-orthogonal code coefficient for the r-th RIS in the i-th block
$\boldsymbol{\omega}_{r,\ell}$	Phase-control vector of the r-th RIS during the ℓ-th OFDM symbol
$N_{x,r}$	Number of RIS elements along the local x-axis of the r-th RIS
$N_{z,r}$	Number of RIS elements along the local z-axis of the r-th RIS
N_r	Number of reflecting elements of the r-th RIS
d_{RIS}	RIS inter-element spacing
ϕ_x	Pitch angle of the RIS local coordinate system
ϕ_y	Roll angle of the RIS local coordinate system
ϕ_z	Yaw angle of the RIS local coordinate system

$\mathbf{R}_x(\phi_x)$	Rotation matrix with respect to the x-axis
$\mathbf{R}_y(\phi_y)$	Rotation matrix with respect to the y-axis
$\mathbf{R}_z(\phi_z)$	Rotation matrix with respect to the z-axis
M_0	Number of scatter points in direct satellite–scatter point–UE
M_r	Number of scatter points in the r-th RIS path
c_{RCS}	Scattering-strength parameter related to the radar cross section
$\mathbf{q}_{0,m}$	Position of the m-th direct scatter point
$\mathbf{q}_{r,m}$	Position of the m-th scatter point associated with the r-th RIS
γ_{th}	SNR threshold for joint positioning
R_{random}	Random position in the cluster disk
α_m	Random phase in the scatter path
PL	Total path Loss
PL_b	Basic path loss
PL_g	Attenuation due to atmospheric gases
PL_s	Attenuation caused by ionospheric or tropospheric scintillation
PL_e	Building entry loss
SF	Shadow fading
G_{e}	The RIS element radiation pattern
$\hat{\mathbf{n}}_r$	The broadside unit vector
A_{e}	The physical aperture
$d_{T,m}$	The distance between satellite and LoS scatter points
$d_{R,m}$	The distance between LoS scatter points and receiver
$d_{T,r,m}$	The distance between satellite and RIS scatter points
$w_{d,r}$	The weights of RIS distance measurement
$w_{\theta,r}$	The weights of RIS θ measurement

Variables

$\mathbf{p}$	Unknown UE position
$\hat{\mathbf{p}}$	Estimated UE position
$\hat{\mathbf{p}}_{\text{BL}}$	UE position estimated by bearing-line localization
$\hat{\mathbf{p}}_{\text{TP}}$	UE position estimated by delay-difference positioning
δ	Receiver clock bias or time offset
$\hat{\delta}$	Estimated receiver clock bias

δ_f	Carrier-frequency offset factor
$\hat{\delta}_f$	Estimated carrier-frequency offset factor
d_{su}	Satellite–UE distance
$d_{\text{sr},r}$	Satellite–r-th-RIS distance
$d_{\text{ru},r}$	r-th-RIS–UE distance
τ_{su}	LoS satellite–UE propagation delay
$\hat{\tau}_{\text{su}}$	Estimated LoS delay
$\tau_{\text{sr},r}$	Satellite–r-th-RIS propagation delay
$\tau_{\text{ru},r}$	r-th-RIS–UE propagation delay
$\hat{\tau}_{\text{ru},r}$	Estimated r-th-RIS–UE delay
$\tau_{\text{sru},r}$	Total satellite–r-th-RIS–UE path delay
ν_{su}	LoS Doppler factor
$\hat{\nu}_{\text{su}}$	Estimated LoS Doppler factor
$\nu_{\text{sr},r}$	Satellite–r-th-RIS Doppler factor
$\nu_{\text{ru},r}$	r-th-RIS–UE Doppler factor
$\nu_{\text{sru},r}$	Total Doppler factor of the r-th RIS-assisted path
α_{su}	Complex baseband channel coefficient of the LoS path
$\hat{\alpha}_{\text{su}}$	Estimated LoS complex channel coefficient
$\alpha_{\text{sru},r}$	Complex cascaded channel coefficient of the r-th RIS-assisted path
$\hat{\alpha}_{\text{sru},r}$	Estimated complex channel coefficient of the r-th RIS-assisted path
$\alpha_{\text{su},m}$	Complex channel coefficient of the m-th direct MP
$\alpha_{\text{sru},r,m}$	Complex channel coefficient of the m-th MP associated with the r-th RIS
ρ_{su}	Passband channel amplitude of the LoS path
$\rho_{\text{sru},r}$	Passband channel amplitude of the r-th RIS-assisted path
$\rho_{\text{su},m}$	Passband channel amplitude of the m-th direct MP
$\rho_{\text{sru},r,m}$	Passband channel amplitude of the m-th RIS-related MP
θ^{az}	Azimuth angle
θ^{el}	Elevation angle
$\theta_{\text{rs},r}$	Satellite-to-r-th-RIS AoA tuple
$\theta_{\text{ru},r}$	r-th-RIS-to-UE AoD tuple
$\hat{\theta}^{\text{az}}_{\text{ru},r}$	Estimated azimuth AoD of the r-th RIS path
$\hat{\theta}^{\text{el}}_{\text{ru},r}$	Estimated elevation AoD of the r-th RIS path
$\mathbf{u}(\theta^{\text{az}}, \theta^{\text{el}})$	Unit direction vector defined by azimuth and elevation
$\mathbf{u}'_r$	RIS-to-UE unit direction vector in the RIS LCS

$\mathbf{u}_r$	RIS-to-UE unit direction vector in the GCS
$\mathbf{a}_r(\cdot)$	Steering vector of the r-th RIS
$\mathbf{a}_{\mathrm{rx},r}$	RIS receive-side steering vector for the satellite-to-RIS link
$\mathbf{a}_{\mathrm{tx},r}$	RIS transmit-side steering vector for the RIS-to-UE link
$\mathbf{G}_{\mathrm{RIS},r,\ell}$	Effective response of the r-th RIS during the ℓ-th OFDM symbol
$\mathbf{G}_{\mathrm{RIS},r}$	Slow-time RIS response vector of the r-th RIS
$G^{MP}_{\mathrm{RIS},r,m\ell}$	Effective response of the r-th RIS in the scatter path during the ℓ-th OFDM symbol
$\mathbf{G}^{MP}_{\mathrm{RIS},r,m}$	Slow-time RIS response vector of the r-th RIS in the scatter path
$\mathbf{Y}$	Received OFDM signal matrix
$\mathbf{Y}_{\mathrm{res}}$	Residual signal matrix after LoS subtraction
$\bar{\mathbf{Y}}_{\mathrm{RIS}}$	Doppler-compensated RIS residual signal matrix
$\tilde{\mathbf{Y}}_{\mathrm{sru},r}$	time-orthogonal-decoded signal matrix of the r-th RIS branch
$\mathbf{Y}_{\mathrm{clean}}$	Signal matrix after subtracting reconstructed RIS components
$\mathbf{X}$	Pilot matrix
$x_{k,\ell}$	Pilot symbol on the k-th subcarrier and ℓ-th OFDM symbol
$\mathbf{N}$	Additive complex Gaussian noise matrix
$\mathbf{A}_i$	Fast-time Doppler matrix of path i
$\mathbf{B}_i$	Delay and inter-subcarrier Doppler matrix of path i
$\mathbf{C}_i$	Slow-time Doppler matrix of path i
$\mathbf{b}(\tau)$	Delay steering vector
$\mathbf{c}(\nu)$	Doppler steering vector
$\mathbf{z}(\tau,\nu)$	Vectorized delay-Doppler steering vector
$\mathbf{\Pi}_{\mathbf{z}}$	Projection matrix onto the subspace spanned by $\mathbf{z}$
$\mathbf{\Pi}^{\perp}_{\mathbf{z}}$	Orthogonal projection matrix onto the null space of $\mathbf{z}$
$\hat{\rho}_r$	Measured delay-difference range quantity associated with the r-th RIS
$\mathbf{P}_r$	Projection matrix for the r-th RIS bearing line
$\mathbf{I}_r$	Bearing line constructed from the r-th RIS AoD
$\mathbf{u}^{\mathrm{in}}_{r,m}$	Incident unit vectors in scatter RIS path
$\mathbf{u}^{\mathrm{out}}_{r}$	Outgoing unit vectors in scatter RIS path
$\xi^{\mathrm{MP}}_{r,m}$	Spatial frequency in scatter RIS path
$\zeta^{\mathrm{MP}}_{r,m}$	Spatial frequency in scatter RIS path

Contents

List of Figures

List of Tables

1

Introduction

1.1 Background

Satellite positioning has become an indispensable technology for navigation, communication, sensing, and location-related services. Conventional global navigation satellite system (GNSS) have been widely used for positioning, navigation, and timing (PNT) services [1]. However, GNSS-based positioning still faces several limitations in challenging environments. In urban canyons, indoor-like areas, and obstructed scenarios, GNSS signals may be severely blocked, attenuated, jammed, or spoofed [2, 3, 4, 5]. Moreover, due to the high orbital altitude of medium Earth orbit (MEO) satellites, GNSS signals usually arrive at the receiver with weak power. The relatively slow variation of GNSS satellite geometry also limits the available Doppler diversity, which may restrict localization robustness in future 6G scenarios requiring reliable positioning under weak or obstructed signal conditions [6, 7]. Fortunately, future 6G wireless systems are expected to support high reliability, low latency, global coverage, and the deep integration of communication, sensing, and localization [8, 9, 10, 11]. To achieve these objectives, non-terrestrial networks (NTNs) are regarded as a key component of 6G systems, since they can extend service coverage beyond the limitation of terrestrial networks (TNs) and provide continuous connectivity over wide geographical areas [12, 13, 14]. By integrating NTNs with TNs, future wireless systems are expected to support seamless and cross-regional communication and positioning services [12, 13, 15]. Among different NTN platforms shown in Fig. 1.1, low Earth orbit (LEO) satellites have recently attracted significant attention. Compared with conventional MEO GNSS satellites, LEO satellites are deployed at much lower orbital altitudes, which leads to shorter propagation distances, lower propagation delays, and improved received signal strength [2, 16]. In addition, the high orbital velocity of LEO satellites introduces strong Doppler dynamics over time and frequency. These Doppler characteristics can provide additional localization information and can be jointly exploited with time-delay and carrier-phase measurements [2, 6, 17]. Therefore, LEO satellites are promising not only as communication nodes in NTNs, but also as complementary or alternative localization sources for future PNT services [3, 7, 17]. Nevertheless, it's still a challenge to achieve accurate positioning using a single LEO satellite. Although a LEO satellite can provide useful delay and Doppler observations, the localization geometry offered by a single satellite is inherently limited. In particular, the direct line-of-sight (LoS) path alone may not provide sufficient geometric diversity for high-accuracy three-dimensional positioning, especially when the receiver clock

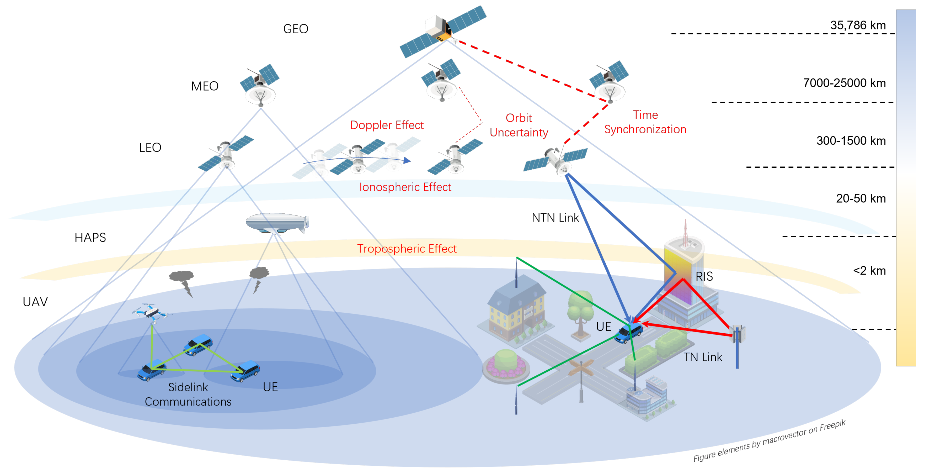

Figure 1.1: The illustration of NTN-TN integrated communication and position in 6G era [15].

bias and carrier-frequency offset need to be jointly estimated. Therefore, additional controllable propagation paths are required to improve the observability of the localization problem under a single-LEO condition. RIS has been recognized as another key enabling technology for 6G localization. By intelligently adjusting the phase or amplitude of reflected electromagnetic waves, RIS can reshape the wireless propagation environment and create controllable propagation paths [18, 19, 20, 21]. These RIS-reflected paths can provide additional delay and angular information, enhance coverage, and improve localization geometry [9, 18, 22]. Owing to its low cost, passive or nearly passive structure, and flexible deployment, RIS is particularly attractive in localization scenarios where the direct LoS path is weak, blocked, or geometrically insufficient [23, 24, 25]. The integration of LEO satellites and RISs is expected to benefit a wide range of future applications. For intelligent transportation and autonomous driving, RISs can be deployed on roadside units, traffic lights, or building facades to strenghthen LEO satellite signals and improve positioning reliability in urban blockage scenarios [9, 19, 26]. For emergency communications and disaster response, LEO satellites can provide wide-area connectivity, while RISs deployed on temporary platforms or unmanned aerial vehicles (UAVs) can strengthen reflected links and support high-accuracy localization when terrestrial infrastructure is unavailable or damaged [2, 3, 27]. Therefore, LEO-RIS integrated localization is a promising direction for future 6G-enabled PNT systems.

1.2 Related Work

1.2.1 LEO-Satellite-Based Localization

LEO-satellite-based localization has been extensively investigated in recent years. Compared with conventional GNSS satellites, LEO satellites operate at much lower orbital altitudes and move at significantly higher velocities. This fast orbital motion creates strong Doppler variations, which can be exploited together with time-delay

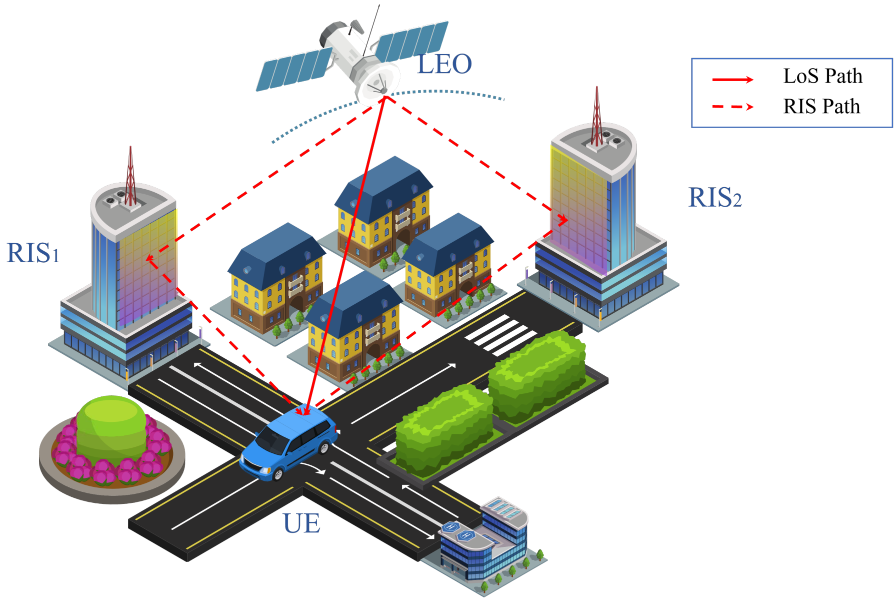

Figure 1.2: The 6G localization urban scenario using single LEO aided by multiple RISs [23].

and carrier-phase measurements for high-accuracy positioning. Existing studies have shown that LEO satellites can serve either as an enhancement to GNSS or as independent localization sources by using dedicated communication signals or opportunistic signals [7, 28, 29].
Existing LEO-based localization approaches can be broadly classified into two categories.

- The first category is based on signals-of-opportunity (SOP), where communication LEO satellites originally designed for non-navigation services are reused as opportunistic localization sources. Representative examples include commercial constellations such as Starlink, Orbcomm, Globalstar, and Iridium [30]. The main advantage of this approach is that it reuses already deployed satellite infrastructure, reducing the need for dedicated navigation payloads. However, opportunistic localization is challenging because the signal structure, timing information, ephemeris accuracy, and receiver access to proprietary system parameters may not be fully disclosed [15]. As a result, advanced receiver architectures and signal-processing methods are often required to extract useful localization observables from communication signals.
- The second category is based on dedicated LEO-PNT satellite constellations [31]. Unlike SOP-based methods, dedicated LEO-PNT systems are explicitly designed to provide navigation services from low Earth orbit. Representative commercial efforts include the PULSAR system from Xona Space Systems, the GeeSAT/GeeSpace system, and CentiSpace from Future Navigation [32, 33]. These systems are expected to broadcast navigation-related information such as ephemeris, clock bias, and clock-drift corrections. Their several signal structures, including GNSS-like signals, orthogonal frequency division multiplexing (OFDM), and chirp spread spectrum (CSS), are being investigated for LEO-

PNT applications.

Depending on the signal design and receiver capability, LEO satellite signals can provide several types of localization observables, including pseudorange, carrier phase, Doppler shift, AoA, andAoD [34].

- Pseudorange and carrier-phase measurements provide range-related information, but they require accurate timing, synchronization, and ambiguity handling.
- Doppler measurements are particularly informative in LEO systems because of the high satellite velocity, and they can support positioning and tracking even when timing information is limited.
- Angle-domain measurements can further improve observability when antenna arrays are available, but they increase receiver hardware complexity and require accurate array calibration.

To achieve those positioning methods, a common approach to improve LEO-based localization is to employ multiple satellites. Multi-LEO localization provides better geometric diversity and enables joint estimation of the user position, velocity, clock bias, and frequency offset through multiple independent delay-Doppler observations [3, 17]. However, this approach relies on the simultaneous visibility of multiple satellites. In dense urban, indoor-edge, or obstructed environments, the number of visible LEO satellites may be limited. Moreover, multi-satellite positioning increases system-level complexity because the receiver must model multiple satellite ephemerids, clock errors, Doppler dynamics, and inter-satellite measurement consistency [3, 29]. Therefore, high-accuracy localization under a single-LEO condition remains an important but challenging problem. The fundamental difficulty of single-LEO localization is the lack of geometric diversity. A single direct LoS path can provide useful delay and Doppler information, but these observations alone may not be sufficient to robustly resolve the user position, clock bias, and frequency-related uncertainties. This motivates the introduction of additional controllable propagation paths to enhance localization observability without requiring multiple simultaneously visible satellites [18, 23, 35].

1.2.2 RIS-Assisted Localization

RIS localization provides a promising solution for improving localization geometry, coverage, availability, and robustness in future integrated TN and NTN.

1.2.2.1 RIS function

A RIS can create a controllable reflected propagation path and can therefore be regarded as a virtual anchor with known position and configurable electromagnetic response [18, 35].

- By properly adjusting the phase or amplitude response of its reconfigurable elements, a RIS can provide additional positioning measurements, such as time of arrival (TOA), AoA, and AoD. These additional measurements are particularly useful when the LoS path is blocked, severely attenuated, or geometrically unfavorable.

- What's more, adding RIS-based measurements to the positioning filter can further improve localization accuracy by increasing the number of independent geometric constraints.
- Another important advantage of RIS technology is its ability to provide accurate angular information. Because a RIS consists of a large number of spatially distributed reconfigurable elements, beam sweeping or structured phase-profile design can be used to estimate both horizontal and vertical AoA/AoD [36]. Such angular measurements can support high-accuracy localization even in systems with limited antenna resources at the user equipment (UE), thereby reducing the requirement of deploying large antenna arrays at the receiver.
- Compared with deploying additional base stations, RISs can improve positioning geometry without introducing extra satellite clocks, base-station clocks bias, or carrier frequency offset (CFO), which is beneficial to reduce synchronization complexity and requires additional clock and frequency-offset calibration.

Therefore, RIS-enabled positioning can enhance localization performance with lower deployment and operation cost than adding new base stations. These properties make RIS a suitable technology for improving single-LEO localization, where the direct satellite path provides limited delay-Doppler information while the RIS paths provide additional delay and angle information.

1.2.2.2 RIS types

Within RIS localization, different RIS architectures can be considered depending on the required coverage, power consumption, hardware complexity, and propagation conditions [15]. The main types include:

- Passive RIS: reflects incident signals without power amplification. It is energy-efficient and low-cost, but its performance depends strongly on the strength of the incident signal.
- Active RIS: amplifies the reflected signal and can improve communication and localization performance under weak or degraded channel conditions, especially for NTN links. However, it requires additional power supply and introduces higher hardware complexity.
- Hybrid RIS: combines passive and active elements, aiming to balance the low-power advantage of passive RIS with the signal-enhancement capability of active RIS.
- STAR-RIS: also known as intelligent omni-surface, supports both reflection and transmission. Unlike conventional RIS, it can serve users on both sides of the surface, which is useful for extending terrestrial and non-terrestrial coverage to indoor or blocked areas.

1.2.2.3 Single RIS localization

In a single-LEO positioning system, the RIS path introduces additional propagation delay and angular information, which can compensate for the limited geometric information provided by the direct satellite-to-UE LoS path. In [23], the RIS single-LEO localization problem was investigated with one visible LEO satellite and one

RIS deployed near the UE. This work bridges conventional single-LEO localization and RIS localization by introducing one controllable reflected path to complement the direct satellite–UE LoS path. A comprehensive OFDM signal model was developed by accounting for receiver clock bias, CFO, and both slow-time and fast-time Doppler effects caused by the high mobility of the LEO satellites. A low-complexity multi-stage estimator was further proposed to estimate the LoS delay and Doppler first, subtract the reconstructed LoS component, and then estimate the RIS delay and AoD. This work [23] contributes an important benchmark for RIS single-LEO localization.

Nevertheless, single-RIS localization still has several limitations. First, a single RIS introduces only one additional positioning anchor. If the RIS position is geometrically unfavorable with respect to the satellite and the UE, the delay-angle constraints may still be weak. Second, the cascaded satellite-RIS-UE path usually experiences larger path loss than the LoS path, which makes the RIS path more sensitive to noise and multipath (MP) interference. Third, the improvement provided by a single RIS depends heavily on the quality of the estimated RIS channel parameters. These limitations indicate that simply adding one RIS may not be sufficient for robust high-accuracy localization in challenging single-LEO scenarios [18, 23, 37].

1.2.2.4 Multi-LEO and Multi-RIS Localization Method

To further improve geometric diversity, multiple RISs can be deployed as spatially separated positioning anchors. Compared with a single-RIS model, a multi-RIS system can provide multiple independent RIS paths with different delays, angles, and propagation geometries. In [38], a multi-LEO and multi-RIS localization framework was proposed for UE tracking. Different from single-LEO or single-RIS localization, this approach assumes that multiple LEO satellites and multiple terrestrial RISs are simultaneously available. The system exploits both satellite transmissions and RIS paths to provide richer channel observations and stronger geometric diversity. The localization problem in [38] is formulated as a high-dimensional user-tracking problem. Specifically, the unknown user state includes the 3D position, 3D velocity, and 3D orientation of the UE, leading to a 9D tracking problem. To handle this challenging state estimation problem, a tracking algorithm based on the unscented Kalman filter (UKF) and Riemannian manifold theory was developed. The UKF is used to deal with the nonlinear observation model and time-varying measurement uncertainty, while the Riemannian manifold formulation is adopted to properly represent and update the constrained orientation state. In the multi-LEO multi-RIS system considered in [38], the separation of different propagation paths mainly relies on orthogonal satellite multiplexing and the assumption of an efficient channel estimation process. Specifically, different LEO satellites are assigned orthogonal frequency resources so that their downlink pilot signals can be transmitted simultaneously without mutual interference. After pilot transmission, the receiver estimates the geometric channel parameters associated with the direct satellite–UE LoS paths and the RIS paths. Since the RISs are deployed at different locations and orientations, their RIS paths lead to different delay, Doppler, and angular characteristics in the channel-parameter domain. Thus, the different RIS paths are assumed to be separable by the channel estimator, rather than being explicitly separated by a

dedicated time-orthogonal RIS coding scheme in the later work. In [38], the MP effect is modeled through a statistical shadowed Rician channel model rather than explicit scatter paths. The LoS component is treated as a deterministic channel component, while the non-line-of-sight (NLoS) or MP component is modeled as a zero-mean Gaussian random term. This model is applied to the satellite–UE and RIS–UE channels, where both LoS and NLoS components may exist in the near-ground propagation environment. In contrast, the satellite–RIS channel is assumed to be LoS-only because the RISs are deployed at elevated positions and are considered to be far from near-ground clutter. The MP are treated as additive disturbance in the received signal and are incorporated into the observation uncertainty through the channel-parameter covariance.
However, this method relies on the simultaneous visibility of several LEO satellites and several RISs. This requirement imposes constraints on satellite constellation deployment, RIS infrastructure availability, and path visibility. This motivates the study of single-LEO multi-RIS localization, where multiple terrestrial RISs are used to compensate for the limited satellite visibility.

1.2.2.5 Multi-RIS Separation

In [39], different RIS paths are separated by using time-orthogonal RIS profiles in TN. Specifically, the transmission block is divided into several time blocks, and the LoS path and individual RIS paths are assigned mutually orthogonal temporal profiles. After receiving, orthogonal projection is applied to extract the observations associated with the LoS component and each RIS branch, enabling separate channel-parameter estimation for different paths. The MP components are modeled explicitly through a geometric channel model rather than represented by an implicit shadow-fading model. The received signal includes both LoS MP components and RIS MP components. These MP components are not exploited as additional positioning information in the proposed algorithm and regarded as effective noise. Instead, they are incorporated into the channel model and simulations to evaluate how unresolved scatter paths affect channel estimation and positioning accuracy. However, this work primarily focuses on TN base station localization and does not involve LEO satellite-assisted scenarios.

1.2.3 Comparison and Research Gap

Table 1.1 compares representative localization approaches in terms of the number of satellites, the number of RISs, the RIS-path separation strategy, and the MP model. The comparison shows that existing studies have addressed different parts of the problem, but a unified framework for single-LEO multi-RIS localization with RIS separation and explicit MP evaluation is still missing.
From Table 1.1, the research gap can be identified from three aspects. First, multi-LEO localization improves geometric diversity, but it relies on the simultaneous availability of multiple visible satellites, which may be difficult to satisfy in dense urban, indoor-edge, or obstructed environments. Second, single-RIS-assisted LEO localization reduces the dependence on multiple satellites, but it introduces only one additional virtual anchor, which is limited by its poor RIS geometry and weak

Table 1.1: Comparison of Related Localization Approaches.

Approach	**Satellite number**	**RIS number**	**RIS separation scheme**	**MP model**
Single-LEO localization [29]	One	No RIS	Not applicable.	Statistical channel models.
Multi-LEO localization [3, 17]	Multiple	No RIS	Not applicable.	Statistical channel models.
Single-RIS-assisted LEO localization [23]	One	One	No inter-RIS separation is required.	Not applicable
Multi-LEO multi-RIS tracking [38]	Multiple	Multiple	Satellites are separated by orthogonal frequency resources. Different RIS paths are assumed to be distinguishable through geometry and channel estimation.	Statistical shadowed Rician model. The NLoS/MP component is modeled as a zero-mean Gaussian random term.
Time-orthogonal multi-RIS sidelink positioning [39]	No LEO	Multiple	Uses time-orthogonal RIS profiles to explicitly separate the LoS path and individual RIS paths.	Explicit geometric MP model. Both LoS-related and RIS-related scatter paths are included.
This thesis	One visible LEO	Multiple	Uses time-orthogonal RIS coding to explicitly separate different RIS branches after Doppler compensation.	Explicit geometric MP model. LoS-related and RIS-related MP components are generated from geometric propagation routes.

RIS-path observability. Moreover, this model does not take MP into consideration. Third, for the multi-LEO multi-RIS model, it is necessary to develop an accurate channel estimator that can separate high-dimensional channel components while preserving the temporal synchronization and parameter consistency among different paths. Fourth, although time-orthogonal multi-RIS separation has been studied in TN sidelink positioning, directly extending it to LEO-NTN localization needs more efforts because the high satellite mobility introduces strong Doppler phase rotations. If these Doppler effects are not properly compensated, the orthogonality among different RIS profiles may be degraded. Fifth, most models adopt statistical channel models to describe MP, but the impact of explicit MP scatter paths on single-LEO multi-RIS localization has not been sufficiently investigated to evaluate the geometric disturbance for LoS and RIS paths. Therefore, the main gap addressed in this thesis is the lack of a unified localization framework for a single visible LEO satellite assisted by multiple time-orthogonally coded RISs under MP. Such a framework should jointly address Doppler compensation for LEO signals, multi-RIS branch separation, robust positioning using multiple virtual anchors, and explicit MP evaluation. This motivates the proposed double-RIS localization framework, where time-orthogonal RIS coding, Doppler compensation, staged channel estimation, joint positioning, and explicit scatter-path simulations are considered together.

1.3 Problem Statement

Multi-LEO localization can improve geometric diversity, but it relies on the simultaneous availability of multiple visible satellites. Single-RIS LEO localization reduces this requirement by introducing an additional controllable reflection path, but it provides only one virtual anchor and may still suffer from poor geometry or weak reflected-path observability. Although multi-RIS localization has been investigated in terrestrial or quasi-static scenarios, its application to LEO-NTN localization remains less explored, especially under high satellite mobility and strong Doppler effects. Similarly, time-orthogonal RIS coding has mainly been developed for TN localization or communication scenarios, where the power gap between the LoS and RIS-assisted paths is usually less severe. In a LEO-NTN scenario, the large propagation distance, high Doppler shift, and weak RIS-reflected signals make the separation of multiple RIS paths more challenging. Therefore, the design of time-orthogonal RIS profiles together with Doppler compensation requires further investigation. Finally, MP effects are often represented by statistical NLoS shadow-fading models, while fewer studies explicitly model scatter paths and analyze their impact on channel estimation and localization accuracy.

1.4 Thesis Objectives

To realize multi-RIS LEO localization under realistic propagation conditions, this thesis pursues the following five objectives:

- **Develop accurate channel models and build a simulation environment.** Construct a geometric and channel model in a multi-RIS single-LEO scenario which contains the LoS, RIS, and MP together with Doppler and CFO effects. Explicit MP is designed to evaluate the robustness of the proposed method.
- **Develop RIS configurations to resolve the path-association problem.** Design a time-orthogonal RIS coding scheme that distinguishes the RIS branches and suppresses inter-RIS interference.
- **Develop channel estimation algorithms to estimate channel parameters.** Build a staged channel estimation algorithm that extracts the LoS and RIS-branch parameters from the received signal to reduce the complexity of direct joint estimation algorithm.
- **Develop positioning algorithms.** Design a joint positioning method that combines bearing-line methods and delay-difference method to estimate the UE position, achieving more robust performance than the single-RIS setup.
- **Derive the Cramer–Rao bound.** Derive the Cramér–Rao bound (CRB) for channel parameter estimation and localization accuracy. root mean square error (RMSE)-based evaluation metrics are evaluated to the performance in the Monte Carlo.

1.5 Contributions

Based on the above research gap, the main contributions of this thesis are summarized as follows.

- *Multi-RIS single-LEO system model:* This thesis extends existing single-LEO and single-RIS localization models to a double-RIS single-LEO architecture. Different from the multi-LEO satellite localization, this method can exploit single visible satellite localization. What's more, the multiple RIS provides more localization information to improve performance compared to the single-RIS.

- *Time-orthogonal RIS branch separation:* This thesis applies time-orthogonal RIS coding to separate the two RIS branches at the receiver as well as improve the LoS delay estimation. Unlike the conventional encoding scheme, the proposed scheme is only applied to RIS paths because LoS path power is stronger than RIS branch power.
- *Staged channel-parameter estimation:* A staged estimator is developed to first estimate and subtract the dominant LoS component and then estimate the separated RIS branches. Compared with high-dimensional joint estimation, this staged approach reduces the search dimensionality and extracts the channel parameters by sequence. What's more, the second-stage refinement is operated to optimize the extracted channel parameters.
- *Joint positioning strategy:* This thesis combines bearing-line localization and delay-difference time positioning (TP) to build up joint positioning method through an signal-to-noise ratio (SNR)-dependent selection rule. The bearing-line solution is used when the RIS-path delay estimate is unreliable at low SNR, while the delay-difference solution is selected at higher SNR to exploit range-related information.
- *CRB benchmarking and multipath evaluation:* The thesis derives and numerically evaluates channel-domain and position-domain CRBs. The MP components are explicitly modeled to evaluate the robustness of the proposed localization framework under structured propagation interference. The complex path gains are treated as nuisance parameters, while the impact of MP is assessed through both Monte Carlo simulations and an effective-noise approximation in the CRB analysis.

1.6 Thesis Outline

The remainder of this thesis is organized as follows:

- **Chapter 2** introduces the fundamentals and theoretical background of the problem. It first describes different satellite orbits. Then, the device configurations for each component in the proposed model are explained in detail, followed by an introduction to geometric states and measurements. Next, channel parameters are introduced, followed by a general introduction to positioning methods.
- **Chapter 3** describes, in detail, the signal models used in this thesis. Specifically, it introduces the transmit signal model, the received passband signal model, the received baseband signal, the sampled received signal model, and the observations in compact matrix form. Finally, the chapter ends with a summary of the main assumptions of this work.
- **Chapter 4** describes the proposed method, including the channel-parameter estimation, time-orthogonal RIS coding scheme and the positioning method. The channel-parameter estimation features a staged-channel estimation framework, which sequentially processes LoS channel estimation, Doppler elimination, RIS decoding scheme, RIS branch channel estimation, and second-staged refinement. The time-orthogonal RIS coding scheme is introduced for the aim of encoding and decoding for RIS branch. The positioning method mainly explains the positioning methods, including bearing-line, delay-difference positioning, and joint

positioning.

- **Chapter 5** presents the simulation setup, the experiment evaluation metrics, and the numerical results. It compares the double-RIS setup with single-RIS setup to evaluate the performance of the proposed method. The MP effect is studied to explore the robustness of the proposed method. In addition, the ablation studies are conducted to validate the effectiveness of each key component, including the RIS AoD heatmap analysis, different positioning methods, and the RIS time-orthogonal coding scheme.
- **Chapter 6** summarizes the main findings and the existing limitations. Furthermore, it provides future directions to highlight several promising research directions as well as potential risk management for the future application.

2

Fundamentals

This section introduces the fundamental concepts and theoretical background in the subsequent system modeling and algorithm design. First, satellite orbits are systematically reviewed to explain their characteristics and application to motivate the use of LEO satellites. Second, the device configuration describes single-antenna UE, the LEO satellite transmit model and RIS introduction. Third, the geometric model is established to define the states of the user equipment, satellite, RIS, and multipath scatterers, together with the corresponding geometric measurements. Fourth, channel parameter are derived from the geometric model to build up the proposed positioning signal channel model. Fifth, we introduce several fundamental geometric positioning methods, providing the theoretical basis for the localization methods in the following chapters.

2.1 Satellite Orbit Classes

The Earth attracts many satellites by the laws of Kepler. There are several constraints in the space of Earth: the higher density of the atmosphere, debris caused by former launchers and satellites in the lower altitudes, and high-energy particles trapped in the Van Allen radiation belts located in approximately 2000 km and 8000 km. These factors affect the satellite orbits that can be used for the communication task. Satellite orbits can be divided into geostationary Earth orbit (GEO) and LEO satellites, MEO satellites, highly elliptical orbit (HEO) satellites [16], which is illustrated in Fig. 2.1, Table. 2.1 and Table. 2.2. LEO satellites are typically deployed

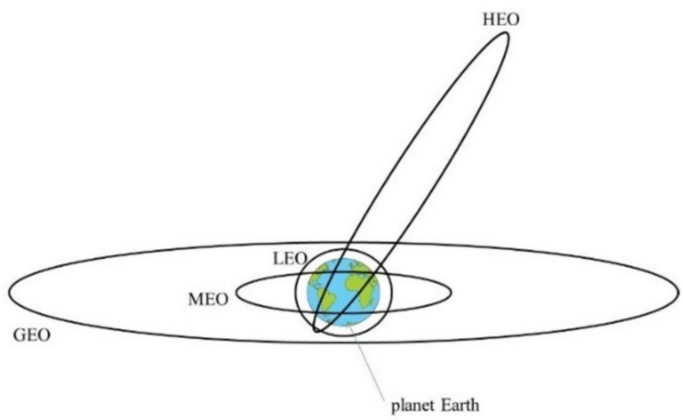

Figure 2.1: Illustration of the classes of orbits of satellites [16].

Table 2.1: Comparison of different satellite orbit classes [16].

Orbit	Typical altitude	Coverage characteristic
GEO	35786 km	Very large continuous regional coverage
LEO	500–2000 km	Small coverage per satellite; large constellation required
MEO	8000–20000 km	Medium to large coverage; fewer satellites than LEO needed
HEO	7000 – 45000 km	Long-duration coverage near apogee, especially for high-latitude regions

Table 2.2: UE-to-satellite propagation delay for different satellite orbit classes [16].

Orbit	UE to Satellite Delay [ms]		Max Propagation Delay [ms]
	Min	Max	
LEO	3	15	30
MEO	27	43	90
GEO	120	140	280

at altitudes between 500 km and 2000 km and the inclination angle of the orbital plane ranging from 0 to more than 90 degrees, providing a low propagation delay and relatively strong received signals. But their coverage area per satellite is limited and their high orbital velocity introduces significant Doppler effects. Their constellations are employed above the International Space Station and below the first Van Allen belt. GEO satellites are located in the equatorial plane at an altitude of approximately 35786 km. Since their orbital angular velocity is equal to the Earth's rotation rate, they appear still with respect to the Earth surface. MEO satellites are deployed at higher altitudes, typically between 8000 km and 20000 km, usually above the Van Allen belts. The inclination angles of the orbital plane range from 0 to more than 90 degrees. GNSSs, like GPS, Galileo and Beidou Navigation Satellite System, are developed based on the MEO satellite constellations. HEO satellites use highly elliptical orbits, whose operational altitude can range from around 7000 km to more than 45000 km. The propagation delay associated with the UE-to-satellite link varies significantly with the satellite altitude. In general, LEO satellites provide the lowest propagation delay due to their relatively low orbital altitude, while GEO satellites introduce the largest delay because of their much longer propagation distance. The typical UE-to-satellite propagation delays for different satellite orbits are summarized in Table 2.2.

Table 2.3: LEO satellite system-level parameters [16].

Parameter	**LEO**
Satellite orbit	LEO-600
Satellite altitude	600 km
Frequency band	S-band, 2 GHz
Equivalent satellite antenna aperture	2 m
Satellite EIRP density	34 dBW/MHz
Satellite Tx max gain	30 dBi
3-dB beamwidth	4.4127°
Satellite beam diameter	50 km

2.2 Device Configuration

2.2.1 UE Configuration

We consider a single UE equipped with an omnidirectional single antenna. The UE is located in the vicinity of the RIS and receives both the direct LoS signal from the LEO satellite and the RIS-assisted signal and additive noise. Since the UE is equipped with only one antenna, there is no array response at the UE to extract AoA information. This single-antenna UE configuration makes the localization problem more challenging, as spatial information must be inferred indirectly from the RIS paths rather than from a receiver antenna array. Therefore, the estimated UE position of the UE is mainly obtained from the delay, Doppler, and RIS-induced angular features of the received signal.

2.2.2 LEO Satellite Configuration

In this work, the LEO satellite is configured according to the Third Generation Partnership Project (3GPP) NTN Set-1 LEO-600 S-band reference scenario. Specifically, we consider the LEO Scenario C1, where the satellite adopts a transparent payload and earth-fixed steerable beams. The satellite altitude is set to 600 km, and the service link operates in the S-band with carrier frequency $f_c = 2$ GHz. According to the Set-1 LEO-600 S-band configuration, the equivalent satellite antenna aperture is $D_{\mathrm{sat}} = 2$ m, the satellite equivalent isotropically radiated power (EIRP) density is 34 dBW/MHz, and the satellite transmit maximum antenna gain is $G_{\max} = 30$ dBi. The corresponding 3 dB beamwidth is $\theta_{3\mathrm{dB}} = 4.4127°$, and the nadir-pointing satellite beam diameter is approximately 50 km. The satellite is modeled as a directional transmitter with a fixed maximum antenna gain. This directional antenna gain represents the main-beam gain of the LEO satellite antenna. In the considered simulation, the detailed antenna pattern, sidelobe structure, and satellite attitude dynamics are not explicitly modeled. Instead, the steerable earth-fixed beam is assumed to be properly pointed toward the service area during the observation interval, and its beam-pointing effect is absorbed into the fixed maximum gain and EIRP-density model.

A simplified satellite orbit model is adopted to generate physically meaningful range

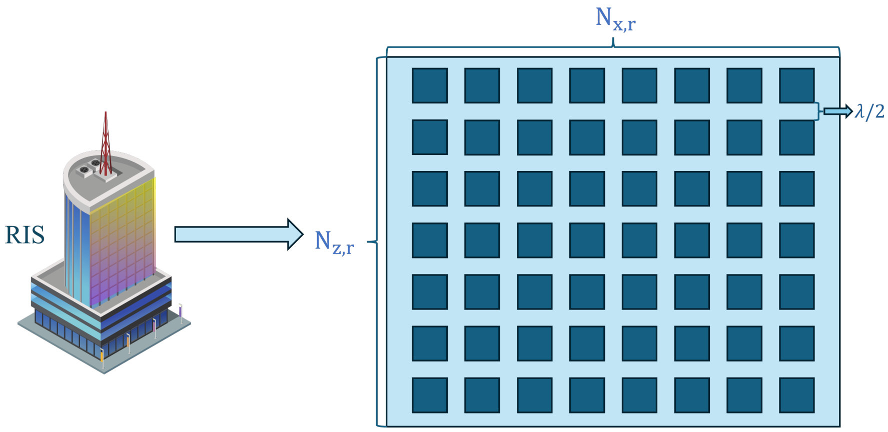

Figure 2.2: The URA RIS layout.

and Doppler measurements, which takes the satellite orbital altitude h, the Earth radius R and the initial azimuth-elevation angle tuple $\boldsymbol{\theta}_{\text{sat}} = (\theta_{\text{sat}}^{\text{az}}, \theta_{\text{sat}}^{\text{el}})$ as inputs, and outputs the satellite position and velocity vectors.

$$\mathbf{p}_{\text{sat}}(t) = d_{\text{sat}}(t)\mathbf{u}\Big(\boldsymbol{\theta}_{\text{sat}}(t)\Big), \tag{2.1}$$

$$d_{\text{sat}}(t) = R\sin\left(-\theta_{\text{sat}}^{\text{el}}(t)\right) + \sqrt{R^2\sin^2\left(-\theta_{\text{sat}}^{\text{el}}(t)\right) + 2Rh + h^2}. \tag{2.2}$$

$$\mathbf{v}_{\text{sat}}(t) = \dot{d}_{\text{sat}}(t)\mathbf{u}\Big(\boldsymbol{\theta}_{\text{sat}}(t)\Big) + d_{\text{sat}}(t)\dot{\mathbf{u}}\Big(\boldsymbol{\theta}_{\text{sat}}(t)\Big), \tag{2.3}$$

$\mathbf{p}_{\text{sat}}(t)$ denotes the satellite position at time t. $d_{\text{sat}}(t)$ is the distance between UE and the LEO satellite. $\mathbf{u}(\boldsymbol{\theta}_{\text{sat}}(t))$is the unit direction vector from LEO satellites. $\mathbf{v}_{\text{sat}}(t)$ is the satellite velocity with respect to time. $\dot{d}_{\text{sat}}(t)$ and $\dot{\mathbf{u}}(\boldsymbol{\theta}_{\text{sat}}(t))$ denote the time derivatives of the distance and the unit direction vector, respectively.

2.2.3 RIS Configuration

2.2.3.1 RIS Elements

Each RIS employs a uniform rectangular array (URA) as shown in Fig. 2.2. The number of reflecting elements of the rth RIS is

$$N_r = N_{x,r}N_{z,r}, \quad r \in \{1, 2\}, \tag{2.4}$$

where $N_{x,r}$ and $N_{z,r}$ denote the numbers of elements along the local x- and z-axes, respectively. In the simulations, both RISs use $N_{x,r} = N_{z,r} = 10$, and thus each RIS contains $N = 100$ reflecting elements. The carrier wavelength is $\lambda = \frac{c}{f_c}$, and the inter-element spacing is set to $\lambda/2$. The position of the (i, j)th RIS element of the rth RIS is

$$\mathbf{p}_{r,i,j} = \begin{bmatrix} x_{r,i} \\ 0 \\ z_{r,j} \end{bmatrix}, \tag{2.5}$$

where

$$x_{r,i} = \left(i - \frac{N_{x,r}-1}{2}\right)\frac{\lambda}{2}, \quad i = 0, \ldots, N_{x,r} - 1, \tag{2.6}$$

and

$$z_{r,j} = \left(j - \frac{N_{z,r} - 1}{2}\right)\frac{\lambda}{2}, \quad j = 0, \ldots, N_{z,r} - 1. \tag{2.7}$$

2.2.3.2 Profile Configuration

For n RIS element in rth RIS, the RIS controllanle delay $\tau_{n,r}$ is defined by

$$\tau_{r,n} \in \left[0, \frac{1}{f_c}\right]. \tag{2.8}$$

Thus, the corresponding phase shift is given by

$$\omega_{r,n} = -2\pi f_c \tau_{r,n}, \quad \omega_{r,n} \in [-2\pi, 0]. \tag{2.9}$$

Combining all N_r RIS elements, the RIS configuration vector is expressed as

$$\boldsymbol{\omega_r} = [e^{\jmath\omega_{r,1}}, e^{\jmath\omega_{r,2}}, \ldots, e^{\jmath\omega_{r,N_r}}]^\top \in \mathbb{C}^N. \tag{2.10}$$

Every elements in the RIS configuration vector has unit modulus with the controlled phase, which can adjust the expected signal direction to improve the signal

$$|[\boldsymbol{\omega}]_{r,n}| = 1, \quad \forall n. \tag{2.11}$$

The time-varying RIS configuration vector is given by

$$\boldsymbol{\omega_r}(t) = \left[e^{-\jmath 2\pi f_c \tau_{r,1}(t)}, e^{-\jmath 2\pi f_c \tau_{r,2}(t)}, \ldots, e^{-\jmath 2\pi f_c \tau_{r,N}(t)}\right]^\top. \tag{2.12}$$

2.3 Geometric Model

2.3.1 States

We consider a three-dimensional LEO satellite localization system consisting of one LEO satellite, one approximately static UE, and several RISs [23, 18, 39]. The unknown UE position with three unknown parameters is denoted by

$$\mathbf{p} \in \mathbb{R}^3. \tag{2.13}$$

The known positions of RISs, similarly defined by three parameters, are denoted by

$$\mathbf{p}_{R,r} \in \mathbb{R}^3, \quad r \in \{1, 2\}, \tag{2.14}$$

where r defines the index of RISs and in this experiment $r \in 1, 2$ is defined by two to illustrate. The position of the LEO satellite is defined by

$$\mathbf{p}_{sat} \in \mathbb{R}^3. \tag{2.15}$$

Within a short observation interval, the LEO satellite is assumed to move with approximately constant velocity. Its position is given by

$$\mathbf{p}_{\text{sat}}(t) = \mathbf{p}_{\text{sat}}(0) + t\mathbf{v}_{\text{sat}}, \tag{2.16}$$

where $\mathbf{v}_{\text{sat}}$ is the satellite velocity.
The satellite and UE clocks are assumed to be asynchronous, characterized by an unknown time offset δ and an unknown CFO δ_f. In addition to the deterministic LoS and RIS paths, MPs are introduced through scatter points (SPs). In this work, the MP propagation is not modeled through an implicit NLoS shadow-fading term. Instead, explicit scatter paths are introduced into the received signal. Specifically, the scatter points are generated around predefined cluster centers, and each MP component is constructed according to its geometric propagation route, including its delay, Doppler factor, and path gain. Based on the defined assumption, these MPs are modeled as single-bounce scattering paths added in the received signal. Let M_0 denote the number of LoS MP paths (satellite–SP–UE), and let M_r denote the number of scatter paths in the rth RIS path (satellite–SP–RIS–UE). The position of the mth scatter point corresponding to the LoS MP path is denoted by

$$\mathbf{q}_{0,m} \in \mathbb{R}^3, \quad m = 1, \ldots, M_0. \tag{2.17}$$

In the RIS MP paths, the position of the mth scatter point associated with the rth RIS is denoted by

$$\mathbf{q}_{r,m} \in \mathbb{R}^3, \quad r \in \{1, 2\}, \quad m = 1, \ldots, M_r. \tag{2.18}$$

The SPs are randomly generated around cluster centers [9]. The SP is generated as

$$\mathbf{q} = \mathbf{p}_c + R_{random} \begin{bmatrix} \cos \alpha_m \\ 0 \\ \sin \alpha_m \end{bmatrix}, \tag{2.19}$$

where $\mathbf{p}_c$ denotes the center of the scatter cluster, R_{random} denotes the random position in the disk and α_m denotes the random phase. The R_{random} is defined by the the cluster radius R_{c} following random distribution.

$$R_{random} = R_{\text{c}}\sqrt{u}, \quad u \sim \mathcal{U}(0, 1), \tag{2.20}$$

and

$$\alpha_m \sim \mathcal{U}(0, 2\pi). \tag{2.21}$$

This construction uniformly distributes the SPs inside a horizontal disk in the global x-z plane, while y is determined by the corresponding cluster center shown in Fig. 2.3.

2.3.2 Geometric Measurement

The local coordinate system (LCS) is related to the orientation angles of three axes, known as the pitch ϕ_x, roll ϕ_y, and yaw ϕ_z, respectively, to the x, y, and z axes.

- The pitch angle ϕ_x denotes the vertical tilt between the y-axis of the LCS and the xy-plane of the global coordinate system (GCS). Its positive or negative values denote the upward or downward trend of the antenna array, respectively.
- The roll angle ϕ_y denotes the vertical tilt between the x-axis of the LCS and the xy-plane of the GCS. The positive roll angle denotes the counterclockwise rotation along the antenna array y-axis.

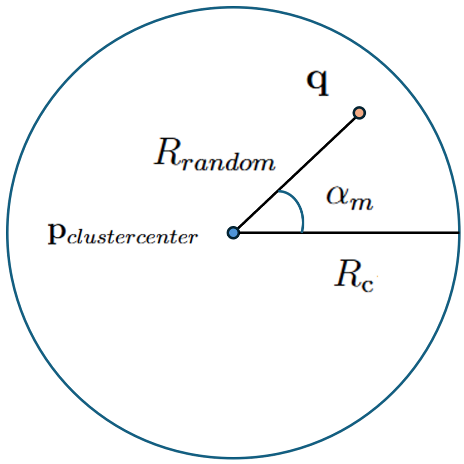

Figure 2.3: The SP position diagram on the x-z plane.

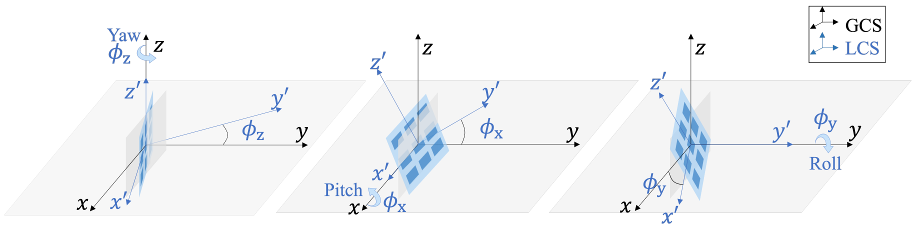

Figure 2.4: Three rotation positive angles of RIS antenna array [15].

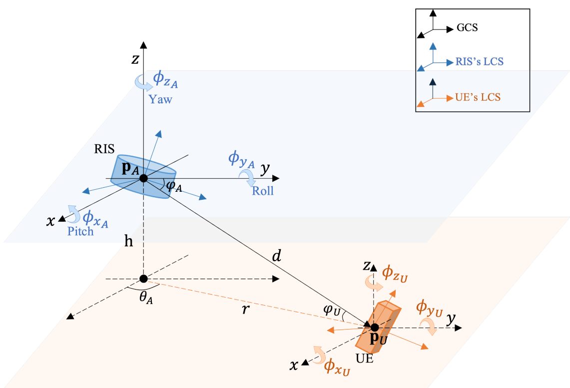

Figure 2.5: The elevation and azimuth angles [15].

- The yaw angle ϕ_z denotes the horizontal tilt between the y-axis of the LCS and the y-axis of the GCS. The positive yaw angle denotes the westward direction of the antenna array.

The translation from LCS to GCS can be represented by orientation $R(\phi_x, \phi_y, \phi_z)$. The standard order of applying matrices is usually listed as follows: roll angle, pitch angle, and yaw angle.

$$\mathbf{R}_x(\phi_x) = \begin{bmatrix} 1 & 0 & 0 \\ 0 & \cos\phi_x & -\sin\phi_x \\ 0 & \sin\phi_x & \cos\phi_x \end{bmatrix}, \tag{2.22}$$

$$\mathbf{R}_y(\phi_y) = \begin{bmatrix} \cos\phi_y & 0 & \sin\phi_y \\ 0 & 1 & 0 \\ -\sin\phi_y & 0 & \cos\phi_y \end{bmatrix}. \tag{2.23}$$

$$\mathbf{R}_z(\phi_z) = \begin{bmatrix} \cos\phi_z & -\sin\phi_z & 0 \\ \sin\phi_z & \cos\phi_z & 0 \\ 0 & 0 & 1 \end{bmatrix} \tag{2.24}$$

$$\mathbf{R}(\phi_\mathbf{x}, \phi_\mathbf{y}, \phi_\mathbf{z}) = \mathbf{R}_z(\phi_z)\mathbf{R}_x(\phi_x)\mathbf{R}_y(\phi_y). \tag{2.25}$$

The LoS vector between the rth RIS and the UE in the GCS is shown in Fig. 2.5, where $\mathbf{p}_{R,r} = [x_{R,r}, y_{R,r}, z_{R,r}]^T$ and $\mathbf{p} = [x, y, z]^T$ denote the positions of the rth RIS and the UE, respectively. The three-dimensional distance between them is denoted by $d_{\mathrm{ru},r} = \|\mathbf{p} - \mathbf{p}_{R,r}\|$:

$$d_{\mathrm{ru},r} = \|\mathbf{p} - \mathbf{p}_{R,r}\| = \sqrt{(x - x_{R,r})^2 + (y - y_{R,r})^2 + (z - z_{R,r})^2}. \tag{2.26}$$

The geometric angles $\theta_{ru,r}$ in the GCS, with respect to the rth RIS, can be expressed as

$$\theta_{ru,r} = \begin{bmatrix} \operatorname{atan2}\left(y - y_{R,r},\ x - x_{R,r}\right) \\ \sin^{-1}\left(\dfrac{z - z_{R,r}}{d_{\mathrm{ru},r}}\right) \end{bmatrix}, \tag{2.27}$$

2.4 Channel Parameters

2.4.1 Delay

Based on the last section's geometric parameters, the distance, delay, and Doppler information can be computed as follows: The LoS distance between the satellite and the UE is

$$d_{\mathrm{su}} = \|\mathbf{p} - \mathbf{p}_{\mathrm{sat}}\|. \tag{2.28}$$

The corresponding propagation delay τ_{su} is

$$\tau_{\mathrm{su}} = \frac{d_{\mathrm{su}}}{c} + \delta = \frac{\|\mathbf{p} - \mathbf{p}_{\mathrm{sat}}\|}{c} + \delta, \tag{2.29}$$

where c is the speed of light, δ is the unknown time offset. The rth RIS path parameters can be modeled as follows: The distance between the satellite and the rth RIS is:

$$d_{\mathrm{sr},r} = \left\| \mathbf{p}_{\mathrm{sat}} - \mathbf{p}_{R,r} \right\|, \tag{2.30}$$

Similarly the distance between rth RIS and UE is:

$$d_{\mathrm{ru},r} = \left\| \mathbf{p} - \mathbf{p}_{R,r} \right\|. \tag{2.31}$$

Based on the distance parameters, the delay parameters of each part are listed:

$$\tau_{\mathrm{sr},r} = \frac{d_{\mathrm{sr},r}}{c}, \tag{2.32}$$

$$\tau_{\mathrm{ru},r} = \frac{d_{\mathrm{ru},r}}{c} + \delta. \tag{2.33}$$

The total delay of rth RIS path $\tau_{\mathrm{sru},r}$ is:

$$\tau_{\mathrm{sru},r} = \tau_{\mathrm{sr},r} + \tau_{\mathrm{ru},r} = \frac{d_{\mathrm{sr},r}}{c} + \frac{d_{\mathrm{ru},r}}{c} + \delta = \frac{\left\| \mathbf{p}_{\mathrm{sat}} - \mathbf{p}_{R,r} \right\|}{c} + \frac{\left\| \mathbf{p} - \mathbf{p}_{R,r} \right\|}{c} + \delta \tag{2.34}$$

Scatter points are randomly generated around given cluster centers in equation 2.19 For the mth scatter paths in LoS path, they are defined:

$$d_{T,m} = \left\| \mathbf{p}_{\mathrm{sat}} - \mathbf{q}_{0,m} \right\|, \tag{2.35}$$

and

$$d_{R,m} = \left\| \mathbf{p} - \mathbf{q}_{0,m} \right\|. \tag{2.36}$$

.
The direct scatter path in the LoS path can be expressed as:

$$\tau_{su,m} = \frac{d_{T,m} + d_{R,m}}{c} + \delta = \frac{\left\| \mathbf{p}_{\mathrm{sat}} - \mathbf{q}_{0,m} \right\| + \left\| \mathbf{p} - \mathbf{q}_{0,m} \right\|}{c} + \delta. \tag{2.37}$$

For mth scatter path in RISpath, the parameters are listed:

$$d_{T,r,m} = \left\| \mathbf{p}_{\mathrm{sat}} - \mathbf{q}_{r,m} \right\|, \qquad d_{R,r,m} = \left\| \mathbf{q}_{r,m} - \mathbf{p}_{R,r} \right\|. \tag{2.38}$$

The scatter path in the RIS paths can be expressed:

$$\begin{aligned} \tau_{sru,r,m} &= \frac{d_{T,r,m} + d_{R,r,m} + d_{\mathrm{ru},r}}{c} + \delta \\ &= \frac{\left\| \mathbf{p}_{\mathrm{sat}} - \mathbf{q}_{r,m} \right\| + \left\| \mathbf{q}_{r,m} - \mathbf{p}_{R,r} \right\| + \left\| \mathbf{p} - \mathbf{p}_{R,r} \right\|}{c} + \delta \end{aligned} \tag{2.39}$$

For the

2.4.2 Doppler

To calculate the LoS Doppler ν_{su}, the following formula can be modeled:

$$\nu_{\text{su}} = \frac{\mathbf{v}_{\text{sat}}^T(\mathbf{p} - \mathbf{p}_{\text{sat}})}{c \left\| \mathbf{p} - \mathbf{p}_{\text{sat}} \right\|} + \delta_f. \tag{2.40}$$

The Doppler of rth RIS path $\nu_{\text{sru},r}$ can also be modeled as follow:

$$\nu_{\text{sr},r} = -\frac{\mathbf{v}_{\text{sat}}^T \mathbf{R}_r \mathbf{u}(\theta'_{rs,r})}{c}, \tag{2.41}$$

where $\mathbf{R}_r$ denotes the rth RIS rotation matrix, which is constructed from the yaw, pitch, and roll rotation, which denotes the rth RIS rotation transfer from the LCS of the RIS to the GCS. $u(\theta)$ denotes the rth RIS unit direction vector. In this work, the RISs and UE are determined static so the Doppler $\nu_{\text{ru},r}$ only includes unknown CFO:

$$\nu_{\text{ru},r} = \delta_f, \tag{2.42}$$

The total rth RIS path Doppler $\nu_{\text{sru},r}$ is defined:

$$\nu_{\text{sru},r} = \nu_{\text{sr},r} + \nu_{\text{ru},r} = -\frac{\mathbf{v}_{\text{sat}}^T \mathbf{R}_r \mathbf{u}(\theta'_{rs,r})}{c} + \delta_f, \tag{2.43}$$

For the LoS MP generated by the mth scatter point $\mathbf{q}_{0,m}$, the corresponding propagation path is satellite $\rightarrow$ $\text{SP}_{0,m}$ $\rightarrow$ UE. Since both the scatter point and the UE are assumed to be static during the observation interval, the Doppler of the scatter path is only induced by the satellite-to-SP part. Therefore, the total Doppler factor of the mth direct MPC is modeled as

$$\nu_{su,m} = \frac{\mathbf{v}_{\text{sat}}^T \left(\mathbf{q}_{0,m} - \mathbf{p}_{\text{sat}}\right)}{c \left\| \mathbf{q}_{0,m} - \mathbf{p}_{\text{sat}} \right\|} + \delta_f, \quad m = 1, \ldots, M_0, \tag{2.44}$$

For the scatter path in the rth RIS, the propagation path is satellite $\rightarrow$ $\text{SP}_{r,m}$ $\rightarrow$ RIS_r $\rightarrow$ UE. Similarly, since the SP, RIS, and UE are assumed static, the Doppler factor is approximated by the Doppler induced by the satellite-to-SP segment plus the CFO. Thus, the total Doppler factor of the mth scatter path in the rth RIS is written as

$$\nu_{sru,r,m} = \frac{\mathbf{v}_{\text{sat}}^T \left(\mathbf{q}_{r,m} - \mathbf{p}_{\text{sat}}\right)}{c \left\| \mathbf{q}_{r,m} - \mathbf{p}_{\text{sat}} \right\|} + \delta_f, \quad r \in \{1, 2\}, \quad m = 1, \ldots, M_r. \tag{2.45}$$

2.4.3 Angles

For the rth RIS, the RIS-to-satellite incident vector and the RIS-to-UE outgoing vector are shown in Fig. 2.6

$$\Delta\mathbf{p}_{\text{rs},r} = \mathbf{p}_{\text{sat}} - \mathbf{p}_{R,r} \tag{2.46}$$

and

$$\Delta\mathbf{p}_{\text{ru},r} = \mathbf{p} - \mathbf{p}_{R,r} \tag{2.47}$$

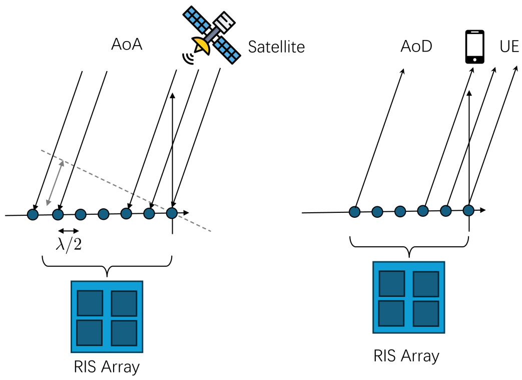

Figure 2.6: The illustation of AoA and AoD in the RIS scenario.

respectively. Their local-coordinate representations for AoA and AoD are

$$\theta'_{rs,r} = \begin{bmatrix} \tan^{-1}\left(\frac{[R_r^T(\Delta\mathbf{p}_{\mathrm{rs},r})]_2}{[R_r^T(\Delta\mathbf{p}_{\mathrm{rs},r})]_1}\right) \\ \sin^{-1}\left(\frac{[R_r^T(\Delta\mathbf{p}_{\mathrm{rs},r})]_3}{||\Delta\mathbf{p}_{\mathrm{rs},r}||}\right) \end{bmatrix}. \tag{2.48}$$

$$\theta'_{ru,r} = \begin{bmatrix} \tan^{-1}\left(\frac{[R_r^T(\Delta\mathbf{p}_{\mathrm{ru},r})]_2}{[R_r^T(\Delta\mathbf{p}_{\mathrm{ru},r})]_1}\right) \\ \sin^{-1}\left(\frac{[R_r^T(\Delta\mathbf{p}_{\mathrm{ru},r})]_3}{||\Delta\mathbf{p}_{\mathrm{ru},r}||}\right) \end{bmatrix}. \tag{2.49}$$

When RIS is considered the starting point, $\boldsymbol{\theta}'_{\mathrm{rs},r}$ denotes the incident angle LoS from the satellite to the rth RIS while $\boldsymbol{\theta}'_{\mathrm{ru},r}$ denotes the outgoing AoD from the rth RIS to the UE. For the MP in the RIS path, the incident direction is determined by the corresponding scatter point rather than by the satellite position. Therefore, the incident direction of the scatter-path should be modeled separately. For the scatter path in the mth scatter point of the rth RIS, the incident and outgoing unit vectors are given by

$$\mathbf{u}_{r,m}^{\mathrm{in}} = \mathbf{R}_r^T \frac{\mathbf{q}_{r,m} - \mathbf{p}_{R,r}}{\|\mathbf{q}_{r,m} - \mathbf{p}_{R,r}\|}, \tag{2.50}$$

and

$$\mathbf{u}_{r,m}^{\mathrm{out}} = \mathbf{R}_r^T \frac{\mathbf{p} - \mathbf{p}_{R,r}}{\|\mathbf{p} - \mathbf{p}_{R,r}\|}. \tag{2.51}$$

Here, $\mathbf{p}_{R,r}$ denotes the position of the rth RIS, $\mathbf{q}_{r,m}$ denotes the position of the mth scatter point, and $\mathbf{p}$ denotes the UE position. Since the RIS elements are located on the local x-z plane, only the x- and z-components of the incident and outgoing unit vectors contribute to the spatial phase. Thus, the scatter-path spatial frequencies are defined as

$$\xi_{r,m}^{\mathrm{MP}} = \left[\mathbf{u}_{r,m}^{\mathrm{in}}\right]_x + \left[\mathbf{u}_r^{\mathrm{out}}\right]_x, \tag{2.52}$$

and

$$\zeta_{r,m}^{\mathrm{MP}} = \left[\mathbf{u}_{r,m}^{\mathrm{in}}\right]_z + \left[\mathbf{u}_r^{\mathrm{out}}\right]_z. \tag{2.53}$$

2.4.4 Channel Gain

2.4.4.1 Atmospheric and Large-Scale Propagation Effects

In the considered NTN scenario, the propagation link between a satellite transmitter and a ground UE experiences several attenuation effects. According to the 3GPP NTN channel model [16], the total path loss can be expressed as

$$PL = PL_{\mathrm{b}} + PL_{\mathrm{g}} + PL_{\mathrm{s}} + PL_{\mathrm{e}}, \tag{2.54}$$

where PL denotes the total path loss in dB, PL_{b} is the basic path loss, PL_{g} represents the attenuation due to atmospheric gases, PL_{s} denotes the attenuation caused by ionospheric or tropospheric scintillation, and PL_{e} is the building entry loss. Since the transmission signal is outside the building, the PL_{e} term is ignored. What's more, for the system operates at S-band with $f_c = 2$ GHz, atmospheric attenuation PL_{g} is relatively weak compared with the free-space path loss. The basic path loss is then modeled as

$$PL_{\mathrm{b}} = FSPL(d, f_c) + PL_{\mathrm{g}} + SF, \tag{2.55}$$

The free space path loss (FSPL) is given by

$$FSPL(d, f_c) = 32.45 + 20\log_{10}(f_c) + 20\log_{10}(d), \tag{2.56}$$

The shadow fading term SF follows a zero-mean Gaussian distribution in the dB domain,

$$SF \sim \mathcal{N}(0, \sigma_{\mathrm{SF}}^2), \tag{2.57}$$

where σ_{SF} is the standard deviation of shadow fading. Therefore, the path loss is further simplified to the following equation:

$$PL = FSPL(d, f_c) + SF + PL_{\mathrm{s}}, \tag{2.58}$$

To divide constant part and distance-change part, the path loss is rewritten as

$$10^{-PL/20} = \frac{\lambda}{4\pi d}\sqrt{G_{\mathrm{space}}}. \tag{2.59}$$

where G_{space} contains the constant terms and the distance term is expressed by $\frac{\lambda}{4\pi d}$.

2.4.4.2 LoS Channel Gain

For the satellite–UE LoS path, the channel gain is modeled as

$$\rho_{\mathrm{su}} = \sqrt{G_{\mathrm{sat}} G_{\mathrm{UE}} G_{\mathrm{space}}}\frac{\lambda}{4\pi d_{\mathrm{su}}}, \tag{2.60}$$

where G_{sat} is the satellite antenna gain, G_{UE} is the UE antenna gain, d_{su} is the satellite–UE distance, $\lambda = c/f_c$ is the wavelength, and τ_{su} is the LoS propagation delay including the receiver clock bias.

2.4.4.3 RIS Channel Gain and Response

In the proposed system, each RIS is modeled as a URA composed of electrically small passive reflecting elements. Since RIS elements are commonly regarded as low-gain radiating elements placed above a conducting ground plane and a cosine-type element radiation pattern is adopted to characterize the directional response of each RIS element. Let ψ denote the angle between the propagation direction and the broadside direction of the RIS element [41]. The element radiation pattern is modeled as

$$G_{\mathrm{e}}(\psi) = \begin{cases} \gamma \cos^{2b}(\psi), & 0 \leq \psi < \frac{\pi}{2}, \\ 0, & \frac{\pi}{2} \leq \psi \leq \pi, \end{cases} \tag{2.61}$$

where γ denotes the maximum gain coefficient in the broadside direction, and b is the factor controlling the shape of the element radiation pattern. The second case in (2.61) indicates that the RIS element only responds to the incident or reflected signals within the front half-space, while the signals from the back side of the RIS are ignored. Let $\hat{\mathbf{n}}_r$ denote the broadside unit GCS vector of the rth RIS. Since the RIS elements are located on the x–z plane of the RIS and the broadside direction is aligned with the local y-axis, the global broadside direction of the rth RIS can be expressed as

$$\hat{\mathbf{n}}_r = \mathbf{R}_r \begin{bmatrix} 0 & 1 & 0 \end{bmatrix}^{\mathrm{T}}. \tag{2.62}$$

For an arbitrary unit propagation direction $\hat{\mathbf{u}}$ observed from the RIS, the angle ψ satisfies

$$\cos(\psi) = \hat{\mathbf{u}}^{\mathrm{T}} \hat{\mathbf{n}}_r. \tag{2.63}$$

Therefore, the RIS element gain in the direction $\hat{\mathbf{u}}$ can be written in vector form as

$$G_{\mathrm{e}}(\hat{\mathbf{u}}) = \gamma \left(\hat{\mathbf{u}}^{\mathrm{T}} \hat{\mathbf{n}}_r \right)^{2b}, \tag{2.64}$$

The physical aperture of each RIS element is

$$A_{\mathrm{e}} = \frac{\lambda^2}{4}. \tag{2.65}$$

According to the relationship between the effective aperture and antenna gain, the broadside gain coefficient is given by

$$\gamma = \frac{4\pi A_{\mathrm{e}}}{\lambda^2}. \tag{2.66}$$

Meanwhile, γ and q satisfy the following relationship:

$$\gamma = 2(2b+1), \qquad b = \frac{\gamma}{4} - \frac{1}{2}. \tag{2.67}$$

When $A_{\mathrm{e}} = \lambda^2/4$, the broadside gain coefficient and the directivity factor become

$$\gamma = \pi, \qquad b = \frac{\pi}{4} - \frac{1}{2} \approx 0.285. \tag{2.68}$$

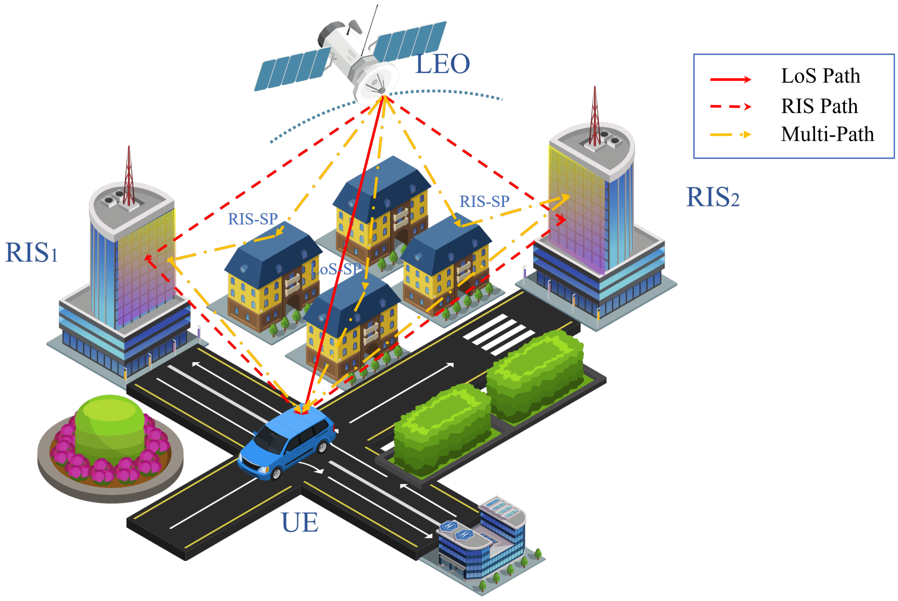

Figure 2.7: The system illustration with LoS and RIS scatter-path.

Meanwhile, γ and q satisfy the following relationship:

$$\gamma = 2(2b+1), \qquad b = \frac{\gamma}{4} - \frac{1}{2}. \tag{2.69}$$

This value corresponds to a broad low-gain RIS element radiation pattern and is suitable for modeling general passive RIS reflecting elements. For each RIS path, two RIS directional gains need to be considered based, where $G_{\mathrm{sr,r}}$ and $G_{\mathrm{ru,r}}$ represent the incident-side directional gain and outgoing-side directional gain. $\mathbf{u}_{sr,r}$ and $\mathbf{u}_{ru,r}$ denote the incident and outgoing unit direction vector from the r th RIS.

$$G_{\mathrm{sr,r}} = G_{\mathrm{e}}\left(\mathbf{u}_{sr,r}\right), \tag{2.70}$$

and

$$G_{\mathrm{ru,r}} = G_{\mathrm{e}}\left(\mathbf{u}_{ru,r}\right). \tag{2.71}$$

For the rth RIS-assisted path, the cascaded channel coefficient is separated into $\rho_{\mathrm{sr},r}$ and $\rho_{\mathrm{ru},r}$.

$$\rho_{\mathrm{sru},r} = \rho_{\mathrm{sr},r}\rho_{\mathrm{ru},r}. \tag{2.72}$$

The satellite–RIS channel gain is modeled as

$$\rho_{\mathrm{sr},r} = \sqrt{G_{\mathrm{sat}} G_{\mathrm{sr},r} G_{\mathrm{space}}} \frac{\lambda}{4\pi d_{\mathrm{sr},r}}, \tag{2.73}$$

The RIS–UE channel gain is written as

$$\rho_{\mathrm{ru},r} = \sqrt{G_{\mathrm{ru},r} G_{\mathrm{UE}}} \frac{\lambda}{4\pi d_{\mathrm{ru},r}}, \tag{2.74}$$

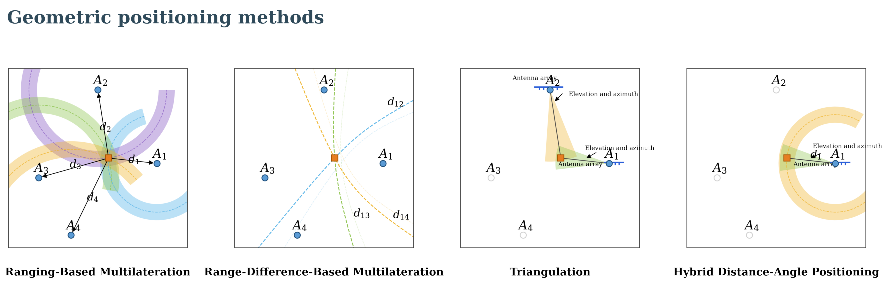

Figure 2.8: Four Position Method [15].

2.4.4.4 MP Channel Gain

The MP scatter paths are included two types: the scatter paths in the LoS path and scatter paths in RIS paths in Fig. 2.7. The LoS scatter paths do not involve any RIS array response, whereas the RIS scatter paths include both a scatter-path gain and the RIS array response. Its complex channel gain is modeled as [39]

$$\rho_{su,m} = \sqrt{G_{\text{sat}} G_{\text{UE}} G_{\text{space}}} \frac{\sqrt{4\pi c_{RCS}}\lambda}{(4\pi)^2 d_{T,m} d_{R,m}}, \tag{2.75}$$

where c_{RCS} is as the radar cross section (RCS) coefficient of the m-th SP in the LoS scatter path. Similarly, the scatter paths in RIS paths can be defined by:

$$G_{\text{sr,r,m}} = G_{\text{e}} \left(\mathbf{u}_{r,m}^{in} \right), \tag{2.76}$$

$$G_{\text{ru,r,m}} = G_{\text{e}} \left(\mathbf{u}_{r,m}^{out} \right), \tag{2.77}$$

$$\rho_{sru,r,m} = \sqrt{G_{\text{sat}} G_{\text{UE}} G_{\text{space}} G_{sr,r,m} G_{ru,r,m}} \frac{\sqrt{4\pi c_{RCS}}\lambda^2}{(4\pi)^3 d_{T,r,m} d_{R,r,m} d_{ru,r}} \tag{2.78}$$

2.5 Geometric Positioning Methods

Geometric positioning methods estimate the target position by using range, range-difference, or angle measurements from known reference nodes [15, 26, 42]. Let the UE position be

$$\mathbf{p} = [x, y, z]^T, \tag{2.79}$$

and let the position of the r-th RIS be

$$\mathbf{p}_{R,r} = [x_r, y_r, z_r]^T, \quad r = 1, \dots, R, \tag{2.80}$$

According to these measurements, geometric positioning methods can be classified into ranging-based multilateration, range-difference-based multilateration, triangulation, and hybrid distance-angle positioning, as shown in Fig. 2.8.

2.5.1 Ranging-Based Multilateration

Ranging-based multilateration estimates the UE position from absolute range measurements between the target and multiple anchors. The range measurement from the r-th RIS is modeled as

$$\hat{d}_r = \|\mathbf{p} - \mathbf{p}_{R,r}\| + n_r, \tag{2.81}$$

where $\hat{d}_r$ is the measured range and n_r denotes the ranging error. Geometrically, each range measurement defines a sphere centered at the corresponding RIS positions:

$$(x - x_r)^2 + (y - y_r)^2 + (z - z_r)^2 = \hat{d}_r^2. \tag{2.82}$$

The UE position is obtained from the intersection of multiple spheres. In practice, due to measurement errors, the position is commonly estimated by nonlinear least squares:

$$\hat{\mathbf{p}} = \arg\min_{\mathbf{p}} \sum_{r=1}^{R} w_r \left(\hat{d}_r - \|\mathbf{p} - \mathbf{p}_{R,r}\|\right)^2, \tag{2.83}$$

where w_r is a weighting coefficient. This method is suitable when range-related measurements, such as TOA or round trip time (RTT), are available. However, the range-position relationship is nonlinear, and linearized solutions may introduce linearization errors.

2.5.2 Range-Difference-Based Multilateration

Range-difference-based multilateration estimates the UE position from the difference between ranges measured with respect to different RIS. This method is often associated with time difference of arrival (TDOA) measurements and requires tight synchronization among RISs. Taking the first RIS as the reference, the range-difference measurement can be expressed as

$$\Delta\hat{d}_{r1} = \|\mathbf{p} - \mathbf{p}_{R,r}\| - \|\mathbf{p} - \mathbf{p}_{R,1}\| + n_{r1}, \quad r = 2, \ldots, R. \tag{2.84}$$

For TDOA measurements,

$$\Delta\hat{d}_{r1} = c\Delta\hat{\tau}_{r1}, \tag{2.85}$$

where c is the speed of light and $\Delta\hat{\tau}_{r1}$ is the measured time difference. Each range-difference measurement defines a hyperboloid:

$$\|\mathbf{p} - \mathbf{p}_{R,r}\| - \|\mathbf{p} - \mathbf{p}_1\| = \Delta\hat{d}_{r1}. \tag{2.86}$$

The UE position can be estimated by

$$\hat{\mathbf{p}} = \arg\min_{\mathbf{p}} \sum_{r=2}^{R} w_{r1} \left(\Delta\hat{d}_{r1} - \|\mathbf{p} - \mathbf{p}_r\| + \|\mathbf{p} - \mathbf{p}_1\|\right)^2. \tag{2.87}$$

where w_{r1} is a weighting coefficient. This method is widely used in cellular positioning because base stations can usually be synchronized. Similar to ranging-based multilateration, its measurement model is nonlinear and may suffer from linearization errors. In this work, the Range-difference-based multilateration provides fundament for the delay-difference positioning method using the delay information from LoS path and RIS paths.

2.5.3 Triangulation

Triangulation estimates the UE position from angle measurements obtained at multiple RISs. For the r-th RIS, let $\hat{\theta}^{az}_{ru,r}$ and $\hat{\theta}^{el}_{ru,r}$ denote the estimated azimuth and elevation angles. The corresponding unit direction vector is

$$\hat{\mathbf{u}}_r = \begin{bmatrix} \cos\hat{\theta}^{az}_{ru,r}\cos\hat{\theta}^{el}_{ru,r} \\ \sin\hat{\theta}^{az}_{ru,r}\cos\hat{\theta}^{el}_{ru,r} \\ \sin\hat{\theta}^{el}_{ru,r} \end{bmatrix}. \tag{2.88}$$

Ideally, the UE lies on the bearing line

$$\mathbf{p} = \mathbf{p}_{R,r} + d_r\hat{\mathbf{u}}_r, \tag{2.89}$$

where d_r is an unknown distance parameter. With multiple RISs, the UE position can be estimated by minimizing the perpendicular distance to all bearing lines. Define the perpendicular projection $\mathbf{P}_r$

$$\mathbf{P}_r = \mathbf{I} - \hat{\mathbf{u}}_r\hat{\mathbf{u}}_r^T. \tag{2.90}$$

Then, the UE estimation is resolved by the perpendicular distance

$$\hat{\mathbf{p}} = \arg\min_{\mathbf{p}} \sum_{r=1}^{R} w_r \left\|\mathbf{P}_r(\mathbf{p} - \mathbf{p}_{R,r})\right\|^2. \tag{2.91}$$

where w_r is the weight coefficient of rth measurement path. A closed-form weighted least-squares solution is

$$\hat{\mathbf{p}} = \left(\sum_{r=1}^{R} w_r\mathbf{P}_r\right)^{-1}\left(\sum_{r=1}^{R} w_r\mathbf{P}_r\mathbf{p}_{R,r}\right). \tag{2.92}$$

Triangulation is suitable when AoA or AoD measurements are available. In this thesis, the triangulation method provides fundament the bearing-line positioning method because the RIS AoD is extracted from the channel estimation algorithm. On the other hand, this positioning method is sensitive to angle errors, which requires high-accuracy angle estimation algorithm.

2.5.4 Hybrid Distance-Angle Positioning

Hybrid distance-angle positioning combines range and angle measurements, which can estimate three-dimensional position even from a single RIS if both range and two-dimensional angle information are available. RIS at $\mathbf{p}_{R,r}$ receives the measurement values including the range $\hat{d}_{R,r}$, azimuth $\hat{\theta}^{az}_{ru,r}$, and elevation $\hat{\theta}^{el}_{ru,r}$. The unit direction vector can be expressed by $\hat{\mathbf{u}}_r(\hat{\theta}^{az}_{ru,r}, \hat{\theta}^{el}_{ru,r})$ For each RIS $\mathbf{p}_{R,r}$, the UE position can be reconstructed as

$$\hat{\mathbf{p}} = \mathbf{p}_{R,r} + \hat{d}_r\hat{\mathbf{u}}_r. \tag{2.93}$$

Furthermore, when multiple RISs are available, range and angle constraints can be jointly fused as

$$\hat{\mathbf{p}} = \arg\min_{\mathbf{p}} \sum_{r=1}^{R} w_{d,r}\left(\hat{d}_r - \|\mathbf{p} - \mathbf{p}_{R,r}\|\right)^2 + \sum_{r=1}^{R} w_{\theta,r}\left\|\mathbf{P}_r(\mathbf{p} - \mathbf{p}_{R,r})\right\|^2. \tag{2.94}$$

where $w_{d,r}$ is a weighting coefficient for the distance and $w_{\theta,r}$ is is a weighting coefficient for the angle. Hybrid positioning exploits both range constraints and directional bearing-line constraints to reduce geometric ambiguity and improve robustness, which inspires this thesis to build a joint positioning method in this thesis. However, since the range term $\|\mathbf{p} - \mathbf{p}_{R,r}\|$ is nonlinear in $\mathbf{p}$, how to obtain optimal resolution through the cost function is the key part to improve the localization accuracy.

3

System Signal Model

This section establishes the system signal model for the subsequent positioning signal channel model. First, the main assumptions are introduced to clarify the signal propagation environment and simplify some variation. Second, the transmitted OFDM signal is defined in the time domain with signal parameters. Third, the received passband signal is derived by incorporating the previously-defined effects of propagation delay, Doppler shift, channel gain, and RIS profile. Fourth, the baseband signal is further sampled to reveal the information over subcarriers and OFDM symbols. Fifth, to provide a simplified mathematical formulation, the observed signals are represented by compact matrices for the following algorithms description. Sixth, the assumptions in this work are summarized to further describe the model with more details.

3.1 Transmit Signal Model

The satellite employs an OFDM waveform with K subcarriers and L OFDM symbols, as shown in Fig. 3.1. Each OFDM symbol has a total duration T_{sym} in equation 3.1, where T denotes the useful symbol duration, Δf is the subcarrier spacing, and T_{CP} is the cyclic prefix (CP) duration.

$$T_{\mathrm{sym}} = T + T_{\mathrm{CP}}, \quad T = 1/\Delta f \tag{3.1}$$

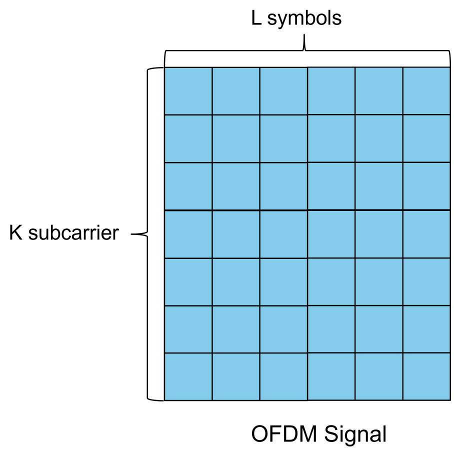

Figure 3.1: The structure illustration of the OFDM signal.

The transmitted complex baseband signal in the time-domain is given by

$$s(t) = \sqrt{\frac{P_{\mathrm{tot}}}{K}} \sum_{l=0}^{L-1} \sum_{k=0}^{K-1} x_{k,l}\, e^{j2\pi k\Delta f(t-lT_{\mathrm{sym}})} \cdot \mathrm{rect}\left(\frac{t-lT_{\mathrm{sym}}}{T_{\mathrm{sym}}}\right). \tag{3.2}$$

where P_{tot} denotes the total transmit power across all K subcarriers, $x_{k,l} \in \mathbb{C}$ is the pilot symbol transmitted on the k-th subcarrier of the l-th OFDM symbol with$|x_{k,l}| = 1$, and $\mathrm{rect}(t) = 1$ for $t \in [0,1]$ and otherwise 0, in this work $t \in [0, LT_{\mathrm{sym}}]$. The normalization factor $\sqrt{\frac{P_{\mathrm{tot}}}{K}}$ ensures that the average power per subcarrier equals P_{tot}/K, so that the total transmit power across all subcarriers satisfies $\mathbb{E}[\|s(t)\|^2] = P_{\mathrm{tot}}$ when $|x_{k,l}|^2 = 1$. The transmitted passband signal is

$$\tilde{s}(t) = \Re\left\{e^{j2\pi f_c t}\, s(t)\right\}, \tag{3.3}$$

In this work, all time-frequency resource elements are dedicated to localization pilot symbols. Specifically, the pilot sequence is known at the receiver and can be written as

$$x_{k,l} = x_0, \qquad |x_0| = 1, \qquad k = 0, \ldots, K-1, \quad l = 0, \ldots, L-1. \tag{3.4}$$

Since the transmitted pilots are known, the received signal is fully parameterized by the unknown channel parameters for the further performance evaluation.

3.2 Received Passband Signal Model

The received passband signal without MP at the UE consists of the LoS component, the RIS components and thermal noise.

$$\tilde{y}(t) = \tilde{y}_{\mathrm{su}}^{\mathrm{LoS}}(t) + \sum_{r=1}^{R} \tilde{y}_{\mathrm{sru},r}^{\mathrm{RIS}}(t) + \tilde{n}(t), \tag{3.5}$$

The received passband signal with MP at the UE consists of the LoS component, the LoS MP components, the RIS components, the RIS MP components, and thermal noise.

$$\tilde{y}(t) = \tilde{y}_{\mathrm{su}}^{\mathrm{LoS}}(t) + \tilde{y}_{\mathrm{su}}^{\mathrm{MP}}(t) + \sum_{r=1}^{R} \left(\tilde{y}_{\mathrm{sru},r}^{\mathrm{RIS}}(t) + \tilde{y}_{\mathrm{sru},r}^{\mathrm{MP}}(t)\right) + \tilde{n}(t), \tag{3.6}$$

where $\tilde{n}(t)$ denotes the additive thermal noise at the receiver with power spectral density (PSD) N_0. The LoS satellite–UE component is modeled as

$$\tilde{y}_{\mathrm{su}}^{\mathrm{LoS}}(t) = \rho_{\mathrm{su}}\, s(t - \tau_{\mathrm{su}} + \nu_{\mathrm{su}} t), \tag{3.7}$$

where ρ_{su}, τ_{su}, and ν_{su} denote the LoS path channel amplitude, propagation delay, and Doppler-induced frequency-shift factor.
The LoS MP component is given by

$$\tilde{y}_{\mathrm{su}}^{\mathrm{MP}}(t) = \sum_{m=1}^{M_0} \rho_{\mathrm{su},m}\, s(t - \tau_{\mathrm{su},m} + \nu_{\mathrm{su},m} t), \tag{3.8}$$

where M_0 is the number of MP scatter paths, and $\rho_{\text{su},m}$, $\tau_{\text{su},m}$, and $\nu_{\text{su},m}$ are the mth LoS MP path, amplitude, delay, and Doppler shift respectively. The rth RIS signal path is expressed as

$$\tilde{y}^{\text{RIS}}_{\text{sru},r}(t) = \rho_{\text{sru},r} \sum_{n=0}^{N_r-1} s\Big(t - \tau_{\text{sru},r} + \nu_{\text{sru},r}t - \tau_{r,n}(t) - \tau_{\theta_{\text{rs}},r,n} - \tau_{\theta_{\text{ru}},r,n}\Big), \tag{3.9}$$

where the parameters $\rho_{\text{sru},r}$, $\tau_{\text{sru},r}$, and $\nu_{\text{sru},r}$ denote the rth RIS path amplitude, initial delay, and Doppler-induced frequency-shift factor respectively. And the term $\tau_{r,n}(t)$ is the controllable delay introduced by the nth reflecting element of the rth RIS at time t. The element-dependent delays $\tau_{\theta_{\text{rs}},r,n}$ and $\tau_{\theta_{\text{ru}},r,n}$ describe the relative propagation delays with respect to the RIS phase center. The geometric delay difference of the nth RIS element can be expressed as

$$\tau_{\boldsymbol{\theta},r,n} = -\frac{\mathbf{p}^T_{r,n}\mathbf{u}(\boldsymbol{\theta})}{c}. \tag{3.10}$$

where $\mathbf{p}_{r,n}$ denotes the nth element position in the $r$the RIS and a positive $\tau_{\boldsymbol{\theta},n,r}$ value corresponds to a delay with respect to the reference point while a negative value denotes a earlier arrival. The RIS MP component associated with the rth RIS is modeled as

$$\begin{aligned}\tilde{y}^{\text{MP}}_{\text{sru},r}(t) = \sum_{m=1}^{M_r} \sum_{n=0}^{N_r-1} \rho_{\text{sru},r,m}\, s\Big(& t - \tau_{\text{sru},r,m} - \tau_{n,r}(t) + \nu_{\text{sru},r,m}t \\ & - \tau_{\xi^{MP}_{r,m},r,n,m} - \tau_{\zeta^{MP}_{r,m},r,n,m}\Big),\end{aligned} \tag{3.11}$$

where M_r denotes the number of MP components associated with the rth RIS branch. The parameters $\rho_{\text{sru},r,m}$, $\tau_{\text{sru},r,m}$, and $\nu_{\text{sru},r,m}$ represent the amplitude, delay, and Doppler shift of the mth RIS MP component, respectively. The terms $\tau_{\xi^{MP}_{r,m},r,n,m}$ and $\tau_{\zeta^{MP}_{r,m},r,n,m}$ denote the MP geometric delay of nth elements in rth RIS.

3.3 Received Baseband Signal Model

After downconversion of the received passband signal in (3.6), the noise-free complex baseband signal can be decomposed into the LoS component, the LoS MP components, the RIS components, and the RIS MP components as

$$y(t) = y^{\text{LoS}}_{\text{su}}(t) + y^{\text{MP}}_{\text{su}}(t) + \sum_{r=1}^{R} \left(y^{\text{RIS}}_{\text{sru},r}(t) + y^{\text{MP}}_{\text{sru},r}(t)\right), \tag{3.12}$$

The baseband LoS component is given by

$$y^{\text{LoS}}_{\text{su}}(t) = \alpha_{\text{su}} e^{j2\pi f_c \nu_{\text{su}} t} s(t - \tau_{\text{su}} + \nu_{\text{su}}t)\,, \tag{3.13}$$

$$\alpha_{\text{su}} = \rho_{\text{su}} e^{-j2\pi f_c \tau_{\text{su}}} \tag{3.14}$$

α_{su} is the complex baseband LoS channel gain. Although the carrier term is removed by downconversion, the carrier-frequency Doppler phase $e^{j2\pi f_c \nu_{\mathrm{su}} t}$ remains in the baseband signal. The LoS MP component is modeled as

$$y_{\mathrm{su}}^{\mathrm{MP}}(t) = \sum_{m=1}^{M_0} \alpha_{\mathrm{su},m} e^{j2\pi f_c \nu_{\mathrm{su},m} t} s(t - \tau_{\mathrm{su},m} + \nu_{\mathrm{su},m} t)\,, \tag{3.15}$$

$$\alpha_{\mathrm{su},m} = \rho_{\mathrm{su},m} e^{-j2\pi f_c \tau_{\mathrm{su},m}} \tag{3.16}$$

For the rth RIS, the RIS component is written as

$$y_{\mathrm{sru},r}^{\mathrm{RIS}}(t) = \alpha_{\mathrm{sru},r} e^{j2\pi f_c \nu_{\mathrm{sru},r} t} s(t - \tau_{\mathrm{sru},r} + \nu_{\mathrm{sru},r} t)\, G_{\mathrm{RIS},r}(t), \tag{3.17}$$

$$\alpha_{\mathrm{sru},r} = \rho_{\mathrm{sru},r} e^{-j2\pi f_c \tau_{\mathrm{sru},r}} \tag{3.18}$$

$\alpha_{\mathrm{sru},r}$ is the cascaded baseband channel coefficient of the rth RIS path. The term $G_{\mathrm{RIS},r}(t)$ denotes the effective RIS response. Let $\mathbf{a}_r(\boldsymbol{\theta}) \in \mathbb{C}^{N_r}$ denote the rth RIS steering vector associated with the angle tuple $\boldsymbol{\theta}$. The nth element of $\mathbf{a}_r(\boldsymbol{\theta})$ is modeled as

$$[\mathbf{a}_r(\boldsymbol{\theta})]_n = a_{r,n}(\boldsymbol{\theta}) = \exp\left(-j2\pi f_c \tau_{\boldsymbol{\theta},r,n}\right), \tag{3.19}$$

By stacking the responses of all RIS elements in rth RIS, the RIS steering vector can be written as

$$\mathbf{a}_r(\boldsymbol{\theta}) = \begin{bmatrix} e^{-j2\pi f_c \tau_{\boldsymbol{\theta},r,1}} \\ e^{-j2\pi f_c \tau_{\boldsymbol{\theta},r,2}} \\ \vdots \\ e^{-j2\pi f_c \tau_{\boldsymbol{\theta},r,N_r}} \end{bmatrix} \in \mathbb{C}^{N_r}. \tag{3.20}$$

The position of rth RIS $\mathbf{P}_{R,r}$ is expressed as

$$\mathbf{P}_{R,r} = [\mathbf{p}_{r,1}, \mathbf{p}_{r,2}, \ldots, \mathbf{p}_{r,N_r}] \in \mathbb{R}^{3\times N_r}, \tag{3.21}$$

the steering vector can be compactly expressed as

$$\mathbf{a}_r(\boldsymbol{\theta}) = \exp\left(j\frac{2\pi f_c}{c} \mathbf{P}_{R,r}^T \mathbf{u}(\boldsymbol{\theta}) \right). \tag{3.22}$$

For a satellite-to-RIS AoA $\boldsymbol{\theta}_{\mathrm{rs},r}$ and RIS-to-UE AoD $\boldsymbol{\theta}_{\mathrm{ru},r}$, the RIS response is expressed as

$$G_{\mathrm{RIS},r}(t) = \left(\mathbf{a}_r(\boldsymbol{\theta}_{\mathrm{rs},r}) \odot \mathbf{a}_r(\boldsymbol{\theta}_{\mathrm{ru},r})\right)^T \boldsymbol{\omega}_r(t), \tag{3.23}$$

where $\odot$ denotes the Hadamard product. The RIS MP component in the rth RIS is given by

$$y_{\mathrm{sru},r}^{\mathrm{MP}}(t) = \sum_{m=1}^{M_r} \alpha_{\mathrm{sru},r,m} e^{j2\pi f_c \nu_{\mathrm{sru},r,m} t} s(t - \tau_{\mathrm{sru},r,m} + \nu_{\mathrm{sru},r,m} t)\, G_{\mathrm{RIS},r,m}^{\mathrm{MP}}(t), \tag{3.24}$$

$$\alpha_{\mathrm{sru},r,m} = \rho_{\mathrm{sru},r,m} e^{-j2\pi f_c \tau_{\mathrm{sru},r,m}} \tag{3.25}$$

$G_{\mathrm{RIS},r,m}^{\mathrm{MP}}(t)$ is the RIS spatial response to the mth MP associated with the rth RIS.

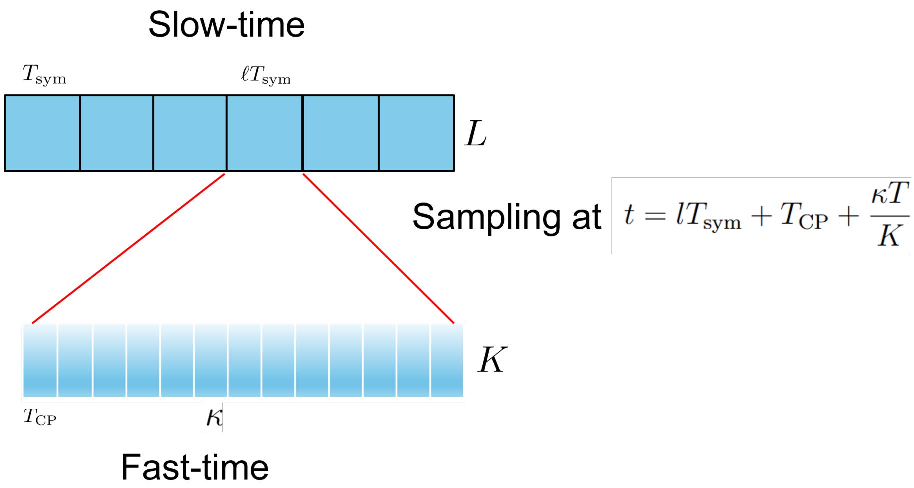

Figure 3.2: The OFDM sampling process.

The RIS steering vector in MP is then written as

$$\mathbf{a}_{mp,r}\left(\xi_{r,m}^{MP}, \zeta_{r,m}^{MP}\right) = \exp\left(\jmath\frac{2\pi f_c}{c}\mathbf{P}_{R,r}^{T}\begin{bmatrix}\xi_{r,m}^{MP}\\ 0\\ \zeta_{r,m}^{MP}\end{bmatrix}\right), \tag{3.26}$$

Therefore, the RIS array response of the mth scatter path associated with the rth RIS is expressed as

$$G_{RIS,r,m}^{\mathrm{MP}}(t) = \mathbf{a}_{\mathbf{mp,r}}^{\mathbf{T}}(\mathbf{t})\boldsymbol{\omega}_r(t) \tag{3.27}$$

3.4 Sampled Received Signal Model

After down-conversion, the received signal is sampled at the following time instances in Fig. 3.2

$$t = lT_{\mathrm{sym}} + T_{\mathrm{CP}} + \frac{\kappa T}{K}, \qquad \kappa = 0, \dots, K-1, \quad l = 0, \dots, L-1, \tag{3.28}$$

After CP removal, these LoS and RIS signals are modeled as follows:

$$\begin{aligned} Y_{\mathrm{su},\kappa,l}^{\mathrm{LoS}} =& \alpha_{\mathrm{su}} e^{\jmath 2\pi f_c \nu_{\mathrm{su}}\left(lT_{\mathrm{sym}}+T_{\mathrm{CP}}+\frac{\kappa T}{K}\right)} \\ & \times s\Big((1+\nu_{\mathrm{su}})\left(lT_{\mathrm{sym}} + T_{\mathrm{CP}} + \frac{\kappa T}{K}\right) - \tau_{\mathrm{su}}\Big), \end{aligned} \tag{3.29}$$

$$\begin{aligned} Y_{\mathrm{su,m},\kappa,l}^{\mathrm{MP}} =& \alpha_{\mathrm{su,m}} e^{\jmath 2\pi f_c \nu_{\mathrm{su,m}}\left(lT_{\mathrm{sym}}+T_{\mathrm{CP}}+\frac{\kappa T}{K}\right)} \\ & \times s\Big((1+\nu_{\mathrm{su,m}})\left(lT_{\mathrm{sym}} + T_{\mathrm{CP}} + \frac{\kappa T}{K}\right) - \tau_{\mathrm{su,m}}\Big), \end{aligned} \tag{3.30}$$

$$\begin{aligned} Y_{\mathrm{sru},r,\kappa,l}^{\mathrm{RIS}} =& \alpha_{\mathrm{sru},r} G_{\mathrm{RIS},r,l} e^{\jmath 2\pi f_c \nu_{\mathrm{sru},r}\left(lT_{\mathrm{sym}}+T_{\mathrm{CP}}+\frac{\kappa T}{K}\right)} \\ & \times s\Big((1+\nu_{\mathrm{sru},r})\left(lT_{\mathrm{sym}} + T_{\mathrm{CP}} + \frac{\kappa T}{K}\right) - \tau_{\mathrm{sru},r}\Big), \end{aligned} \tag{3.31}$$

$$
\begin{aligned}
Y^{\mathrm{MP}}_{\mathrm{sru},r,m,\kappa,l} =& \alpha_{\mathrm{sru},r,m} G^{MP}_{\mathrm{RIS},r,m,l} e^{\jmath 2\pi f_c \nu_{\mathrm{sru},r,m}\left(lT_{\mathrm{sym}}+T_{\mathrm{CP}}+\frac{\kappa T}{K}\right)} \\
& \times s\Big((1+\nu_{\mathrm{sru},r,m})\left(lT_{\mathrm{sym}}+T_{\mathrm{CP}}+\frac{\kappa T}{K}\right)-\tau_{\mathrm{sru},r,m}\Big),
\end{aligned}
\tag{3.32}
$$

where $G_{\mathrm{RIS},r,l}$ and $G^{MP}_{\mathrm{RIS},r,m,l}$ are the sampled RIS and MP RIS response during the lth OFDM symbol. To further simplify the channel models, there are several assumptions to conduct.

- The constant phase rotation caused by $2\pi f_c \nu_i T_{\mathrm{CP}}$ can be absorbed into α_i, where $i \in (su; su, m; sru, r; sru, r, m)$.
- The known CP-related subcarrier phase caused by $k\Delta f T_{\mathrm{CP}}$ inside $s(\cdot)$ can be merged into the pilot symbol $x_{k,\ell}$.
- The terms $\nu_i T_{\mathrm{CP}}$ and $\nu_i \kappa T/K$ ins $s(\cdot)$ are neglected because they only introduce very small time-delay perturbations.

  For the system parameters in Table 5.1, we have $K = 2000$, $\Delta f = 15$ kHz, $T = 1/\Delta f = 66.67$ μs, $T_{\mathrm{CP}} = 0.07T = 4.67$ μs, and $\mathrm{B} = K\Delta f = 30$ MHz. The delay resolution is therefore

$$
\frac{1}{\mathrm{B}} = \frac{1}{K\Delta f} \approx 33.3 \text{ ns}. \tag{3.33}
$$

  In Table 5.1, $\theta_{\mathrm{el}} = 45^\circ$, $\theta_{\mathrm{az}} = 90^\circ$, and $h = 600$ km, based on equation 2.2 the satellite distance is calculated as $d_{\mathrm{sat}} \approx 814.80km$, based on equation 2.3 the satellite velocity $\|\mathbf{v}_{\mathrm{sat}}\| \approx 8.111 \times 10^3$ m/s generated by the orbit function is

$$
\mathbf{v}_{\mathrm{sat}} \approx [0,\ -8.0834 \times 10^3,\ 6.7038 \times 10^2]^T \text{ m/s} \tag{3.34}
$$

  Furthermore, based on equations 2.40-2.43 and realistic simulation parameters, $\nu_{su} \approx 1.84845 \times 10^{-5}$ and $\nu_{sru,r} \approx 1.84849 \times 10^{-5}$. There are several assumptions to list:

$$
\nu_{\mathrm{su}} \approx \nu_{\mathrm{sru},1} \approx \nu_{\mathrm{sru},2}. \tag{3.35}
$$

$$
|\nu_i| \leq 1.85 \times 10^{-5} \approx 2 \times 10^{-5}. \tag{3.36}
$$

  With the Doppler factor bounded by $|\nu_i| \lesssim 2 \times 10^{-5}$, the two neglected delay perturbations are upper bounded by

$$
|\nu_i T_{\mathrm{CP}}| \leq 2 \times 10^{-5} \times 4.67\ \mu\text{s} \approx 9.3 \times 10^{-11} \text{ s} = 0.093 \text{ ns}, \tag{3.37}
$$

$$
\left|\nu_i \frac{\kappa T}{K}\right| \leq |\nu_i| T = 2 \times 10^{-5} \times 66.67\ \mu\text{s} \approx 1.33 \text{ ns}. \tag{3.38}
$$

  Both values are much smaller than the delay resolution 33.3 ns, whose distortion is negligible for $s(\cdot)$.
- In contrast, the inter-subcarrier Doppler term $\nu_i l T_{\mathrm{sym}}$ is retained because it accumulates over the whole observation window. For $L = 256$ and $T_{\mathrm{sym}} = 1.07T = 71.33$ μs, its maximum magnitude is

$$
|\nu_i (L-1) T_{\mathrm{sym}}| \lesssim 2 \times 10^{-5} \times 255 \times 71.33\ \mu\text{s} \approx 363.7 \text{ ns}, \tag{3.39}
$$

  which is larger than the delay resolution and therefore cannot be ignored.

The maximum phase rotations of the slow-time Doppler phase and the fast-time Doppler are approximately

$$2\pi|f_c\nu_i(L-1)T_{\mathrm{sym}}| \approx 1.46 \times 10^3\pi \text{ rad}, \tag{3.40}$$

and

$$2\pi\left|f_c\nu_i\frac{(K-1)T}{K}\right| \approx 5.3\pi \text{ rad}, \tag{3.41}$$

These phase rotations are non-negligible and must be retained in the sampled received signal model.

Based on these assumptions, the sampled LoS and RIS signals can be simplified as

$$\begin{aligned} Y^{\mathrm{LoS}}_{\mathrm{su},\kappa,l} =& \alpha_{\mathrm{su}} e^{\jmath 2\pi f_c \nu_{\mathrm{su}}\left(lT_{\mathrm{sym}}+\frac{\kappa T}{K}\right)} \\ &\times s\left(lT_{\mathrm{sym}}+\frac{\kappa T}{K}-\tau_{\mathrm{su}}+\nu_{\mathrm{su}}lT_{\mathrm{sym}}\right), \end{aligned} \tag{3.42}$$

$$\begin{aligned} Y^{\mathrm{MP}}_{\mathrm{su,m},\kappa,l} =& \alpha_{\mathrm{su,m}} e^{\jmath 2\pi f_c \nu_{\mathrm{su,m}}\left(lT_{\mathrm{sym}}+\frac{\kappa T}{K}\right)} \\ &\times s\left(lT_{\mathrm{sym}}+\frac{\kappa T}{K}-\tau_{\mathrm{su,m}}+\nu_{\mathrm{su,m}}lT_{\mathrm{sym}}\right), \end{aligned} \tag{3.43}$$

$$\begin{aligned} Y^{\mathrm{RIS}}_{\mathrm{sru},r,\kappa,l} =& \alpha_{\mathrm{sru},r} G_{\mathrm{RIS},r,l} e^{\jmath 2\pi f_c \nu_{\mathrm{sru},r}\left(lT_{\mathrm{sym}}+\frac{\kappa T}{K}\right)} \\ &\times s\left(lT_{\mathrm{sym}}+\frac{\kappa T}{K}-\tau_{\mathrm{sru},r}+\nu_{\mathrm{sru},r}lT_{\mathrm{sym}}\right), \end{aligned} \tag{3.44}$$

$$\begin{aligned} Y^{\mathrm{MP}}_{\mathrm{sru},r,m,\kappa,l} =& \alpha_{\mathrm{sru},r,m} G^{MP}_{\mathrm{RIS},r,m,l} e^{\jmath 2\pi f_c \nu_{\mathrm{sru},r,m}\left(lT_{\mathrm{sym}}+\frac{\kappa T}{K}\right)} \\ &\times s\left(lT_{\mathrm{sym}}+\frac{\kappa T}{K}-\tau_{\mathrm{sru},r,m}+\nu_{\mathrm{sru},r,m}lT_{\mathrm{sym}}\right). \end{aligned} \tag{3.45}$$

3.5 Observations in Compact Matrix Form

By inserting the OFDM transmit signal in (3.2) into (3.42)–(3.45), the received observations can be written in compact matrix form. Let $\mathbf{Y} \in \mathbb{C}^{K\times L}$ denote the received sample matrix after CP removal, where rows correspond to fast-time samples and columns correspond to OFDM symbols. Let $\mathbf{F} \in \mathbb{C}^{K\times K}$ denote the unitary fast Fourier transform (FFT) matrix, and define the pilot matrix

$$[\mathbf{X}]_{k,l} = \sqrt{\frac{P_{\mathrm{tot}}}{K}}\, x_{k,l}. \tag{3.46}$$

For any propagation path $i = su; sru, r; su, m; sru, r, m$, define the fast-time Doppler matrix, the delay and inter-subcarrier Doppler matrix and the slow-time Doppler matrix

$$[\mathbf{A}_i]_{\kappa,l} = e^{\jmath 2\pi f_c \nu_i \frac{\kappa T}{K}}, \tag{3.47}$$

$$[\mathbf{B}_i]_{k,l} = e^{-\jmath 2\pi k\Delta f(\tau_i-\nu_i lT_{\mathrm{sym}})}, \tag{3.48}$$

$$[\mathbf{C}_i]_{k,l} = e^{\jmath 2\pi f_c \nu_i l T_{\text{sym}}}. \tag{3.49}$$

$\mathbf{A}_i$ captures the fast-time Doppler effect, $\mathbf{B}_i$ captures both the delay-induced subcarrier phase and the inter-subcarrier Doppler effect, and $\mathbf{C}_i$ captures the slow-time Doppler phase across OFDM symbols. The LoS observation matrix can thus be constructed as follows:

$$\mathbf{Y}_{\text{su}}^{\text{LoS}} = \alpha_{\text{su}} \mathbf{A}_{\text{su}} \odot \mathbf{F}^H \left(\mathbf{B}_{\text{su}} \odot \mathbf{C}_{\text{su}} \odot \mathbf{X} \right). \tag{3.50}$$

The rth RIS path is defined

$$\mathbf{Y}_{\text{sru},r}^{\text{RIS}} = \alpha_{\text{sru},r} \mathbf{A}_{\text{sru},r} \odot \mathbf{F}^H \left(\mathbf{B}_{\text{sru},r} \odot \mathbf{C}_{\text{sru},r} \odot \mathbf{G}_{\text{RIS},r} \odot \mathbf{X} \right). \tag{3.51}$$

where $\mathbf{G}_{\text{RIS},r} \in \mathbb{C}^{K \times L}$ is the RIS response matrix. Similarly, the LoS MP matrix is expressed as

$$\mathbf{Y}_{\text{su}}^{\text{MP}} = \sum_{m=1}^{M_0} \alpha_{\text{su},m} \mathbf{A}_{\text{su},m}^{\text{MP}} \odot \mathbf{F}^H \left(\mathbf{B}_{\text{su},m}^{\text{MP}} \odot \mathbf{C}_{\text{su},m}^{\text{MP}} \odot \mathbf{X} \right), \tag{3.52}$$

where the matrices $\mathbf{A}_{\text{su},m}^{\text{MP}}$, $\mathbf{B}_{\text{su},m}^{\text{MP}}$, and $\mathbf{C}_{\text{su},m}^{\text{MP}}$ are obtained from (3.47)–(3.49)
For the RIS MP components associated with the rth RIS, the equation is represented by:

$$\mathbf{Y}_{\text{sru},r}^{\text{MP}} = \sum_{m=1}^{M_r} \alpha_{\text{sru},r,m} \mathbf{A}_{\text{sru},r,m}^{\text{MP}} \odot \mathbf{F}^H \left(\mathbf{B}_{\text{sru},r,m}^{\text{MP}} \odot \mathbf{C}_{\text{sru},r,m}^{\text{MP}} \odot \mathbf{G}_{\text{RIS},r,m}^{\text{MP}} \odot \mathbf{X} \right), \tag{3.53}$$

where $\mathbf{G}_{\text{RIS},r,m}^{\text{MP}}$ denotes the RIS response of the mth MP related to the rth RIS. Combining all path components and receiver noise, the overall observation matrix is

$$\mathbf{Y} = \mathbf{Y}_{\text{su}}^{\text{LoS}} + \mathbf{Y}_{\text{su}}^{\text{MP}} + \sum_{r=1}^{R} \left(\mathbf{Y}_{\text{sru},r}^{\text{RIS}} + \mathbf{Y}_{\text{sru},r}^{\text{MP}} \right) + \mathbf{N}, \tag{3.54}$$

$$\text{vec}(\mathbf{N}) \sim \mathcal{CN} \left(\mathbf{0}_{\mathbf{k} \times \mathbf{L}}, \sigma^2 \mathbf{I}_{K \times L} \right). \tag{3.55}$$

$$\sigma^2 = N_0 N_f \tag{3.56}$$

$$N_0 = k_{\text{B}} T_0 \tag{3.57}$$

σ^2 is the noise variance per complex OFDM resource element under the unitary OFDM and the total thermal-noise power over bandwidth B would be $B\sigma^2$ in a continuous-time receiver. N_f is the noise figure (NF) of UE, N_0 is the thermal-noise power spectral density and k_{B} is Boltzmann's constant, $T_0 = 290$ K is the reference noise temperature.

3.6 Summary of Assumptions

The system model is developed under the following assumptions, whose detailed derivations are provided in the Appendix.

1. *Static UE and short observation interval:* The UE is assumed to remain static within one observation block, i.e.,

$$\mathbf{p}(t) = \mathbf{p}. \tag{3.58}$$

   During this short interval, the LEO satellite moves with approximately constant velocity,

$$\mathbf{v}_{\text{sat}}(t) \approx \mathbf{v}_{\text{sat}}, \tag{3.59}$$

   and the satellite-to-RIS angular variation is negligible, namely

$$\theta_{\text{rs},r}(LT_{\text{sym}}) - \theta_{\text{rs},r}(0) \approx 0, \tag{3.60}$$

   where L is the number of OFDM symbols in one observation block.
   The observation window is approximately 18.26 ms. For a low-speed UE moving at 1 m/s, the delay within one block is about 0.61 ns, which is negligible compared with the delay resolution 33.3 ns. Compared to the satellite large distance d_{sat}, the satellite velocity and angular variation is much smaller within one observation block.
2. *Asynchronous receiver:* The satellite and the UE are not perfectly synchronized. Therefore, an unknown clock bias δ and an unknown CFO δ_f are included in the delay and Doppler models and need to be estimated.
3. *Far-field plane-wave model:* Due to the large LEO satellite distance d_{sat}, the satellite is assumed to lie in the far field of the RISs and the UE. The RIS–UE path is also modeled under the far-field assumption, so that plane-wave steering vectors can be used for the RIS array response. The RIS aperture is about 0.954 m when the diagonal aperture is used. At $f_c = 2GHz$, the Fraunhofer distance is approximately 12.1 m. Since the RIS–UE distance in the simulation is about 13.72 m, which supports the far-field assumption model.
4. *Doppler assumption:* Since the RISs and the UE are located in a small local region compared with the large satellite distance d_{sat}, the Doppler factors of the LoS and RIS paths are approximately identical. With $\delta_f \ll \nu_{\text{sr},r}$, the Doppler of different paths have such assumptions:

$$\nu_{\text{su}} \approx \nu_{\text{sru},1} \approx \nu_{\text{sru},2}. \tag{3.61}$$

5. *RIS profile configuration:* The RIS phase profiles are assumed to be known at the UE side through RISS-aided positioning protocols. Each RIS profile remains constant within one OFDM symbol and is updated symbol by symbol.
6. *Multipath modeling assumption:* In this work, MP propagation is modeled explicitly rather than represented by an implicit NLoS shadow-fading term. Specifically, SPs are generated around predefined cluster centers, and each MP component is constructed according to its geometric propagation route, including the corresponding delay, Doppler factor, and path gain.

Only single-bounce scatter paths are considered in the MP model. This assumption is adopted because each additional scattering or reflection path introduces extra path loss, and multi-bounce components are expected to be significantly weaker, especially for the already weak RIS paths in the considered simulation setup.
The MP paths are constructed in the channel model, but in the CRB analysis they are regarded additional effective noise into thermal-noise variance σ^2.

$$\sigma_{\text{eff}}^2 = \sigma^2 + P_{\text{MP,avg}}, \tag{3.62}$$

where $P_{\text{MP,avg}}$ denotes the average received power of the injected MP interference. The MP delays, Doppler factors, angles, and complex gains are not explicitly added to the Fisher information matrix (FIM) as additional unknown nuisance parameters, which represents a worthwhile avenue for further research.

4

Methods

This section describes the proposed methods for channel-parameter estimation and positioning method. The channel-parameter estimation procedure estimates LoS channel and RIS channel parameters separately to reduce high-dimension computation. LoS channel estimation algorithm mainly extracts its delay, Doppler and gain values. After removing the LoS part, the RIS branches are separated through a time-orthogonal decoupling strategy. The delay, Doppler and angular information in the RIS branches are extracted based on the decoupled RIS observation signal, A second-stage estimation procedure is then introduced to refine the estimated parameters and improve the robustness of the overall estimation process. Finally, the positioning methods exploit the estimated channel parameters using joint positioning compared.

4.1 Channel-Parameter Estimation

Instead of directly performing a high-dimensional joint maximum likelihood estimation (MLE), a staged estimation method is adopted. The reason is that the complete parameter set contains the LoS delay, LoS Doppler, two RIS delays, two two-dimensional RIS AoDs, three complex channel gains, leading to prohibitively high search complexity.

4.1.1 Complexity Analysis

The complexity of the proposed estimator comes from the sequential estimation of the LoS parameters, RIS path decoupling, the subsequent RIS parameter estimation and second-stage refinement.

- For the LoS path estimator, the complexity mainly comes from the FFT-based delay-Doppler coarse search and the 2D MLE refinement. The FFT-based search scales approximately as $\mathcal{O}(N_K N_L \log_2(N_K N_L))$, where N_K and N_L denote the FFT sizes in the delay and Doppler dimensions, respectively. The 2D MLE refinement has complexity $\mathcal{O}(N_g^2 M_{iter} KL)$. where N_g is the number of grid points per dimension, M_{iter} is the number of refinement iterations.
- For the RIS decoupling, the decoding step requires linear processing over the received resource grid with complexity $\mathcal{O}(KL)$.
- After decoding, each RIS branch is processed independently. For each branch, the 1D FFT delay estimation has complexity $\mathcal{O}(\tilde{L} N_K \log_2 N_K)$, where $\tilde{L} = L/2$ is the number of symbols in each decoded block. The 2D AoD MLE search and

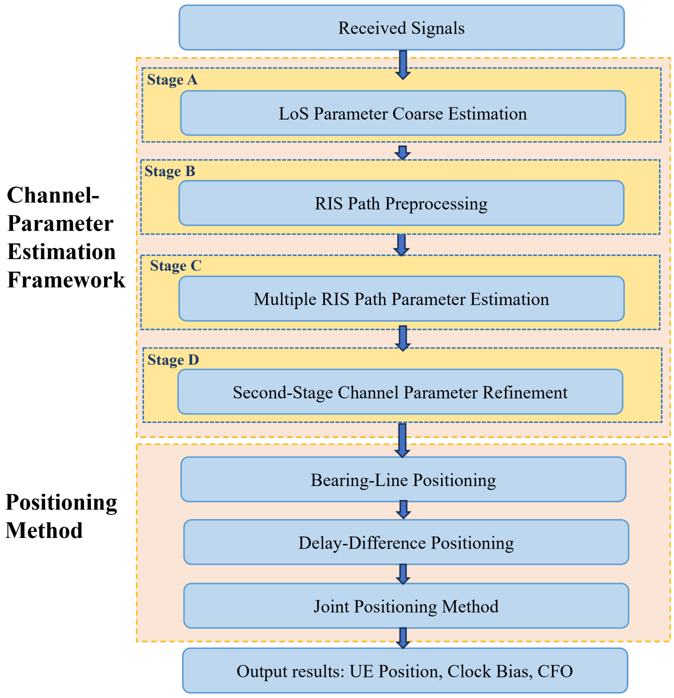

Figure 4.1: The system framework structure of channel estimation and positioning method.

the subsequent 1D delay MLE refinement have complexities $\mathcal{O}(N_g^2 M_{iter} N_r \tilde{L})$ and $\mathcal{O}(N_g M_{iter} K)$, respectively. Since two RIS branches are used, the RIS complexity is approximately twice that of a single-RIS branch.

- In second-stage refinement, the complexity repeats the LoS and RIS parameter estimation steps to increase the computational cost by 2.
- The total algorithm complexity can be calculated by $\mathcal{O}(2(N_K N_L \log_2(N_K N_L) + N_g^2 M_{iter} KL + KL + 2(\tilde{L} N_K \log_2 N_K + N_g^2 M_{iter} N_r \tilde{L} + N_g M_{iter} K)))$,

In contrast, a direct joint grid search would need to estimate the LoS delay-Doppler parameters and the two RIS delay-Doppler-AoD parameter sets simultaneously, which results in an 10D MLE search with complexity scales on the order of $\mathcal{O}(N_g^{10} KL)$. Therefore, the proposed sequential estimation channel estimation strategy drastically reduce the complexity compared with direct joint MLE.

4.1.2 LoS Path Channel Parameter Estimation

Since $|\alpha_{\mathrm{su}}| \gg |\alpha_{\mathrm{sru},r}|$, the LoS path is usually the strongest component in the received signal. Therefore, the RIS paths and MP are first ignored, and the received signal is approximated as LoS-dominated. The LoS delay and Doppler are estimated by a coarse-to-fine procedure: delay is first coarsely estimated using an inverse fast Fourier transform (IFFT) along the subcarrier dimension, Doppler is coarsely estimated using an FFT along the slow-time dimension, and then a two-dimensional local MLE grid refinement is performed.

4.1.2.1 Doppler Elimination

Before the delay estimation, we first need to remove the fast-time Doppler effect and then demodulate the received signal. However, compensating the fast-time Doppler effect requires knowledge of the Doppler effect. Based on the previously mentioned Doppler assumption in Section 3.6, the LoS Doppler shift can be coarsely approximated by the satellite-to-RIS Doppler shift,

$$\nu_{su} \approx \nu_{sr}. \tag{4.1}$$

Based on this approximation, the fast-time Doppler component and the subcarrier-dependent Doppler phase are compensated before performing delay estimation. Specifically, the received signal matrix $\mathbf{Y}$ is first compensated for the fast-time Doppler term as

$$\mathring{\mathbf{Y}} = \mathbf{F}\left(\mathbf{A}_{su}^{*} \odot \mathbf{Y}\right), \tag{4.2}$$

where $\odot$ denotes the Hadamard product and $\mathbf{A}_{su}^{*}$ is the complex conjugate of the estimated fast-time Doppler matrix. Its element can be expressed as

$$[\mathbf{A}_{su}^{*}]_{\kappa,\ell} = e^{-\jmath 2\pi f_c \nu_{su} \kappa/(K\Delta f)}, \tag{4.3}$$

Then, the subcarrier Doppler phase is further removed by

$$\breve{\mathbf{Y}} = \hat{\mathbf{B}}_{\nu_{su}}^{*} \odot \mathring{\mathbf{Y}}, \tag{4.4}$$

$$[\hat{\mathbf{B}}_{\nu_{su}}^{*}]_{k,\ell} = e^{-\jmath 2\pi k \Delta f \nu_{su} \ell T_{\mathrm{sym}}}, \tag{4.5}$$

where $\hat{\mathbf{B}}_{\nu_{su}}^{*}$ is the complex conjugate of the estimated inter-subcarrier Doppler matrix. After these Doppler compensation steps and absorbing constant X into α_{su} in equation 3.50, the remaining LoS signal can be approximately written as

$$\breve{\mathbf{Y}} \approx \alpha_{su}\left(\mathbf{B}_{su} \odot \mathbf{C}_{su}\right) + \mathbf{N}, \tag{4.6}$$

Specifically, their elements are given by

$$[\mathbf{B}_{su}]_{k,\ell} = e^{-\jmath 2\pi k \Delta f \tau_{su}}, [\mathbf{C}_{su}]_{k,\ell} = e^{\jmath 2\pi f_c \nu_{su} \ell T_{\mathrm{sym}}}, \tag{4.7}$$

Since all columns of $\mathbf{B}_{su}$ are identical and all rows of $\mathbf{C}_{su}$ are identical, the compensated LoS signal can be reprsented the following rank-one representation:

$$\breve{\mathbf{Y}} \approx \alpha_{su} \mathbf{b}(\tau_{su}) \mathbf{c}^{T}(\nu_{su}) + \mathbf{N}, \tag{4.8}$$

where the delay steering vector and Doppler steering vector are defined as

$$[\mathbf{b}(\tau_{su})]_{k} = e^{-\jmath 2\pi k \Delta f \tau_{su}}, [\mathbf{c}(\nu_{su})]_{\ell} = e^{\jmath 2\pi f_c \nu_{su} \ell T_{\mathrm{sym}}}. \tag{4.9}$$

4.1.2.2 2D-FFT search

This rank-one structure shows that the subcarrier dimension is primarily governed by the LoS delay, while the slow-time dimension is governed by the LoS Doppler shift. Therefore, the initial estimates of τ_{su} and ν_{su} can be obtained either by a 2D- FFT search or by two separate 1D-FFT searches with non-coherent integration. Under the two-dimensional FFT formulation, the coarse estimates are given by

$$[\hat{\tau}_{su}, \hat{\nu}_{su}] = \arg\max_{\tau,\nu} \left| \mathbf{b}^H(\tau)\breve{\mathbf{Y}}\mathbf{c}^*(\nu) \right|. \tag{4.10}$$

In the simulation, the zero-padded FFT sizes are set to

$$N_K = N_L = 2^{13}, \tag{4.11}$$

where N_K and N_L denote the FFT sizes along the subcarrier and slow-time dimensions, respectively. The corresponding delay–Doppler spectrum is

$$P[i_\tau, i_\nu] = \left| \sum_{l=0}^{L-1} \sum_{k=0}^{K-1} \breve{Y}_{k,l}\, e^{\jmath 2\pi k i_\tau / N_K}\, e^{-\jmath 2\pi l i_\nu / N_L} \right|, \tag{4.12}$$

where

$$i_\tau = 0, \ldots, N_K - 1, \qquad i_\nu = 0, \ldots, N_L - 1. \tag{4.13}$$

The delay–Doppler grid point corresponding to the strongest peak is selected as

$$(i_\tau^\star, i_\nu^\star) = \arg\max_{i_\tau, i_\nu} P[i_\tau, i_\nu]. \tag{4.14}$$

If it's supposed to avoid the computational cost of a full joint 2D search, the separability in (4.10) is exploited to decouple the estimation into two successive 1D-FFT stages. First, the delay spectrum is computed by zero-padding the subcarrier dimension to $N_K = 2^{13}$ and applying an IFFT along the subcarrier dimension:

$$P_\tau[i_\tau] = \sum_{l=0}^{L-1} \left| \sum_{k=0}^{K-1} \breve{Y}_{k,l}\, e^{\jmath 2\pi k i_\tau / N_K} \right|, \qquad i_\tau^\star = \arg\max_{i_\tau} P_\tau[i_\tau]. \tag{4.15}$$

The summation over l is performed non-coherently, which makes the delay estimate less sensitive to the residual Doppler-induced phase rotation across OFDM symbols. After obtaining the coarse delay estimate, the delay-dependent subcarrier phase is compensated and the subcarriers are coherently combined:

$$r_l = \sum_{k=0}^{K-1} \breve{Y}_{k,l}\, e^{\jmath 2\pi k \Delta f \hat{\tau}_{su}}. \tag{4.16}$$

Then, the slow-time sequence is zero-padded to $N_L = 2^{13}$, and a slow-time FFT is applied to obtain the Doppler spectrum:

$$P_\nu[i_\nu] = \left| \sum_{l=0}^{L-1} r_l\, e^{-\jmath 2\pi l i_\nu / N_L} \right|, \qquad i_\nu^\star = \arg\max_{i_\nu} P_\nu[i_\nu]. \tag{4.17}$$

Since the FFT grid points only determine the fractional delay and Doppler within one FFT period, the integer ambiguities are resolved using a known reference geometry. In this work, the reference delay τ_{ref} and Doppler ν_{ref} are obtained from the known satellite–RIS geometry (τ_{sr}, ν_{sr}). Therefore, the coarse delay estimate is computed as

$$\hat{\tau}_{su} = \frac{\lfloor \tau_{\text{ref}} \Delta f \rfloor + i_\tau^\star / N_K}{\Delta f}, \tag{4.18}$$

and the coarse Doppler estimate is computed as

$$\hat{\nu}_{su} = \frac{\lfloor \nu_{\text{ref}} f_c T_{\text{sym}} \rfloor + i_\nu^\star / N_L}{f_c T_{\text{sym}}}. \tag{4.19}$$

4.1.2.3 2D-MLE search

To further improve the estimation accuracy, the coarse FFT estimates $\hat{\tau}_{su}, \hat{\nu}_{su}$ are refined by an iterative 2D-MLE search. The MLE refinement can be formulated as

$$[\hat{\tau}_{su}, \hat{\nu}_{su}] = \arg\min_{\tau,\nu} \left\| \mathbf{\Pi}^\perp_{\mathbf{z}(\tau,\nu)} \mathring{\mathbf{y}} \right\|^2, \tag{4.20}$$

$$\mathring{\mathbf{y}} = \text{vec}\left(\mathring{\mathbf{Y}}\right), \quad \mathbf{z} = \text{vec}\left(\mathbf{Z}\right), \tag{4.21}$$

$$\mathbf{Z} = \mathbf{B}_{su} \odot \mathbf{C}_{su} \odot \mathbf{X}. \tag{4.22}$$

The orthogonal projection matrix is defined as

$$\mathbf{\Pi}^\perp_{\mathbf{z}} = \mathbf{I} - \mathbf{\Pi}_{\mathbf{z}}, \tag{4.23}$$

$$\mathbf{\Pi}_{\mathbf{z}} = \frac{\mathbf{z}\mathbf{z}^H}{\|\mathbf{z}\|^2}. \tag{4.24}$$

At each refinement iteration, the local search region is centered around the current estimate and its width is reduced recursively. Specifically, at the hth refinement iteration, the delay and Doppler search grids are generated as

$$\tau_i^{(h)} = \hat{\tau}^{(h-1)} + \frac{\Delta\tau_i}{2^h}, \qquad \nu_j^{(h)} = \hat{\nu}^{(h-1)} + \frac{\Delta\nu_j}{2^h}, \tag{4.25}$$

where $\hat{\tau}^{(h-1)}$ and $\hat{\nu}^{(h-1)}$ are the delay and Doppler estimates obtained from the previous iteration, and $\Delta\tau_i$ and $\Delta\nu_j$ denote the initial local grid offsets in the delay and Doppler dimensions, respectively.

$$\Delta\tau = \frac{2\tau_{\max}}{N_g - 1}, \qquad \Delta\nu = \frac{2\nu_{\max}}{N_g - 1}, \tag{4.26}$$

For each candidate pair $(\tau_i^{(h)}, \nu_j^{(h)})$, their corresponding complex path gain is estimated as

$$\hat{\alpha}(\tau_i^{(h)}, \nu_j^{(h)}) = \frac{\mathbf{z}^H(\tau_i^{(h)}, \nu_j^{(h)})\mathring{\mathbf{y}}}{\left\|\mathbf{z}(\tau_i^{(h)}, \nu_j^{(h)})\right\|^2}, \tag{4.27}$$

where $(\cdot)^H$ denotes the Hermitian transpose. The log-likelihood form is then evaluated as the negative residual energy and the candidate pair that maximizes the likelihood is selected as the updated estimate value

$$\mathcal{L}(\tau_i^{(h)}, \nu_j^{(h)}) = -\left\| \mathring{\mathbf{y}} - \hat{\alpha}(\tau_i^{(h)}, \nu_j^{(h)}) \mathbf{z}(\tau_i^{(h)}, \nu_j^{(h)}) \right\|^2 . \tag{4.28}$$

$$\left(\hat{\tau}^{(h)}, \hat{\nu}^{(h)}\right) = \arg \max_{\tau_i^{(h)}, \nu_j^{(h)}} \mathcal{L}(\tau_i^{(h)}, \nu_j^{(h)}). \tag{4.29}$$

In general, this recursive refinement improves the delay-Doppler resolution without requiring a dense global two-dimensional search.

4.1.2.4 Estimate LoS channel gain

After obtaining the refined estimates $\hat{\tau}_{su}$ and $\hat{\nu}_{su}$, the LoS channel gain can be estimated by least squares as

$$\hat{\alpha}_{su} = \frac{\mathbf{z}^H \mathring{\mathbf{y}}}{\|\mathbf{z}\|^2}. \tag{4.30}$$

Thus, the LoS accurate path parameter estimates are obtained through a low-complexity coarse-to-fine procedure for the subsequent channel parameter extraction. After LoS path channel estimation, the LoS signal is reconstructed as

$$\hat{\mathbf{y}}_{\mathrm{su}} = \hat{\alpha}_{\mathrm{su}} \mathbf{z}_{\mathrm{su}}(\hat{\tau}_{\mathrm{su}}, \hat{\nu}_{\mathrm{su}}), \tag{4.31}$$

And the received signal subtracts the reconstructed LoS signal, resulting in $\mathbf{y}_{\mathrm{res}}$, which mainly includes RIS signals, MP signals and noise.

$$\mathbf{y}_{\mathrm{res}} = \mathbf{y} - \hat{\mathbf{y}}_{\mathrm{su}}. \tag{4.32}$$

4.1.3 RIS Path Preprocessing

4.1.3.1 RIS Doppler Elimination

Based on the Doppler assumption, the estimated values $\hat{\nu}_{\mathrm{su}}$ is used to eliminate the RIS path Doppler. What's more, both RIS branches have similar Doppler effect, so the terms $\hat{\mathbf{A}}_{\mathrm{sru}}$, $\mathbf{B}_{\hat{\nu}_{\mathrm{sru}}}$ and $\mathbf{C}_{\hat{\nu}_{\mathrm{sru}}}$ denote all RIS Doppler effect.

$$\hat{\nu}_{\mathrm{sru},1} \approx \hat{\nu}_{\mathrm{sru},2} \approx \hat{\nu}_{\mathrm{su}}, \tag{4.33}$$

Using this coarse Doppler estimate, the fast-time Doppler RIS effect in the residual signal is removed by

$$\mathring{\mathbf{Y}}_{\mathrm{RIS-combined}} = \mathbf{F}\left(\hat{\mathbf{A}}^*_{\mathrm{sru}} \odot \mathbf{Y}_{res}\right), \tag{4.34}$$

$\hat{\mathbf{A}}^*_{\mathrm{sru}}$ is the conjugate of the estimated RIS fast-time Doppler matrix with

$$[\hat{\mathbf{A}}^*_{\mathrm{sru}}]_{\kappa,\ell} = \exp\left(-\jmath 2\pi f_c \hat{\nu}_{\mathrm{sru}} \frac{\kappa T}{K}\right). \tag{4.35}$$

Then, the RIS inter-subcarrier Doppler term is compensated as

$$\breve{\mathbf{Y}}_{\mathrm{RIS-combined}} = \mathbf{B}^*_{\hat{\nu}_{\mathrm{sru}}} \odot \mathring{\mathbf{Y}}_{\mathrm{RIS-combined}}, \tag{4.36}$$

$$[\mathbf{B}^*_{\hat{\nu}_{\mathrm{sru}}}]_{k,\ell} = \exp\left(-\jmath 2\pi k \Delta f \hat{\nu}_{\mathrm{sru}} \ell T_{\mathrm{sym}}\right). \tag{4.37}$$

To compensate the slow-time Doppler,

$$\bar{\mathbf{Y}}_{\mathrm{RIS-combined}} = \check{\mathbf{Y}}_{\mathrm{RIS-combined}} \odot \mathbf{C}^*_{\hat{\nu}_{\mathrm{sru}}}, \tag{4.38}$$

$$[\mathbf{C}^*_{\hat{\nu}_{\mathrm{sru}}}]_{k,\ell} = \exp\left(\jmath 2\pi f_c \hat{\nu}_{\mathrm{sru}} \ell T_{\mathrm{sym}}\right). \tag{4.39}$$

4.1.3.2 RIS Path Decoupling

Although time-orthogonal coding schemes have been investigated in several RIS localization studies [39, **?**], these schemes usually include the LoS component in the orthogonal temporal coding process. In the considered LEO localization scenario, however, the direct LoS path is much stronger than the RIS paths, $|\alpha_{\mathrm{su}}| \gg |\alpha_{\mathrm{sru},r}|$. Moreover, the LoS component is first estimated and subtracted in order to extract the dominant LoS channel parameters and avoid its interference with the weak RIS branches. Therefore, in this work, the time-orthogonal coding scheme is applied only to the RIS branches, while the LoS component is processed separately before RIS decoding. The RIS profiles are assumed to be known at the UE through RIS positioning protocols, which adopt time-orthogonal RIS profiles to differentiate independent RIS paths from the others. The signal, with L OFDM symbols, is divided into Γ blocks according to the number of RISs, with each block consisting of $\tilde{L} = \frac{L}{\Gamma}$ OFDM symbols. In this work, $\Gamma = R$. Then, we define a normalized orthogonal code matrix $\mathbf{M} \in \mathbb{C}^{\Gamma \times \Gamma}$ using the rows $\mathbf{m}_r$ using orthogonal columns from a discrete Fourier transform (DFT) matrix $\mathbf{F}_\Gamma \in \mathbb{C}^{\Gamma \times \Gamma}$, whose (i, j)th element is given by

$$[\mathbf{F}_\Gamma]_{i,j} = \exp\left(-\jmath \frac{2\pi}{\Gamma}(i-1)(j-1)\right), \qquad i, j = 1, \ldots, \Gamma. \tag{4.40}$$

The codeword assigned to the rth RIS is selected as one column of $\mathbf{F}_\Gamma$ and is denoted by $\mathbf{m}_r \in \mathbb{C}^R$. Its ith element can be written as

$$[\mathbf{m}_r]_i = \frac{1}{\sqrt{\Gamma}} \exp\left(-\jmath \frac{2\pi}{\Gamma}(i-1)(j-1)\right), \qquad i = 1, \ldots, \Gamma, \tag{4.41}$$

where j denotes the selected DFT column index for the rth RIS. The selected codewords satisfy the orthonormality condition

$$\mathbf{m}_r^{\mathrm{H}} \mathbf{m}_{r'} = \begin{cases} 1, & r = r', \\ 0, & r \neq r', \end{cases} \tag{4.42}$$

The normalized code matrix is given by

$$\mathbf{M} = [\mathbf{m}_1, \ldots, \mathbf{m}_\Gamma], \qquad \mathbf{M}^{\mathrm{H}} \mathbf{M} = \mathbf{I}_\Gamma. \tag{4.43}$$

For OFDM signal, the RIS configuration of the rth RIS during the $\tilde{l}$th OFDM symbol of the ith block can thus be expressed as

$$\boldsymbol{\omega}_{r,(i-1)\tilde{L}+\tilde{l}} = m^*_{r,i} \boldsymbol{\omega}_{r,\tilde{l}}, \qquad i = 1, \ldots, \Gamma, \tag{4.44}$$

The vector $\boldsymbol{\omega}_{r,\tilde{l}} \in \mathbb{C}^N$ denotes the reference RIS configuration of the rth RIS during the $\tilde{l}$th OFDM symbol in the first block and the vector $\boldsymbol{\omega}_{r,(i-1)\tilde{L}+\tilde{l}}$ denotes the i th block RIS controller vector of rth RIS path.
For the double-RIS case, two mutually orthogonal codewords are sufficient and the corresponding time-orthogonal code matrix is given by
The corresponding time-orthogonal code matrix is given by

$$\mathbf{M} = \frac{1}{\sqrt{2}} \begin{bmatrix} 1 & 1 \\ 1 & -1 \end{bmatrix}. \tag{4.45}$$

The two RIS branches are assigned two orthogonal codewords as

$$\mathbf{m}_1 = \frac{1}{\sqrt{2}} \begin{bmatrix} 1 & 1 \end{bmatrix}^{\mathrm{T}}, \qquad \mathbf{m}_2 = \frac{1}{\sqrt{2}} \begin{bmatrix} 1 & -1 \end{bmatrix}^{\mathrm{T}}. \tag{4.46}$$

Time-orthogonal Decoding
After the Doppler elimination operation, the Doppler-compensated signal block will be as follows:

$$\bar{\mathbf{Y}}^{(i)}_{\mathrm{RIS-combined}} = \bar{\mathbf{Y}}_{\mathrm{RIS-combined}} \left(:, \, (i-1)\tilde{L} : i\tilde{L} - 1 \right) \in \mathbb{C}^{K \times \tilde{L}}. \tag{4.47}$$

Following the inverse operation of the time-orthogonal encoding scheme, the rth RIS branch is decoded as

$$\breve{\mathbf{Y}}_{\mathrm{sru},r} = \sum_{i=1}^{\Gamma} m_{r,i} \bar{\mathbf{Y}}^{(i)}_{\mathrm{RIS-combined}}, \tag{4.48}$$

For the double-RIS case, the two decoded RIS branches are explicitly written as

$$\breve{\mathbf{Y}}_{\mathrm{sru},1} = \bar{\mathbf{Y}}^{(1)}_{\mathrm{RIS-combined}} + \bar{\mathbf{Y}}^{(2)}_{\mathrm{RIS-combined}} \tag{4.49}$$

$$\breve{\mathbf{Y}}_{\mathrm{sru},2} = \bar{\mathbf{Y}}^{(1)}_{\mathrm{RIS-combined}} - \bar{\mathbf{Y}}^{(2)}_{\mathrm{RIS-combined}} \tag{4.50}$$

Theoretically, $\breve{\mathbf{Y}}_{\mathrm{sru},1}$ denotes the received signal on RIS1 path while $\breve{\mathbf{Y}}_{\mathrm{sru},2}$ denotes the received signal on RIS2 path. And these two received signal are independently addressed by following RIS path estimation algorithm.

4.1.4 RIS Path Channel Parameter Estimation

After Doppler compensation and time-orthogonal decoding, we estimate each RIS path independently. The r-th RIS signal can be approximately expressed as

$$\breve{\mathbf{Y}}_{sru,r} \approx \alpha_{sru,r} \left(\mathbf{B}_{sru,r} \odot \mathbf{G}_{\mathrm{RIS},r} \right) + \mathbf{N} \tag{4.51}$$

Here, $\alpha_{sru,r}$ denotes the complex channel gain of the r-th RIS path, $\mathbf{B}_{sru,r}$ is the delay-induced subcarrier phase matrix affected by $\tau_{sru,r}$, and $\mathbf{G}_{\mathrm{RIS},r}$ denotes RIS response matrix affected by the unknown AoD $\theta_{ru,r}$.

4.1.4.1 1D-FFT Delay Coarse Estimation.

The RIS path delay is first coarsely estimated through a 1D FFT-based search with non-coherent integration over the slow-time dimension:

$$\hat{\tau}_{sru,r} = \arg\max_{\tau} \sum_{\ell=0}^{\tilde{L}-1} \left|\mathbf{b}^H(\tau)\breve{y}_{sru,r,\ell}\right|, \tag{4.52}$$

where $\breve{y}_{sru,r,\ell}$ denotes the ℓ-th column of $\breve{\mathbf{Y}}_{sru,r}$. The delay is first coarsely estimated by applying a zero-padded 1D-FFT along the subcarrier dimension. In this work, the zero-padded FFT size is set to $N_K = 2^{13}$ The corresponding delay spectrum for the rth RIS branch is computed as

$$P_{\tau,r}[i_\tau] = \sum_{\ell=0}^{\tilde{L}-1} \left|\sum_{k=0}^{K-1} \breve{Y}_{sru,r,k,\ell} e^{\jmath 2\pi k i_\tau / N_K}\right|, \qquad i_\tau = 0, \ldots, N_K - 1. \tag{4.53}$$

The delay grid point corresponding to the strongest peak is selected as

$$i^\star_{\tau,r} = \arg\max_{i_\tau} P_{\tau,r}[i_\tau]. \tag{4.54}$$

Since the FFT grid only determines the fractional delay within one subcarrier-spacing period, the known satellite-to-RIS delay $\tau_{sr,r}$ is used to resolve the ambiguity. Specifically, the coarse estimate of the RIS-to-UE delay is computed as

$$\hat{\tau}_{ru,r} = \frac{i^\star_{\tau,r}/N_K - (\tau_{sr,r}\Delta f - \lfloor \tau_{sr,r}\Delta f \rfloor)}{\Delta f}. \tag{4.55}$$

Finally, the coarse total RIS path delay can be reconstructed as

$$\hat{\tau}_{sru,r} = \tau_{sr,r} + \hat{\tau}_{ru,r}. \tag{4.56}$$

4.1.4.2 2D-MLE AoD Estimation

The estimated coarse delay $\hat{\tau}_{sru,r}$ is then used to coherently integrate the RIS residual signal over the subcarrier dimension:

$$\breve{\mathbf{y}}_{\mathrm{AoD},r} = \breve{\mathbf{Y}}^T_{sru,r}\mathbf{b}^*(\hat{\tau}_{sru,r}) \in \mathbb{C}^{\tilde{L}}. \tag{4.57}$$

Given this integrated slow-time observation, the azimuth and elevation AoD of the r-th RIS path are estimated by solving the following 2D MLE problem:

$$\left[\hat{\theta}^{az}_{ru,r}, \hat{\theta}^{el}_{ru,r}\right] = \arg\min_{\theta^{az}_{ru,r}, \theta^{el}_{ru,r}} \left\|\mathbf{\Pi}^\perp_{\mathbf{z}_{\mathrm{AoD},r}} \breve{\mathbf{y}}_{\mathrm{AoD},r}\right\|^2, \tag{4.58}$$

For each candidate AoD pair $(\theta^{az}, \theta^{el})$, the corresponding RIS response template is $\mathbf{z}_{\mathrm{AoD},r} = \mathbf{G}_{\mathrm{RIS},r}(\theta^{az}, \theta^{el})$. At each refinement iteration, the local search region is centered around the current AoD estimate and its width is reduced recursively. Specifically, at the h-th refinement iteration, the azimuth and elevation search grids are generated as

$$\theta^{az,(h)}_i = \hat{\theta}^{az,(h-1)}_{ru,r} + \frac{\Delta\theta^{az}_i}{2^h}, \qquad \theta^{el,(h)}_j = \hat{\theta}^{el,(h-1)}_{ru,r} + \frac{\Delta\theta^{el}_j}{2^h}, \tag{4.59}$$

where $\hat{\theta}_{ru,r}^{az,(h-1)}$ and $\hat{\theta}_{ru,r}^{el,(h-1)}$ are the AoD estimates obtained from the previous iteration, and $\Delta\theta_i^{az}$ and $\Delta\theta_j^{el}$ denote the initial local grid offsets in the azimuth and elevation dimensions, respectively. The initial angular resolutions are given by

$$\Delta\theta^{az} = \frac{2\theta_{\max}}{N_g - 1}, \qquad \Delta\theta^{el} = \frac{2\theta_{\max}}{N_g - 1}, \tag{4.60}$$

where N_g is the number of grid points in each dimension.
The corresponding complex path gain is estimated in closed form by least squares as

$$\hat{\alpha}_{AoD,r}\left(\theta_i^{az,(h)}, \theta_j^{el,(h)}\right) = \frac{\mathbf{z}_{AoD,r}^H\left(\theta_i^{az,(h)}, \theta_j^{el,(h)}\right)\breve{\mathbf{y}}_{\mathrm{AoD},r}}{\left\|\mathbf{z}_{AoD,r}\left(\theta_i^{az,(h)}, \theta_j^{el,(h)}\right)\right\|^2}. \tag{4.61}$$

The log-likelihood is evaluated as the negative residual energy:

$$\mathcal{L}_{AoD,r}\left(\theta_i^{az,(h)}, \theta_j^{el,(h)}\right) = -\left\|\breve{\mathbf{y}}_{\mathrm{AoD},r} - \hat{\alpha}_{AoD,r}\left(\theta_i^{az,(h)}, \theta_j^{el,(h)}\right)\mathbf{z}_{AoD,r}\left(\theta_i^{az,(h)}, \theta_j^{el,(h)}\right)\right\|^2. \tag{4.62}$$

The candidate AoD pair that maximizes the likelihood is selected as the updated estimate:

$$\left(\hat{\theta}_{ru,r}^{az,(h)}, \hat{\theta}_{ru,r}^{el,(h)}\right) = \arg\max_{\theta_i^{az,(h)},\theta_j^{el,(h)}} \mathcal{L}_{AoD,r}\left(\theta_i^{az,(h)}, \theta_j^{el,(h)}\right). \tag{4.63}$$

4.1.4.3 1D-MLE Delay Refinement

After the AoD is estimated, the RIS response vector $\hat{\mathbf{G}}_{\mathrm{RIS},r}$ is reconstructed and used to coherently integrate the RIS residual signal over the slow-time dimension:

$$\breve{\mathbf{y}}_{\tau,r} = \breve{\mathbf{Y}}_{sru,r}\hat{\mathbf{G}}_{\mathrm{RIS},r}^{*} \in \mathbb{C}^K. \tag{4.64}$$

The RIS-related delay is then refined through a one-dimensional MLE search:

$$\hat{\tau}_{ru,r} = \arg\min_{\tau}\left\|\mathbf{\Pi}_{\mathbf{z}_{\tau,r}}^{\perp}\breve{\mathbf{y}}_{\tau,r}\right\|^2 - \tau_{sr,r}, \tag{4.65}$$

where $\tau_{sr,r}$ denotes the known delay from satellite-to-RIS, and the template $\mathbf{z}_{\tau,r} = \mathbf{b}(\tau_{sru,r})$ is the delay steering vector corresponding to the candidate RIS-assisted delay. At each refinement iteration, the local delay search region is centered around the current delay estimate and its width is reduced recursively. Specifically, at the h-th refinement iteration, the RIS–UE delay search grid is generated as

$$\tau_{ru,r,i}^{(h)} = \hat{\tau}_{ru,r}^{(h-1)} + \frac{\Delta\tau_i}{2^h}, \tag{4.66}$$

where $\hat{\tau}_{ru,r}^{(h-1)}$ is the delay estimate obtained from the previous iteration, and $\Delta\tau_i$ denotes the initial local grid offset in the delay dimension. The initial delay resolution is given by

$$\Delta\tau = \frac{2\tau_{\max}}{N_g - 1}, \tag{4.67}$$

where N_g is the number of grid points.

For each candidate delay $\tau_{ru,r,i}^{(h)}$, the corresponding total RIS-assisted path delay is

$$\tau_{sru,r,i}^{(h)} = \tau_{sr,r} + \tau_{ru,r,i}^{(h)}. \tag{4.68}$$

The delay-domain template is then generated as

$$\mathbf{z}_{\tau,r}\left(\tau_{ru,r,i}^{(h)}\right) = \mathbf{b}\left(\tau_{sr,r} + \tau_{ru,r,i}^{(h)}\right). \tag{4.69}$$

The corresponding complex path gain is estimated in closed form by least squares as

$$\hat{\alpha}_{\tau,r}\left(\tau_{ru,r,i}^{(h)}\right) = \frac{\mathbf{z}_{\tau,r}^{H}\left(\tau_{ru,r,i}^{(h)}\right)\breve{\mathbf{y}}_{\tau,r}}{\left\|\mathbf{z}_{\tau,r}\left(\tau_{ru,r,i}^{(h)}\right)\right\|^{2}}. \tag{4.70}$$

The log-likelihood is evaluated as the negative residual energy:

$$\mathcal{L}_{\tau,r}\left(\tau_{ru,r,i}^{(h)}\right) = -\left\|\breve{\mathbf{y}}_{\tau,r} - \hat{\alpha}_{\tau,r}\left(\tau_{ru,r,i}^{(h)}\right)\mathbf{z}_{\tau,r}\left(\tau_{ru,r,i}^{(h)}\right)\right\|^{2}. \tag{4.71}$$

The candidate delay that maximizes the likelihood is selected as the updated estimate:

$$\hat{\tau}_{ru,r}^{(h)} = \arg\max_{\tau_{ru,r,i}^{(h)}} \mathcal{L}_{\tau,r}\left(\tau_{ru,r,i}^{(h)}\right). \tag{4.72}$$

4.1.4.4 Estimate RIS complex gain

Finally, with the refined delay and AoD estimates, the complex channel gain of the r-th RIS path is estimated by least squares as

$$\hat{\alpha}_{sru,r} = \frac{\mathbf{z}_{\tau,l}^{H}\breve{\mathbf{y}}_{\tau,r}}{\left\|\mathbf{z}_{\tau,r}\right\|^{2}}. \tag{4.73}$$

4.1.5 Second-Stage Refinement

In the multi-RIS localization model, the estimated channel parameters may still be affected by residual interference for several reasons. First, the LoS signal is usually much stronger than the RIS-reflected signals. Therefore, even a small LoS estimation error may leave residual components in the received signal and contaminate the subsequent RIS parameter estimation. Second, although multiple RISs are separated by time-orthogonal coding, imperfect LoS subtraction and residual inter-RIS leakage may still introduce interference into the channel parameter estimation process. Third, MP components may interfere with both the LoS and RIS signals because they have similar delay-Doppler structures and signal formats.

To reduce these residual errors, a second-stage refinement is applied. Specifically, the RIS signals are reconstructed using the first-stage estimates and then subtracted from the received signal to obtain a cleaner observation for further parameter refinement.

$$\hat{\mathbf{y}}_{\mathrm{sru},r} = \hat{\rho}_{\mathrm{sru},r}\mathbf{z}_{\mathrm{sru},r}(\hat{\tau}_{\mathrm{ru},r}, \hat{\theta}_{r}, \hat{\phi}_{r}), \tag{4.74}$$

They are then subtracted from the original received signal:

$$\mathbf{y}_{\mathrm{clean}} = \mathbf{y} - \sum_{r=1}^{R}\hat{\mathbf{y}}_{\mathrm{sru},r}. \tag{4.75}$$

The LoS delay and Doppler parameters, $(\hat{\tau}_{\text{su}}^{(2)}, \hat{\nu}_{\text{su}}^{(2)})$, are then re-estimated from the cleaned observation $\mathbf{y}_{\text{clean}}$. Based on the updated LoS estimates, the RIS parameter estimation procedure is repeated to obtain the refined estimates $\hat{\tau}_{\text{ru},r}^{(2)}$, $\hat{\theta}_r^{(2)}$, and $\hat{\phi}_r^{(2)}$. In the current implementation, the second-stage refinement is applied once after the initial LoS and RIS parameter estimation. It is designed as a fixed refinement step rather than an iterative outer-loop procedure; therefore, no additional convergence criterion is introduced.

4.2 Positioning Method

After the channel parameters are estimated, the UE position is estimated from the geometric constraints provided by the RIS paths. The estimated RIS AoD provides angular bearing-line constraints, while the delay difference between the direct LoS path and each RIS path provides range-related constraints. Accordingly, two positioning methods are considered: bearing-line (BL) localization and delay-difference localization, also denoted by TP. The joint positioning method combines the robustness of bearing-line localization at low SNR and the improved range resolution of delay-difference localization at high SNR, based on an SNR-dependent threshold rule.

4.2.1 Bearing-Line Localization

Bearing-line localization follows the principle of triangulation, where the UE position is inferred from angular measurements obtained at known RISs. Base on the previous content about the triangulation localization, the bearing line generated by the r-th RIS is defined as

$$\mathbf{I}_r(d_r) = \mathbf{p}_{R,r} + d_r \hat{\mathbf{u}}_r, \tag{4.76}$$

In the presence of angle estimation errors, the bearing lines from different RISs may not intersect exactly. Following the triangulation formulation, the UE position can be estimated by minimizing the weighted perpendicular distance to all bearing lines. The projection matrix onto the plane perpendicular to $\hat{\mathbf{u}}_r$ is

$$\mathbf{P}_r = \mathbf{I} - \hat{\mathbf{u}}_r \hat{\mathbf{u}}_r^T. \tag{4.77}$$

For any candidate position $\mathbf{p}$, the vector $\mathbf{P}_r(\mathbf{p} - \mathbf{p}_{R,r})$ is the perpendicular residual from $\mathbf{p}$ to the r-th bearing line. The bearing-line estimate is then obtained by solving

$$\hat{\mathbf{p}}_{\text{BL}} = \arg\min_{\mathbf{p}} \sum_{r=1}^{R} w_{\theta,r} \left\| \mathbf{P}_r \left(\mathbf{p} - \mathbf{p}_{R,r} \right) \right\|^2, \tag{4.78}$$

where $w_{\theta,r}$ is the weighting coefficient of the angular measurement from the r-th RIS. The corresponding weighted least-squares solution is

$$\hat{\mathbf{p}}_{\text{BL}} = \left(\sum_{r=1}^{R} w_{\theta,r} \mathbf{P}_r \right)^{-1} \left(\sum_{r=1}^{R} w_{\theta,r} \mathbf{P}_r \mathbf{p}_{R,r} \right). \tag{4.79}$$

In the double-RIS implementation, uniform weights are used, and this expression is equivalently implemented in matrix form as

$$\hat{\mathbf{p}}_{\mathrm{BL}} = \left(\mathbf{A}_{\mathrm{BL}}^T \mathbf{A}_{\mathrm{BL}}\right)^{-1} \mathbf{A}_{\mathrm{BL}}^T \mathbf{b}_{\mathrm{BL}}, \tag{4.80}$$

with

$$\mathbf{A}_{\mathrm{BL}} = \begin{bmatrix} \mathbf{P}_1 \\ \mathbf{P}_2 \end{bmatrix}, \qquad \mathbf{b}_{\mathrm{BL}} = \begin{bmatrix} \mathbf{P}_1 \mathbf{p}_{R,1} \\ \mathbf{P}_2 \mathbf{p}_{R,2} \end{bmatrix}. \tag{4.81}$$

This bearing-line solution provides a robust initial position estimate when the delay estimates are unreliable.

4.2.2 Delay-Difference Localization

The delay-difference localization method is motivated by range-difference-based multilateration using difference between $\tau_{sru,r}$ and τ_{su}. In the considered LEO-RIS-UE geometry, the delay difference between the RIS path and the LoS path satisfies

$$\tau_{sru,r} - \tau_{su} = \frac{d_{sr,r} + d_{ru,r} - d_{su}}{c}, \tag{4.82}$$

Using the estimated LoS delay and the estimated RIS–UE delay, the measured range-difference for the r-th RIS is defined as

$$\hat{\rho}_r = c\left(\hat{\tau}_{sru,r} - \hat{\tau}_{su}\right) = c\left(\tau_{sr,r} + \hat{\tau}_{ru,r} - \hat{\tau}_{su}\right), \tag{4.83}$$

The distance parameter d_r, from RIS to UE, is estimated through the following 1D nonlinear least-squares problem:

$$\hat{d}_r = \arg\min_{d_r} \left[d_{sr,r} + d_r - \|\mathbf{p}_{sat} - (\mathbf{p}_{R,r} + d_r \hat{\mathbf{u}}_r)\| - \hat{\rho}_r\right]^2. \tag{4.84}$$

The corresponding delay-difference position estimate from the r-th RIS is

$$\hat{\mathbf{p}}_{\mathrm{TP},r} = \mathbf{p}_{R,r} + \hat{d}_r \hat{\mathbf{u}}_r. \tag{4.85}$$

For the double-RIS case considered in this work, two independent delay-difference position estimates are obtained. They are fused by a weighted average:

$$\hat{\mathbf{p}}_{\mathrm{TP}} = \sum_{r=1}^{R} \omega_{\mathrm{TP},r} \hat{\mathbf{p}}_{\mathrm{TP},r}, \qquad \sum_{r=1}^{R} \omega_{\mathrm{TP},r} = 1, \tag{4.86}$$

where $\omega_{\mathrm{TP},r}$ denotes the fusion weight of the r-th delay-difference estimate.

4.2.3 Joint Positioning

The bearing-line and delay-difference methods have complementary advantages. The bearing-line estimate mainly depends on the angular information extracted from the RIS paths, and is therefore more robust when the RIS delay estimate is noisy or biased. This is particularly useful in the low-SNR region, where the delay peak is more sensitive to noise, residual interference, and MP components. In contrast,

when the SNR is sufficiently high, the delay estimate becomes more reliable, and the delay-difference method can provide additional range-related information.
Therefore, an SNR-threshold strategy is adopted to select between the bearing-line estimate and the delay-difference estimate:

$$\hat{\mathbf{p}} = \begin{cases} \hat{\mathbf{p}}_{\mathrm{BL}}, & \mathrm{SNR} < \gamma_{\mathrm{th}}, \\ \hat{\mathbf{p}}_{\mathrm{TP}}, & \mathrm{SNR} \geq \gamma_{\mathrm{th}}. \end{cases} \tag{4.87}$$

In this work, the switching threshold is operated through the transmit-power sweeping variable. Specifically, the threshold is set to $P_{\mathrm{th}} = -30$ dB, which corresponds to approximately SNR $= 40$ dB in the reported simulation results. Below this threshold, the bearing-line estimate is selected because the RIS-path delay estimate may still be unreliable and can suffer from large estimation errors. Above this threshold, the delay-difference estimate is used, since the RIS-path delay is generally expected to provide more reliable range-related information at sufficiently high SNR.
Finally, the clock bias and CFO are estimated as

$$\hat{\delta} = \hat{\tau}_{\mathrm{su}} - \frac{||\hat{\mathbf{p}} - \mathbf{p}_{sat}||}{c}, \tag{4.88}$$

and

$$\hat{\delta}_f = \hat{\nu}_{\mathrm{su}} - \frac{\mathbf{v}_{\mathrm{sat}}^T (\hat{\mathbf{p}} - \mathbf{p}_{sat})}{||\hat{\mathbf{p}} - \mathbf{p}_{sat}||c}, \tag{4.89}$$

where $\hat{\delta}$ denotes the estimated time bias, $\hat{\delta}_f$ denotes the estimated CFO, d_{su} is the satellite-to-UE distance, $\mathbf{v}_{\mathrm{sat}}$ is the satellite velocity vector, and $\mathbf{u}(\theta_{\mathrm{su}})$ is the unit direction vector of the LoS path.

Algorithm 1 Staged Channel-Parameter Estimation for multi-RIS Localization

INPUTS Received signal $\mathbf{Y}$, pilot matrix $\mathbf{X}$, Time-orthogonal code Matrix $\mathbf{M}$
OUTPUTS Estimated LoS parameters $(\hat{\tau}_{\mathrm{su}}, \hat{\nu}_{\mathrm{su}})$ and RIS path parameters $\{\hat{\tau}_{\mathrm{ru},r}, \hat{\theta}^{el}_{ru,r}, \hat{\theta}^{az}_{ru,r}\}_{r=1}^{R}$.
Stage-A: LoS Parameter Coarse Estimation
Doppler Compensation with $\nu_{su} \approx \nu_{sr}$.
2D FFT search: coarse estimates $(\hat{\tau}_{\mathrm{su}}, \hat{\nu}_{\mathrm{su}})$.
2D MLE search: Refine the LoS delay and Doppler $(\hat{\tau}_{\mathrm{su}}, \hat{\nu}_{\mathrm{su}})$
Estimate the LoS complex gain $\hat{\alpha}_{\mathrm{su}}$ and remove LoS part $\hat{\mathbf{y}}_{\mathrm{su}}$
Stage-B:RIS Path Preprocessing
Compensate Doppler phases using $\hat{\nu}_{\mathrm{sru},1} \approx \hat{\nu}_{\mathrm{sru},2} \approx \hat{\nu}_{\mathrm{su}}$.
Decode the RIS branches by the time-orothogoanl code:$\tilde{\mathbf{Y}}_{sru,r}$
Stage-C: RIS Path Parameter Estimation
for $r = 1, 2, ..R$ **do**
    1D FFT Search: Coarse estimate of $\hat{\tau}_{ru,r}$
    2D MLE search: Estimate the RIS AoD by 2D-MLE:$(\hat{\theta}^{el}_{ru,r}, \hat{\theta}^{az}_{ru,r})$
    1D MLE search: Refine the RIS–UE delay $\hat{\tau}_{\mathrm{ru},r}$
    Estimate RIS complex gain: the RIS complex gain $\hat{\alpha}_{sru,r}$
end for
Stage-D: Second-Stage Refinement
Reconstruct the estimated RIS signals $\hat{\mathbf{Y}}_{\mathrm{sru},r}$.
Remove RIS components from the original observation $\mathbf{Y}_{\mathrm{clean}}$.
Re-estimate the LoS delay and Doppler $(\hat{\tau}^{(2)}_{\mathrm{su}}, \hat{\nu}^{(2)}_{\mathrm{su}})$.
Repeat the channel estimation algorithm $\{\hat{\tau}^{(2)}_{\mathrm{ru},r}, (\hat{\theta}^{el}_{ru,r}, \hat{\theta}^{az}_{ru,r})^{(2)}\}_{r=1}^{R}$
return $(\hat{\tau}_{\mathrm{su}}, \hat{\nu}_{\mathrm{su}})$ and $\{\hat{\tau}_{\mathrm{sru},r}, (\hat{\theta}^{el}_{sru,r}, \hat{\theta}^{az}_{sru,r})\}_{r=1}^{R}$.

Algorithm 2 Multi-RIS Positioning Algorithm

INPUT Estimated LoS delay $(\hat{\tau}_{\mathrm{su}}, \hat{\nu}_{\mathrm{su}})$, RIS-path delays $\{\hat{\tau}_{\mathrm{sru},r}\}_{r=1}^{R}$, RIS AoDs $(\hat{\theta}_{sru,r}^{el}, \hat{\theta}_{sru,r}^{az})^{(2)}\}_{r=1}^{R}$.
OUTPUT UE position estimate $\hat{\mathbf{p}}$, clock-bias estimate $\hat{\delta}$, and CFO estimate $\hat{\delta}_f$.
Stage-A: Bearing-Line Positioning
for $r = 1, 2..R$ **do**
  Construct the bearing line from the rth RIS:$\mathbf{I}_r : \mathbf{p} = \mathbf{p}_{R,r} + d_r \hat{\mathbf{u}}_r$.
  Construct the projection matrix:$\mathbf{P}_r = \mathbf{I} - \hat{\mathbf{u}}_r \hat{\mathbf{u}}_r^T$.
end for
Estimate the UE position using the least-squares intersection of the bearing lines: $\hat{\mathbf{p}}_{\mathrm{BL}} = \left(\sum_{r=1}^{R} w_{\theta,r} \mathbf{P}_r\right)^{-1} \left(\sum_{r=1}^{R} w_{\theta,r} \mathbf{P}_r \mathbf{p}_{R,r}\right)$.
Stage-B: Delay-Difference Positioning
for $r = 1, 2..R$ **do**
  Construct the delay-difference range term: $\hat{\rho}_r = c\left(\hat{\tau}_{sru,r} - \hat{\tau}_{su}\right) = c\left(\tau_{sr,r} + \hat{\tau}_{ru,r} - \hat{\tau}_{su}\right)$,
  Estimate the RIS-to-UE range by one-dimensional optimization: $\hat{d}_r = \arg\min_{d_r} \left[d_{sr,r} + d_r - \|\mathbf{p}_{sat} - (\mathbf{p}_{R,r} + d_r \hat{\mathbf{u}}_r)\| - \hat{\rho}_r\right]^2$
  Obtain the estimated delay-difference position from the rth RIS:

$$\hat{\mathbf{p}}_{\mathrm{TP},r} = \mathbf{p}_{R,r} + \hat{d}_r \hat{\mathbf{u}}_r.$$

end for
Fuse the estimated positions from multiple RISs:

$$\hat{\mathbf{p}}_{\mathrm{TP}} = \sum_{r=1}^{R} \omega_{\mathrm{TP},r} \hat{\mathbf{p}}_{\mathrm{TP},r}, \qquad \sum_{r=1}^{R} \omega_{\mathrm{TP},r} = 1.$$

Stage-C: Joint Positioning
Combine two estimated positions according to the SNR threshold:

$$\hat{\mathbf{p}} = \begin{cases} \hat{\mathbf{p}}_{\mathrm{BL}}, & \mathrm{SNR} < \gamma_{\mathrm{th}}, \\ \hat{\mathbf{p}}_{\mathrm{TP}}, & \mathrm{SNR} \geq \gamma_{\mathrm{th}}. \end{cases}$$

Estimate the clock bias: $\hat{\delta} = \hat{\tau}_{\mathrm{su}} - \frac{\|\hat{\mathbf{p}} - \mathbf{p}_{\mathrm{sat}}\|}{c}$.
Estimate the CFO factor using the LoS Doppler relation: $\hat{\delta}_f = \hat{\nu}_{\mathrm{su}} - \frac{\mathbf{v}_{\mathrm{sat}}^T(\hat{\mathbf{p}} - \mathbf{p}_{\mathrm{sat}})}{c\|\hat{\mathbf{p}} - \mathbf{p}_{\mathrm{sat}}\|}$.
return Final UE position estimate $\hat{\mathbf{p}}$, clock-bias estimate $\hat{\delta}$, and CFO estimate $\hat{\delta}_f$.

5

Experiments and Results

This section presents the simulation setup, experiment metrics and numerical results to evaluate the proposed positioning method. First, the simulation setup explains the values of simulation experiment parameters described in the geometric model and channel model. Second, the experiment evaluation metrics, including CRB and RMSE, are introduced to provide both theoretical and empirical assessments of the estimation and positioning accuracy. The CRB characterizes the theoretical lower bound, while the RMSE measures the practical performance obtained from Monte Carlo simulations. Finally, the experiment results and ablation studies are presented to validate the effectiveness of the proposed method and to illustrate the contribution of each key component.

5.1 Simulation Setup

The experiments are conducted in MATLAB using LEO NTN parameters based on 3GPP TR 38.821 (Rel-16) Scenario C1–Set 1–Case 9 [16]. An SNR scanning methodology is also employed to assess localization and generate CRB and RMSE curves to evaluate estimation performance.

5.1.1 Geometry and Deployment Parameters

This model captures the dominant large-scale propagation effects relevant to S-band LEO downlink localization. The carrier frequency is set to $f_c = 2$ GHz, corresponding to a wavelength of $\lambda = c/f_c$. The LEO satellite is located at an orbital altitude of 600 km, with azimuth and elevation angles set to $(90°, 45°)$. The UE is placed at $\mathbf{p} = [0,\ 10,\ 1.5]^T$ m , while the RISs are deployed at fixed known positions, $\mathbf{p}_{R,1} = [4,\ 0,\ 10]^T$ m, $\mathbf{p}_{R,2} = [-4,\ 0,\ 10]^T$ m and $\mathbf{p}_{R,3} = [-6,\ 0,\ 8]^T$ m. The OFDM waveform uses $K = 2000$ subcarriers, $L = 256$ OFDM symbols, and a subcarrier spacing of $\Delta f = 15$ kHz, resulting in a system bandwidth of $B = K\Delta f = 30$ MHz. The useful OFDM symbol duration is $T = 1/\Delta f$, and the full symbol duration is $T_{\text{sym}} = (1 + 0.07)T$, where the cyclic prefix duration is $T_{\text{CP}} = 0.07T$. The clock bias is $\delta = 1$ ns, and the CFO factor is $\delta_f = 10^{-6}$.

5.1.2 Transmit Energy

The large-scale loss terms used in the link-budget model are fixed throughout the simulations. Specifically, the atmospheric scintillation loss is set to $PL_s = 2.2$ dB, the shadow fading margin is set to $SF = 3$ dB, and the atmospheric gas attenuation is set to $PL_g = 0.1$ dB. These values are kept constant for all transmit-power levels so that the effect of the power sweep can be evaluated under the same propagation condition. To evaluate the impact of satellite transmit power, a transmit-power offset is swept around the nominal 3GPP reference value. The nominal reference power is set to $P_{\text{3GPP}} = 54$ dBm, as given by The total transmit power level is expressed as

$$P_{\text{tot}}[\text{dBm}] = P_{\text{3GPP}}[\text{dBm}] + P_{\text{sweep}}[\text{dB}], \tag{5.1}$$

where P_{sweep} is the power offset used to generate different received SNR levels. In the simulations, P_{sweep} is swept from -40 dB to 10 dB with a step size of 5 dB. The transmitted pilot symbols are deterministic and have constant amplitude over all occupied subcarriers and OFDM symbols.

$$x_{k,l} = x = \sqrt{\frac{P_{\text{tot}}}{B}}, \qquad k = 0, \ldots, K-1, \quad l = 0, \ldots, L-1, \tag{5.2}$$

where P_{tot} is the linear transmit power in watts and $B = 30$ MHz is the occupied bandwidth. The thermal noise $\sigma^2 = N_0 N_f$ is generated by a noise power spectral density of $N_0 = -174$ dBm/Hz, together with a receiver noise figure of $N_f = 7$ dB. Thus, for each value of P_{sweep}, the received SNR changes only due to the transmit-power scaling, while the propagation geometry, RIS configuration, and noise model remain fixed. For each transmit power level, the corresponding received signal-to-noise ratio (SNR) is computed by accounting for both the direct LoS component and the RIS components. For a system with R RISs, the total SNR is defined as

$$\text{SNR} = \frac{P_{\text{tot}} T \left(|\alpha_{su}|^2 L + \sum_{r=1}^{R} |\alpha_{sru,r}|^2 \left\| \mathbf{g}_{\text{RIS},r} \right\|_2^2 \right)}{\sigma^2}. \tag{5.3}$$

When MP is present, the received signal contains not only thermal noise but also residual MP interference. Therefore, an effective SNR is further defined by replacing the thermal noise power with an equivalent noise power. This equivalent noise power includes both the thermal noise power and the average MP power. The effective SNR is defined as

$$\text{SNR}_{\text{eff}} = \frac{P_{\text{tot}} T \left(|\alpha_{su}|^2 L + \sum_{r=1}^{R} |\alpha_{sru,r}|^2 \left\| \mathbf{g}_{\text{RIS},r} \right\|_2^2 \right)}{\sigma_{\text{eff}}^2}. \tag{5.4}$$

5.1.3 Multipath Configuration

In this case, the LoS MP path contains $M_0 = 4$ scatter paths, while the RIS MP branches each contain $M_1 = M_2 = 3$ scatter paths. The RCS of the scatterer path is set to $c_{\text{RCS}} = 0.5$. Two scatter clusters centers are located at $[2, 2, 12]^T$ m and $[-2, 2, 12]^T$ m, respectively. Each cluster has a radius of $R_c = 1$ m. The SPs are randomly generated within the local x–z plane of the corresponding cluster, while the same geometry seed is used for all SNR points to ensure reproducibility. Therefore, the transmit-power sweep only changes the received signal strength and does not change the scatterer geometry. When MP is considered, its received power is also included in the effective noise variance used for the effective CRB and SNR. Specifically, the effective noise variance is obtained by adding the average received MP power over all subcarriers and OFDM symbols to the thermal noise variance.

$$\sigma_{\text{eff}}^2 = \sigma^2 + P_{\text{MP,avg}}, \tag{5.5}$$

5.1.4 Monte Carlo Procedure and Random Seeds

For each SNR point, the estimator is evaluated over $N_{\text{MC}} = 100$ Monte Carlo trials. In each trial, the geometry, satellite state, RIS positions, RIS configurations, pilot, and deterministic channel parameters are kept fixed, so that the Monte Carlo results reflect the effect of independent noise realizations under the same propagation and system settings. To ensure reproducibility, fixed random seeds are used in the simulation. Four fixed random seeds are used to ensure the reproducibility of different random processes in the simulation. Specifically, one seed is used for generating the directed RIS beamforming profiles $\omega_{r,l}$, one seed is used for generating the MP scatterer geometry R_{random}, one seed is used for generating the MP phasesα_m, and one seed is used before the Monte Carlo estimation loop to reproduce the additive white Gaussian noise (AWGN) realizations and random grid initializations.

5.1.5 Iterative Parameter

The delay, Doppler, and angular parameters are first initialized by coarse search and then refined by iterative MLE search. The initial grid size is set to $N_{\text{g}} = 10$. The number of local refinement layer is set to $N_{\text{iter}} = 10$.
In LoS 2D-MLE and RIS 1D-MLE, delay search half-range is set to $\tau_{\max} = 5/c$ s, corresponding to a range uncertainty of ± 5 m. The initial delay-grid resolution is therefore approximately 1 m in range.

$$\Delta\tau = \frac{2\tau_{\max}}{N_{\text{g}}} = \frac{1}{c} \text{ s}, \tag{5.6}$$

In LoS 2D-MLE, the Doppler search half-range is set to $\nu_{\max} = (25/3.6)/c$, corresponding to a velocity uncertainty of ± 25 km/h. The initial Doppler-grid resolution is approximately 5 km/h in velocity resolution.

$$\Delta\nu = \frac{2\nu_{\max}}{N_{\text{g}}} = \frac{5/3.6}{c} \text{ m/s}, \tag{5.7}$$

In RIS 2D-MLE, the angular search half-range is set to $\theta_{\max} = 45°$, giving an initial angular-grid resolution of

$$\Delta\theta = \frac{2\theta_{\max}}{N_{\text{g}}} = 9°. \tag{5.8}$$

At refinement layer h, the local search interval is scaled by 2^{-h} around the estimate obtained from the previous layer. The LoS delay and Doppler parameters are first initialized using zero-padded FFT searches with an FFT size of $N_K = N_L = 2^{13}$, and the RIS delay parameter is also estimated by 1D-FFT search with size of $N_L = 2^{13}$. The distance refinement function in the TP method are solved using MATLAB `fminunc`, whose optimality tolerance is set to $\epsilon_{\text{opt}} = 10^{-10}$.

5.2 Experiment Evaluation Metrics

5.2.1 Cramér–Rao Bound Analysis

Let $y_{k,l}$ denote the noise-free received signal at the kth subcarrier and the lth OFDM symbol. According to the implemented signal model, $y_{k,l}$ is given by

$$y_{k,l} = x_{k,l} \left(\alpha_0 B_{0,k,l} C_{0,l} + \sum_{r=1}^{R} \alpha_r B_{r,k,l} C_{r,l} G_{RIS,r,l} \right), \tag{5.9}$$

The channel parameter vector is defined as

$$\begin{aligned}\boldsymbol{\eta} = \Big[&\Re\{\alpha_0\}, \Im\{\alpha_0\}, \dots, \Re\{\alpha_R\}, \Im\{\alpha_R\}, \, \tau_0, \dots, \tau_R, \, \nu_0, \dots, \nu_R, \\ &\theta^{el}_{ru,1}, \theta^{az}_{ru,1}, \dots, \theta^{el}_{ru,R}, \theta^{az}_{ru,R} \Big]^\top.\end{aligned} \tag{5.10}$$

Assuming circularly symmetric complex Gaussian noise with variance σ^2, the FIM of $\boldsymbol{\eta}$ is

$$[\mathbf{I}_\eta]_{a,b} = \frac{2}{\sigma^2} \Re \left\{ \sum_{k=0}^{K-1} \sum_{l=0}^{L-1} \left(\frac{\partial y_{k,l}}{\partial \eta_a} \right)^* \frac{\partial y_{k,l}}{\partial \eta_b} \right\}. \tag{5.11}$$

The CRB of the channel parameters is then obtained as

$$\mathbf{C}_\eta = \mathbf{I}_\eta^{-1}. \tag{5.12}$$

When MP is present, the MP components are not explicitly included as nuisance parameters in this FIM. Instead, their average received power is incorporated into an effective noise variance. Therefore, the effective FIM $\mathbf{I}_\eta^{\text{eff}}$ under MP is computed by replacing σ^2 with σ^2_{eff}:

$$[\mathbf{I}_\eta^{\text{eff}}]_{a,b} = \frac{2}{\sigma^2_{\text{eff}}} \Re \left\{ \sum_{k=0}^{K-1} \sum_{l=0}^{L-1} \left(\frac{\partial y_{k,l}}{\partial \eta_a} \right)^* \frac{\partial y_{k,l}}{\partial \eta_b} \right\}, \tag{5.13}$$

The effective CRB of the channel parameters is obtained as

$$\mathbf{C}_\eta^{\text{eff}} = \left(\mathbf{I}_\eta^{\text{eff}} \right)^{-1}. \tag{5.14}$$

The delay, Doppler, and angular error bounds are extracted from the diagonal entries of $\mathbf{C}_\eta$ or $\mathbf{C}_\eta^{\text{eff}}$. To obtain the positioning CRB, we define the state vector

$$\mathbf{s} = [\Re\{\alpha_0\}, \Im\{\alpha_0\}, \dots, \Re\{\alpha_R\}, \Im\{\alpha_R\}, \mathbf{p}^T, \delta, \delta_f]^T, \tag{5.15}$$

The dependence of the channel parameters on the positioning-related state variables is characterized by the state-to-channel Jacobian matrix

$$\mathbf{J} = \frac{\partial \boldsymbol{\eta}}{\partial \mathbf{s}}. \tag{5.16}$$

The FIM of the state vector is obtained by the chain rule as

$$\mathbf{I}_s = \mathbf{J}^T \mathbf{I}_\eta \mathbf{J}. \tag{5.17}$$

The position error bound, the clock-bias and CFO error bounds are given by

$$\mathrm{PEB} = \sqrt{\mathrm{tr}\left([\mathbf{I}_s^{-1}]_{\mathbf{p},\mathbf{p}}\right)} \quad \mathrm{CEB} = \sqrt{[\mathbf{I}_s^{-1}]_{\delta,\delta}} \quad \mathrm{FEB} = \sqrt{[\mathbf{I}_s^{-1}]_{\delta_f,\delta_f}}. \tag{5.18}$$

When MP is present, the effective channel-domain FIM $\mathbf{I}_\eta^{\mathrm{eff}}$ is constructed by replacing the thermal noise variance σ^2 with the effective noise variance σ_{eff}^2. Using the same state-to-channel Jacobian matrix, the effective FIM of the state vector is obtained as

$$\mathbf{I}_s^{\mathrm{eff}} = \mathbf{J}^T \mathbf{I}_\eta^{\mathrm{eff}} \mathbf{J}. \tag{5.19}$$

Here, $\mathbf{I}_s^{\mathrm{eff}}$ represents the approximate state-domain FIM under MP propagation, where the residual MP interference is treated as part of the equivalent noise power. The effective position error bound, clock-bias error bound, and CFO error bound are given by

$$\mathrm{PEB}_{\mathrm{eff}} = \sqrt{\mathrm{tr}\left(\left[(\mathbf{I}_s^{\mathrm{eff}})^{-1}\right]_{\mathbf{p},\mathbf{p}}\right)} \quad \mathrm{CEB}_{\mathrm{eff}} = \sqrt{\left[(\mathbf{I}_s^{\mathrm{eff}})^{-1}\right]_{\delta,\delta}} \quad \mathrm{FEB}_{\mathrm{eff}} = \sqrt{\left[(\mathbf{I}_s^{\mathrm{eff}})^{-1}\right]_{\delta_f,\delta_f}} \tag{5.20}$$

The detailed derivatives used to construct the state-to-channel Jacobian and the numerical CRB implementation are provided in Appendix A.2.

5.2.2 RMSE and Error Metrics

To evaluate the positioning performance, this work reports not only the final UE position error but also the estimation errors of the intermediate channel parameters that directly affect localization. In this work, the term “Error” refers to an RMSE-based evaluation metric, which is used as a unified indicator to quantify the accuracy of the estimated positioning-related parameters and to show their impact on the final positioning performance. For a generic scalar parameter η, the standard RMSE over N_{MC} Monte Carlo trials is defined as

$$\mathrm{RMSE}_\eta = \sqrt{\frac{1}{N_{\mathrm{MC}}} \sum_{i=1}^{N_{\mathrm{MC}}} \left(\hat{\eta}^{(i)} - \eta\right)^2}. \tag{5.21}$$

Based on the standard definition, all the reported error metrics in the following are computed from RMSE, but are expressed in the physical units that are most relevant to positioning performance.

For delay-related parameters including time-bias, the error is converted into meters by multiplying the delay error by the speed of light c to reflect the distance deviation for directly reflects the influence of delay estimation error on the range-domain positioning accuracy. Therefore, the delay-domain error is defined as

$$\mathrm{Error}_\tau = \sqrt{\frac{1}{N_{\mathrm{MC}}} \sum_{i=1}^{N_{\mathrm{MC}}} \left[c\left(\hat{\tau}^{(i)} - \tau\right)\right]^2}. \tag{5.22}$$

For Doppler-related parameters including CFO, the normalized Doppler error is converted into an equivalent velocity error by multiplying it by c. The Doppler error is therefore reported in m/s and is defined as

$$\text{Error}_\nu = \sqrt{\frac{1}{N_{\text{MC}}}\sum_{i=1}^{N_{\text{MC}}}\left[c\left(\hat{\nu}^{(i)}-\nu\right)\right]^2}. \tag{5.23}$$

For the RIS AoD parameters, the error is reported in degrees. For an AoD parameter θ, the error is computed as

$$\text{Error}_\theta = \sqrt{\frac{1}{N_{\text{MC}}}\sum_{i=1}^{N_{\text{MC}}}\left(\hat{\theta}^{(i)}-\theta\right)^2}. \tag{5.24}$$

For the final UE position estimate, the position error is defined as the three-dimensional position RMSE, which is used as the main indicator of the final positioning performance.:

$$\text{Error}_{\mathbf{p}} = \sqrt{\frac{1}{N_{\text{MC}}}\sum_{i=1}^{N_{\text{MC}}}\left\|\hat{\mathbf{p}}^{(i)}-\mathbf{p}\right\|^2}. \tag{5.25}$$

5.3 Results and Discussion

In this work, multiple RISs are considered to evaluate the proposed algorithm and to compare its performance with different single-RIS configurations. Specifically, RIS1 and RIS2 are placed in a symmetric geometry, whereas RIS1 and RIS3 form an asymmetric geometry. For the single-RIS setup, RIS1, RIS2, and RIS3 are evaluated separately, and the TP method is used to estimate the final UE position. For the double-RIS setup, the pair composed of RIS1 and RIS2 is used to evaluate the performance under a symmetric deployment, while the pair composed of RIS1 and RIS3 is used to evaluate the performance under an asymmetric deployment. In the double-RIS setup, the joint positioning method is adopted by default, while the ablation study further compares the performance differences among three positioning methods. The main RMSE-based error metrics include the delay error, Doppler error, angle of departure horizontal (AoD-H) error, angle of departure vertical (AoD-V) error, 3D position error, time-bias error, and CFO error.

5.3.1 Double-RIS Versus Single-RIS under Symmetric Deployment

The comparative results between the single-RIS and double-RIS setups under the symmetric deployment are shown in Fig. 5.1. In this work, RIS1 $[4, 0, 10]^T$ and RIS2 $[-4, 0, 10]^T$ are symmetrically deployed with respect to the UE$[0, 10, 1.5]^T$. The single-RIS setups evaluate RIS1 and RIS2 separately, whereas the double-RIS setup jointly exploits both RISs. In the Fig. 5.1, the red, blue curves denote RIS1-only, RIS2-only in the single-RIS setup. In the double-RIS setup, yellow and green curves represent the RIS-1 and RIS-2 performance. Due to the symmetric positions of these two RISs have similar performance curves. To better interpret the results, the SNR range is roughly divided into three regions: low SNR with SNR ≤ 40 dB, medium SNR with $40 <$ SNR ≤ 60 dB, and high SNR with SNR > 60 dB.

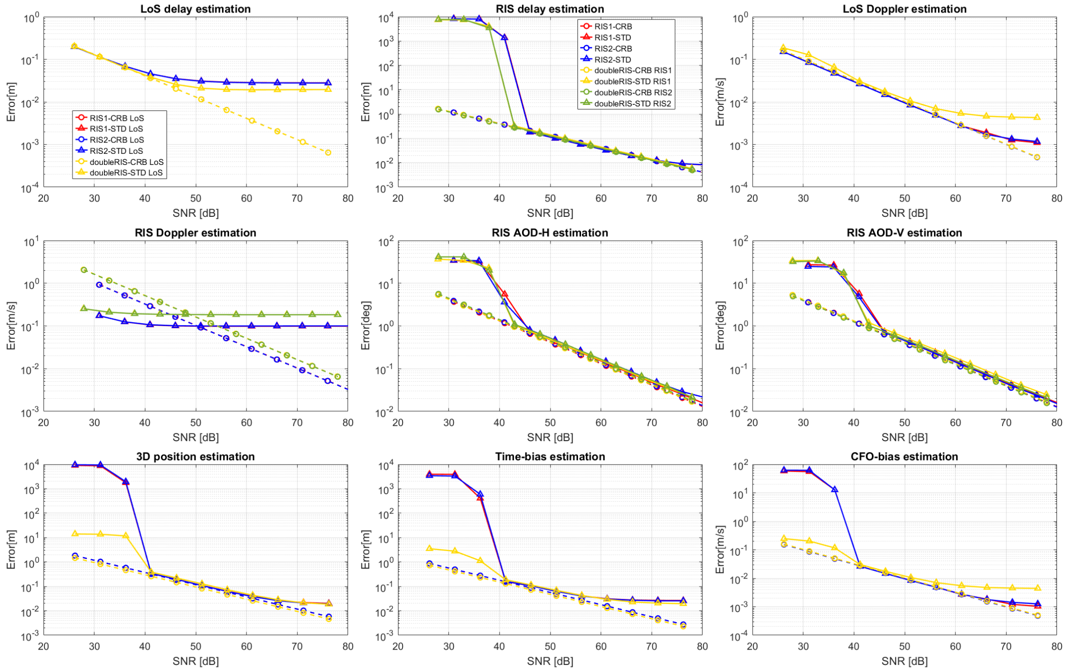

Figure 5.1: Performance comparison between RIS1 (red), RIS2 (blue), and doubleRIS setups (yellow for RIS1 and green for RIS2) and their CRBs.

5.3.1.1 Low-SNR Region

In the low-SNR region, the double-RIS setup provides the most significant robustness improvement in the final positioning-related metrics, including the 3D position error, time-bias error, and CFO error, whose curves have similar curve shape. The single-RIS setups suffer from severe threshold effects: the 3D position error can reach 10^3–10^4 m level, whereas the double-RIS setup keeps the position error much lower around the 10 m level. Similarly, the time-bias error is reduced from the 10^3–10^4 m level to approximately the 10^{-1} level, and the CFO error is reduced from the 10^1–10^2 m/s level to around 10^{-1} m/s for double-RIS setup. The reason for this improvement can be observed from the RIS delay and RIS AoD subplots. At low SNR, the RIS paths are weak and sensitive to the noise, therefore the RIS delay or angular parameters can't be reliably estimated. The RIS delay error can reach 10^3–10^4 m, and the AoD-H and AoD-V errors also remain at tens of degrees. The single-RIS setup mainly relies on the delay estimation, whose positioning accuracy is severely affected by the large RIS delay error. In contrast, the double-RIS setup benefits from the additional geometric constraint provided by the bearing-line methods, less dependent on unreliable RIS delay estimation values. What's more, the LoS delay and LoS Doppler errors are relatively similar among the three methods in this region, roughly around 10^{-1} m and 10^{-1} m/s, respectively, which indicates double-RIS setup mainly comes from improved geometric robustness rather than a large improvement in the LoS parameter estimation.

5.3.1.2 Medium-SNR Region

The medium-SNR region corresponds to the transition region. In this positioning-related curves,the single-RIS setups start to recover from the threshold effect and gradually approach the double-RIS performance as well as the theoretical CRB curve, which means satisfying performance for both RIS setups. The single-RIS 3D position and time-bias errors decrease rapidly from the 10^3–10^4 m level to the sub-meter level, while the CFO error decreases toward approximately 10^{-2} m/s. The double-RIS setup also improves in this region, but its curve is smoother because it has already maintained a much lower error in the low-SNR region. This improvement is mainly attributed to the enhanced RIS delay and angular estimation accuracy. The RIS delay and AoD errors decrease sharply around 40–50 dB. Specifically, the RIS delay error drops from the 10^3–10^4 m level to the sub-meter level, while the AoD-H and AoD-V errors decrease from several tens of degrees to around 1 degree and further approach 10^{-1} degrees as the SNR increases. For the LoS delay, all methods continue to improve and approach the the platform 10^{-2} m level due to stronger signal interference. The double-RIS curve remains slightly lower error in LoS and earlier down-trend in RIS delay, suggesting that time-orthogonal RIS coding and more reliable LoS subtraction help reduce residual interference. For LoS Doppler and CFO, both setups approach the theoretical curves to prove the effectiveness of the RIS estimation algorithm. For the RIS Doppler estimation, the empirical standard deviation (STD) may appear to break the theoretical CRB. This is because the RIS-path Doppler is not independently estimated in the simulation; instead, it is approximated by the estimated LoS Doppler, $\hat{\nu}_{sru,r} = \hat{\nu}_{su}$, which is a biased estimator for the RIS Doppler, while the theoretical CRB denotes the unbiased estimator.

5.3.1.3 High-SNR Region

In the high-SNR region, both methods reach their error-floor levels due to residual signal interference, and the gap between the single-RIS and double-RIS setups becomes smaller. The 3D position error is generally on 10^{-2}–10^{-1} m, the time-bias error is below 10^{-1} m, and the CFO error is around 10^{-3}–10^{-2} m/s. Therefore, once the RIS paths are reliably estimated, the single-RIS methods can also achieve accurate localization. It is worth noting that the double-RIS setup remains competitive and achieves lower error-floor levels in delay and angular estimation, which can be attributed to the time-orthogonal coding, despite the reduced per-RIS branch power. A degradation is mainly observed in the LoS Doppler metrics. This is because the reduced per-RIS branch power in the time-orthogonal coding makes the LoS Doppler estimation more sensitive to residual phase errors. Compared with the single-RIS setup, the symmetric double-RIS setup significantly improves positioning robustness in the low-SNR region and provides competitive or slightly improved performance in the medium- and high-SNR regions.

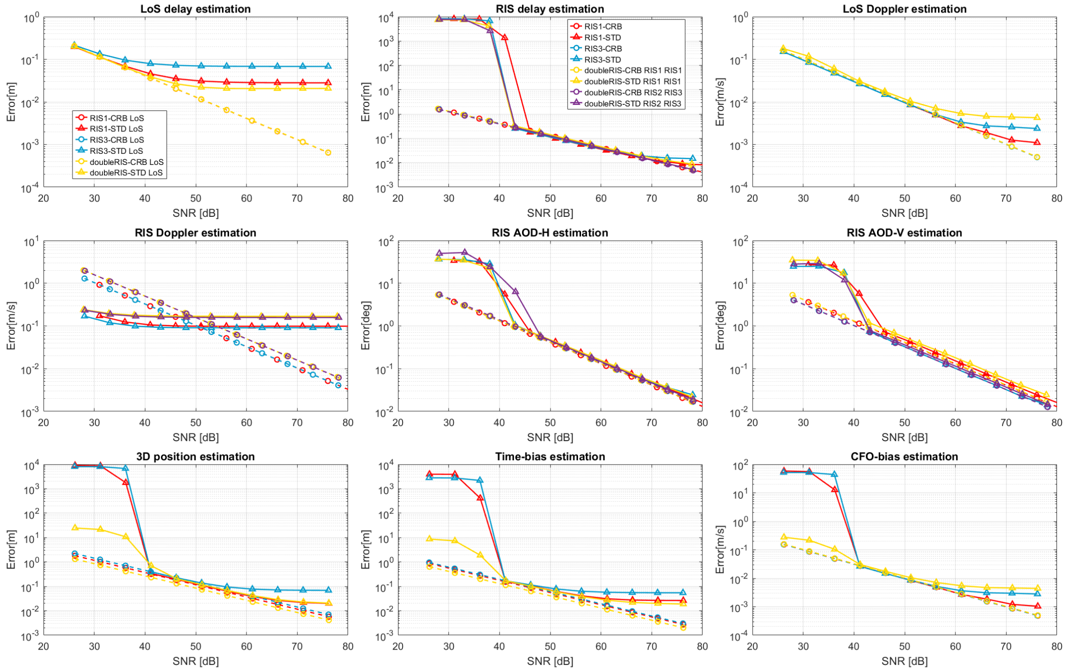

Figure 5.2: Performance comparison between RIS1 (red), RIS3 (Cyan), and doubleRIS asymmetric setup (yellow for RIS1 and purple for RIS3) and their CRBs.

5.3.2 Double-RIS Versus Single-RIS under Asymmetric Deployment

To further study the effectiveness of double-RIS setup, the comparative results between the single-RIS and double-RIS setups under the asymmetric deployment are shown in Fig. 5.2. In this work, RIS1 $[4, 0, 10]^T$ and RIS3 $[-6, 0, 8]^T$ form an asymmetric deployment with respect to the UE $[0, 10, 1.5]^T$. The single-RIS setups evaluate RIS1 and RIS3 separately, whereas the double-RIS setup jointly exploits both RISs. In Fig. 5.2, the red, cyan curves denote RIS1-only, RIS3-only in the single-RIS setup. In the double-RIS setup, yellow and purple curves represent the RIS1 and RIS3 performance. Due to the symmetric positions of these two RISs have similar performance curves. Compared with the symmetric double-RIS deployment in Fig. 5.1, the asymmetric double-RIS deployment shows a similar overall performance trend. In both cases, the double-RIS setup significantly improves robustness in the low-SNR region and maintains competitive accuracy in the medium/high-SNR region. This indicates that the proposed double-RIS framework does not rely strictly on a symmetric RIS layout.

5.3.2.1 Comparison with the Symmetric Deployment

The main similarity between the symmetric and asymmetric deployments is observed in the final positioning-related metrics. In the low-SNR region, the single-RIS setups still suffer from severe threshold effects, whereas the double-RIS setup keeps the 3D position error, time-bias error, and CFO error at a much lower level. More specifically, the 3D position error is reduced from approximately 10^3–10^4 m for the single-RIS baselines to around 10 m for the double-RIS setup. The time-bias error is also reduced from the 10^3–10^4 m level to approximately the meter level, while the CFO error decreases from the 10^1–10^2 m/s level to around 10^{-1} m/s. This behavior is consistent with the symmetric case and confirms that the performance improvement achieved by the double-RIS setup is more generally applicable, rather than being merely a result of a particular placement configuration. In the medium-SNR region, the asymmetric deployment also shows a transition behavior similar to the symmetric deployment. Both the single-RIS and asymmetric double-RIS setups approach the theoretical bounds similarly to the symmetric double-RIS setup, which demonstrates satisfactory positioning performance in the medium-SNR region. As the RIS paths become detectable around 40–60 dB, the RIS delay and angular estimation errors decrease rapidly. The RIS delay error drops from the 10^3–10^4 m level to the 10^{-2}–10^{-1} level, while the AoD-H and AoD-V errors decrease from several tens of degrees to around the 10^{-1} degree level. Therefore, both symmetric and asymmetric deployments demonstrate that the proposed method can provide stable performance over the threshold transition region. In the high-SNR region, the asymmetric double-RIS setup also achieves a performance level close to that of the symmetric double-RIS setup and even shows slightly improved performance, in terms of 3D position error and time-bias error, due to the increased diversity of geometric information. The 3D position error reaches the error-floor around 10^{-2}–10^{-1} m, the time-bias error is below 10^{-1} m, and the CFO error is around 10^{-3}–10^{-2} m/s. For the channel-parameter estimates, the LoS delay and RIS delay errors are generally around the 10^{-2} m level, while the AoD-H and AoD-V errors are around 10^{-2}–10^{-1} degrees. These values are comparable to those obtained under the symmetric double-RIS deployment, suggesting that the performance improvement is not strongly dependent on a specific placement configuration.

5.3.2.2 Differences Caused by the Asymmetric Geometry

Although the overall performance of the double-RIS setup remains similar to the symmetric case, the asymmetric deployment results in some noticeable differences because of the asymmetric positioning. In the symmetric deployment, the RIS1-only and RIS2-only curves are close to each other because the two RISs have similar geometric relationships with the UE. In contrast, under the asymmetric deployment, the RIS1-only and RIS3-only results differ due to the asymmetric geometry. This difference is especially visible in the LoS delay results in the medium- and high-SNR regions, where the RIS3 case reaches a higher error floor earlier than the RIS1 case. This is mainly attributed to the less favorable geometry of RIS3, which makes the LoS path separation more sensitive to residual interference and estimation errors. The asymmetric geometry also affects the Doppler-related metrics. In the LoS Doppler subplots, the RIS3 reaches a higher error-floor $10^{-3} - 10^{-2} m/s$ than RIS1 $10^{-3} m/s$, which can also be explained by the less favorable geometry of RIS3. Nevertheless, these differences do not change the main conclusion. The asymmetric double-RIS setup still achieves performance close to the symmetric double-RIS setup especially in the final localization metrics despite the presence of the less favorable geometric positions. Therefore, the asymmetric experiment verifies that the proposed method is not limited to an ideal symmetric deployment and can maintain

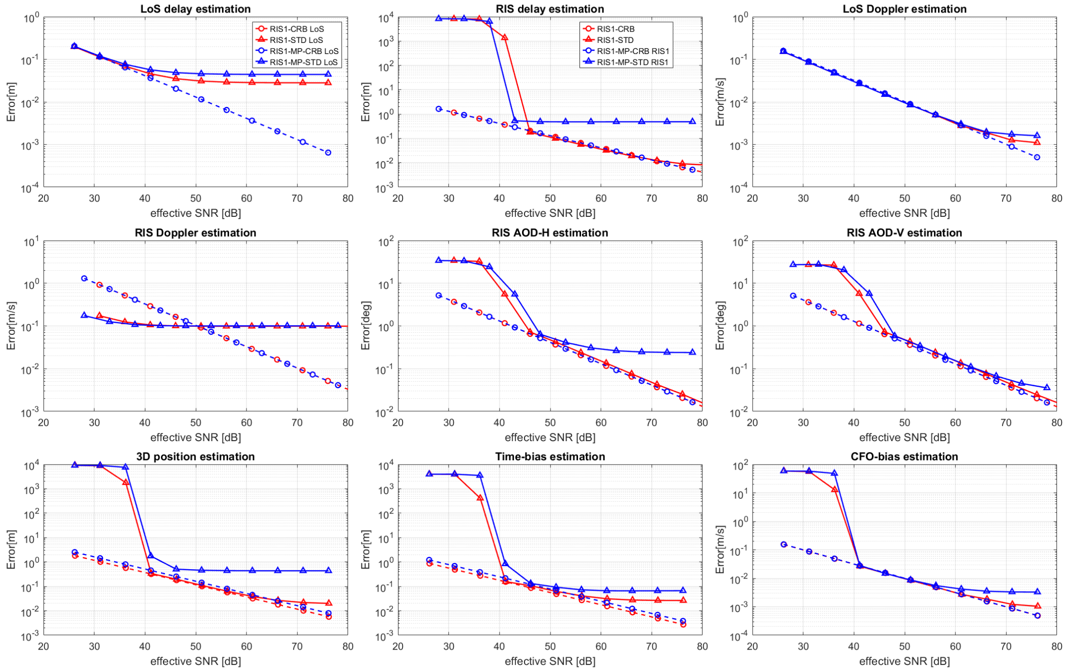

Figure 5.3: Estimation performance of the single-RIS setup without multipath (red) and with multipath (blue).

reliable performance under more general RIS geometries.

5.3.3 The Effect of Multipath

5.3.3.1 Multipath versus No-Multipath

This subsection evaluates the influence of the MP effect on the proposed localization framework. Fig. 5.3 first compares the single-RIS setup without and with MP, where the red curve denotes RIS1 without MP and the blue curve denotes RIS1 with MP. In general, it can be observed that MP mainly introduces severe error floors and threshold effects in the estimation results. For the LoS delay estimation, the no-MP case achieves a lower high-SNR error floor in medium-/high- SNR region. This suggests that LoS-related MP components bias the direct LoS delay estimate due to their similar delay–Doppler structure and non-negligible power. The degradation is more pronounced for the RIS delay error, where the RIS1 delay error without MP can approach the theoretical bound in the medium-/high- SNR region around 10^{-2} m. However, the the MP case reaches the higher error-floor around the m level since the medium-SNR. On the other hand, the RIS2 approaches the theoretical bound in medium-/high- SNR region because the RIS2 branches is approximately orthogonal to the LoS and RIS1 components, which leads to accurate delay estimation for RIS2. In comparison, the Doppler-related metrics are less affected, although small high-SNR error floors are still observed. These estimation errors further degrade the final localization performance. In 3D position error, the RIS1 without MP can approach the theoretical bound in medium/high SNR region while the performance is limited to higher error floor m level due to the MP. The time-bias error and the CFO error

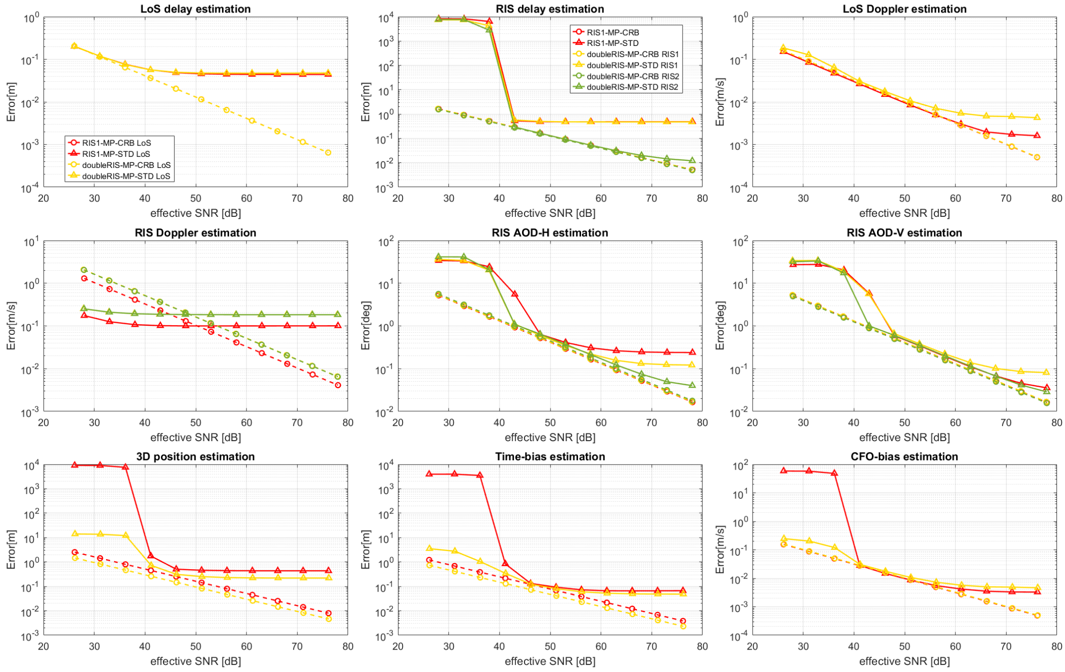

Figure 5.4: Estimation performance of the single-RIS setup (red) and double-RIS setup (yellow for RIS1 and green for RIS2) under multipath.

reach higher error-floor under MP. Overall, MP acts as structured interference and introduces residual estimation bias even when the thermal noise level is low.
Fig. 5.4 compares the single-RIS and double-RIS setups under MP, where the red, yellow and green curves denote the RIS1 , RIS1 in the double-RIS and RIS2 in the double-RIS under the MP with the RCS value is 0.5. Although MP degrades the estimation performance in the single-RIS setup, the double-RIS setup still achieves performance comparable to the no-MP case in the low-SNR region. The double-RIS setup reduces the 3D position error from 10^4 m to 10^1 m level, reduces the time-bias error from 10^3 m to the 10^0 m level, and lowers the CFO error from the 10^1 m/s level to the 10^{-1} m/s level. In the medium-/high-SNR region, both LoS and RIS delay meet the bottleneck under the MP, which means that the MP component with similar delay–Doppler structure degrades the delay estimation severely. The LoS delay reaches error-floor around the 10^{-1} m level and RIS delay reaches error-floor around the m level. Despite these limitations, the double-RIS method still provides slight improvements in the 3D position and time-bias estimation errors. Overall, MP introduces structured interference and high-SNR error floors, but the proposed double-RIS method still achieve reliable localization accuracy especailly in low-SNR region.

5.3.3.2 Impact of the Multipath Coefficient

This subsection investigates the influence of the MP coefficient c_{RCS} on the symmetric double-RIS setup. Two cases are compared in Fig. 5.5, namely $c_{\mathrm{RCS}} = 0.5$ and $c_{\mathrm{RCS}} = 2$, where the latter represents stronger MP interference. Increasing c_{RCS} mainly introduces higher residual error floors. For the LoS delay estimation, the

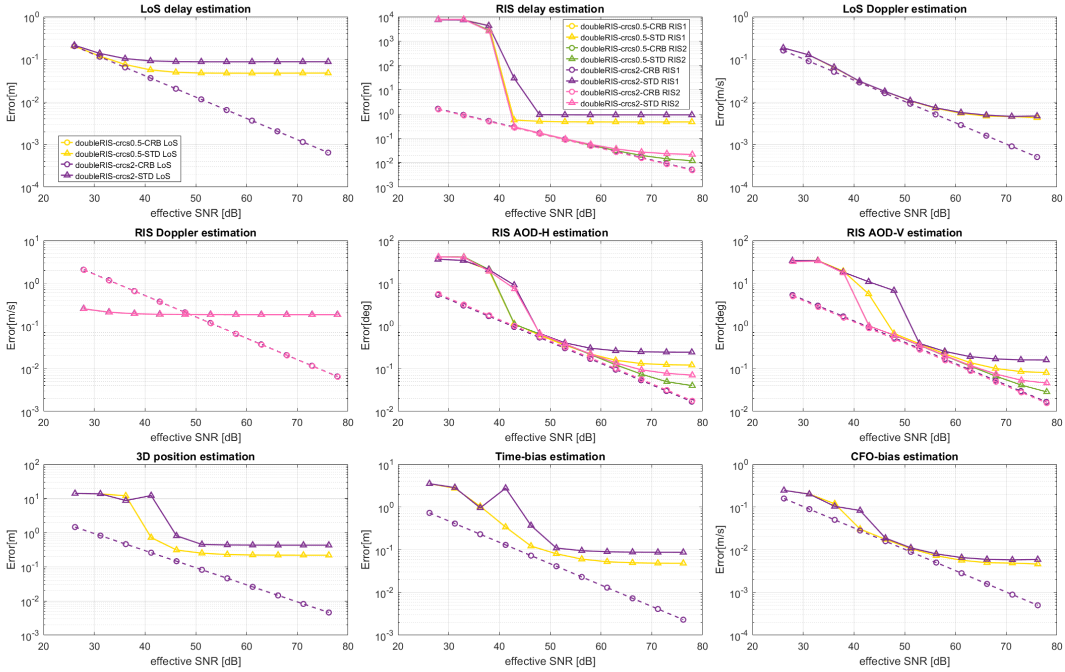

Figure 5.5: Estimation performance of different multipath coefficient in symmetry double-RIS setup crcs=0.5(yellow is RIS1 and green is for RIS2) and crcs=2(purple for RIS1 and pink for RIS2).

medium-/high-SNR error floor increases from the 10^{-2} m level to the 10^{-1} m level when c_{RCS} increases from 0.5 to 2. This indicates that stronger MP components degrade the direct LoS delay estimate due to their similar delay–Doppler structure. The similar trend appears in the in the RIS delay estimation, the RIS1 in $cRcs = 2$ reaches higher error-floor m level than $cRcs = 0.5$. RIS2 dealy curves in both experiments approach theoretical bounds benefited from the time-orthogonal coding scheme. The LoS and RIS Doppler estimations are less sensitive to the increasing MP coefficient. This is because both Doppler estimates are mainly determined by the LoS Doppler estimation, which is less affected by MP after delay-domain reconstruction and subtraction. The LoS Doppler estimation is less sensitive, decreasing from the 10^{-1} m/s level at low SNR to the 10^{-3} m/s level at high SNR, although the stronger MP case still shows a slightly higher floor. In terms of positioning accuracy, the increasing MP curves achieves similar performance in low-SNR region and higher error-floor in medium-/high- SNR region. For both MP coefficients, the double-RIS geometry keeps the 3D position error at the 10^{1} m level and time-bias error at m level in the low-SNR region. In the medium- and high-SNR regions, the curve with a larger MP coefficient generally performs worse than the case with $c_{\text{RCS}} = 0.5$. However, around 40 dB, the $c_{\text{RCS}} = 2$ curve shows a temporary higher error in the 3D position and time-bias errors, which is mainly attributed to the SNR-based threshold rule. Overall, increasing c_{RCS} from 0.5 to 2 strengthens the MP interference and mainly causes higher high-SNR error floors in the channel and position estimates. Nevertheless, the proposed double-RIS method still maintains satisfactory performance, particularly in the low-SNR region, due to the robustness

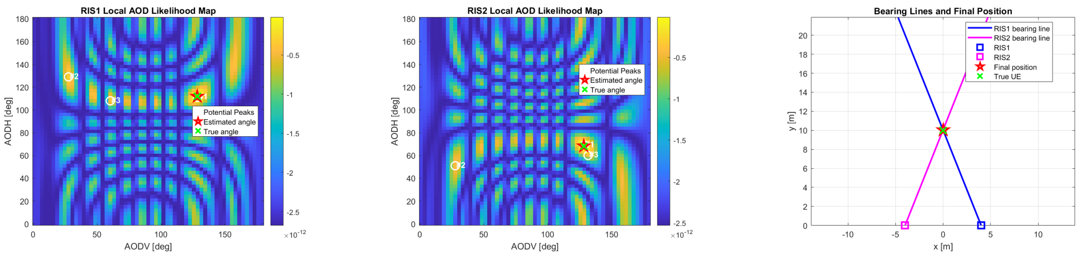

Figure 5.6: Double-RIS Setup AoD heatmap and its bearing-line map(60dB).

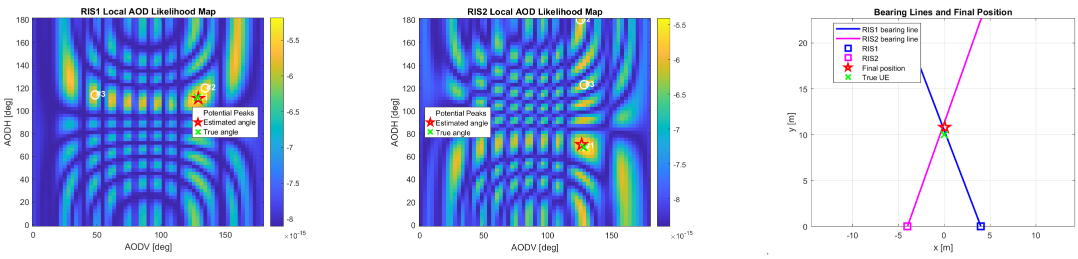

Figure 5.7: Double-RIS Setup AoD heatmap and its bearing-line map(40dB).

provided by the proposed framework.

5.3.4 Ablation Study

This section provides deeper insight into the proposed method from three perspectives: RIS AoD algorithm likelihood heatmaps, bearing-line visualization, comparison of different positioning methods, and the effect of RIS time-orthogonal coding.

5.3.4.1 RIS AoD Heatmap Comparison

Fig. 5.6 and Fig. 5.7 demonstrate two RIS likelihood heatmap and bearing-line map in the double-RIS setup under two SNR threshold (40dB and 60dB) to reflect different SNR region. The AoD likelihood heatmaps visualize the 2D-MLE search for the RIS angular parameters. The horizontal and vertical axes denote AoD-V and AoD-H, respectively. The red star denotes the estimated AoD, the green cross denotes the true value, and the white circles indicate possible peaks. The color intensity indicates the likelihood value, with brighter yellow regions corresponding to stronger candidate peaks. The bearing-line map illustrates the positioning result in the x-y plane. The two RISs, represented by blue and pink square, are located at $[-4, 0, 10]$ and $[4, 0, 10]$, and their bearing lines are constructed from the estimated AoD values. The red star represents the estimated UE position, while the green cross represents the true position. As shown in Fig. 5.6, in SNR (60 dB) the estimated AoD values of both RIS1 and RIS2 are close to the true values, which demonstrates that the proposed AoD 2D-MLE search algorithm is capable of accurately extracting the AoD information in high-SNR region. The corresponding bearing lines intersect near the true UE position, confirming that the double-RIS bearing-line method provides

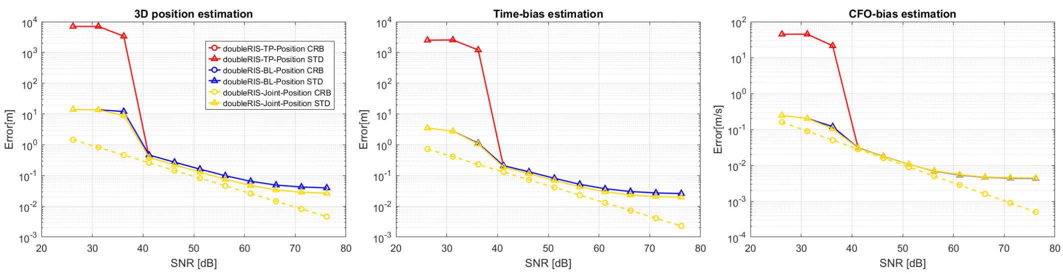

Figure 5.8: Double-RIS Setup three positioning methods comparison for delay-difference only (red), bearing-line only (blue) and joint positioning(yellow).

effective geometric constraints for localization. As shown in Fig. 5.7, in SNR (40 dB), the estimated AoD values show slight deviations from the true values and additional candidate peaks become more prominent, which may disturb the estimation process. This observation explains the increased angular estimation error observed in the low-SNR region. Nevertheless, the estimated AoD values remain close to the true values, and the bearing-line intersection is still near the true UE position.

5.3.4.2 Positioning Method Comparison

To verify the effectiveness of the proposed double-RIS joint positioning method, this section compares three positioning strategies underthe same double-RIS channel-parameter estimates: the delay-difference method, the bearing-line method, and the proposed joint positioning method. The results are shown in Fig. 5.8. Since the estimated channel parameters are identical for the three methods, the channel-parameter estimation subplots are the same as those in Fig. 5.1. Therefore, this ablation study focuses on the last three metrics, namely the 3D position error, time-bias error, and CFO error, which directly reflect the final localization performance. The curves in Fig. 5.8 are distinguished by three colors: red, blue, and yellow, representing the delay-difference method, the bearing-line method, and the proposed joint positioning method, respectively. In the low-SNR region, the TP method suffers from a severe threshold effect like the single-RIS setup, while the bearing line (BL) and joint positioning methods achieves robust localization accuracy. The latter two method drops from 10^4 m level to 10 m level in 3D position error, from 10^3 m level to 10^{-1} m level in time-bias error and from 10^1 m/s level to 10^{-1} m/s in CFO error. This improvement is mainly attributed to the geometric constraints provided by the BL method using angular information, while the TP method heavily depends on accurate RIS delay estimation. In the medium-/high- SNR region, the gap between these three methods is smaller due to increasing RIS. In medium-SNR region, 3D position error, time-bias error and CFO curves approaches the CRB curves from 10^{-1} to 10^{-2} m level,10^{-1} to 10^{-2} m level and 10^{-2} to 10^{-3} m/s level separately. In high-SNR region, all three metric curves reaches their error-floor due to the increasing signal interference. Among the three methods, the joint positioning method achieves slightly better performance than the BL method in the medium- and high-SNR regions, benefiting from the improved accuracy of the RIS delay estimation.

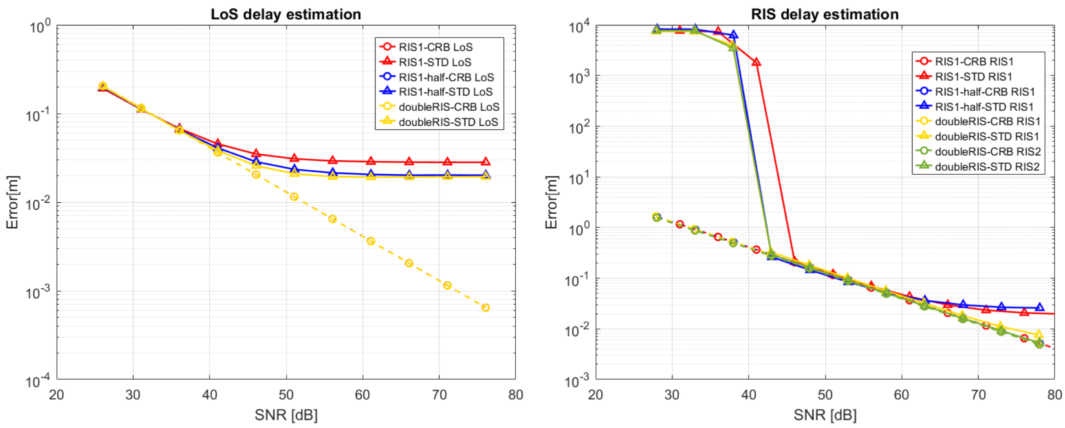

Figure 5.9: The half-power single-RIS setup comparison to Double-RIS setup.Red, blue, yellow and green curves denote RIS1, half-RIS1, double-RIS(RIS1) and double-RIS(RIS2).

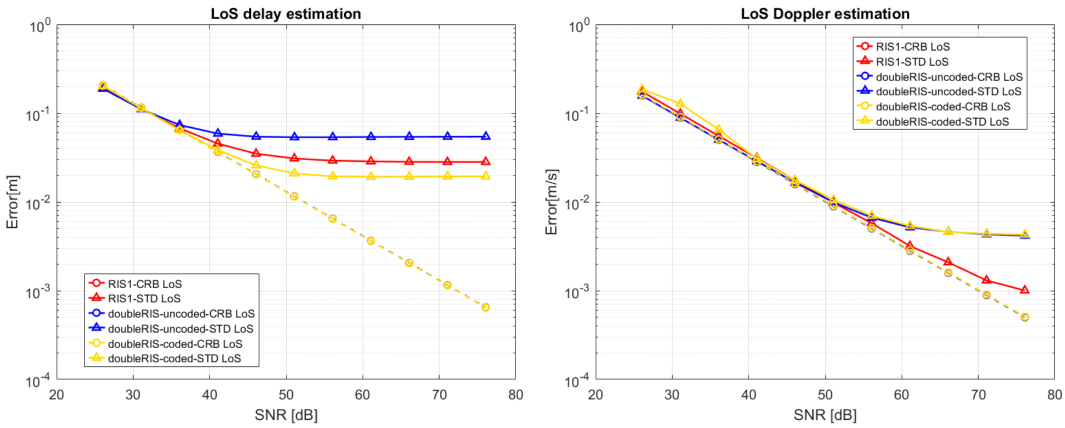

Figure 5.10: The double-RIS setup coding performance comparison for LoS delay (left) and LoS velocity (right). Red, blue, yellow curves denote RIS1, double-RIS (uncoded), double-RIS.

Based on the above experimental results, the ablation study demonstrates the complementary advantages of the two positioning methods. The TP method is sensitive to RIS delay errors at low SNR but becomes accurate at high SNR. The BL method provides better low-SNR positioning robustness but it isn't as accurate as TP method when RIS delay error improves. By combining both methods, the proposed joint positioning method achieves more robust and stable localization performance across the whole SNR range.

5.3.4.3 RIS Time-Orthogonal Coding Study

This section investigates the role of the proposed time-orthogonal RIS coding in the double-RIS setup and explains why the double-RIS configuration can achieve improved or comparable estimation performance. A half-amplitude single-RIS experiment is used as a reference, as shown in Fig. 5.9, which emulates the effective per-RIS reflected-signal strength in the time-orthogonal double-RIS configuration. From the LoS delay estimation, the coded double-RIS curve is close to the half-amplitude single-RIS curve, and both remain at the 10^{-2} m level in the high-SNR region. This indicates that the LoS delay improvement can be achieved by reducing the interference from the RIS components, where LoS path is mainly affected by the similar encoding RIS1 branch and RIS2 branch is approximately orthogonal to the LoS path. In the RIS delay estimation, the double-RIS has similar trend with the half-amplitude curve in low-SNR region and slight improvement in high-SNR region, which explains slight positioning improvement for double-RIS setup compared to single-RIS. This behavior can be interpreted from the time-orthogonal coding structure. The LoS component is not coded by the RIS coding scheme, which is regarded as similar coding pattern with RIS1 branch, therefore the RIS2 is suppressed due to the orthogonality when LoS delay is estimated. Also in the high-SNR region, each RIS branch delay is estimated more accurately due to the suppression from the orthogonality.

To further investigate whether the observed improvement is mainly caused by the reduced reflected-signal energy or by the proposed time-orthogonal coding scheme, an uncoded double-RIS experiment is conducted, as shown in Fig. 5.10. Red, blue and yellow curves denote RIS1, uncoded double-RIS and double-RIS. The uncoded double-RIS method integrates the RIS branches without time-orthogonal coding during channel estimation, which destroys the data association between the received signal and each individual RIS branch, making branch-wise RIS parameter estimation unreliable. Therefore, the following experiment focuses only on the LoS component for the uncoded double-RIS case. In LoS delay estimation, among three methods, the uncoded double-RIS setup shows a highest LoS delay error floor at the 10^{-2}–10^{-1} m level, while the coded double-RIS setup keeps the lowest error-floor at the 10^{-2} m level in medium-/high- SNR region. This demonstrates that time-orthogonal coding effectively reduces residual RIS path interference, especially when thermal noise is no longer dominant. For LoS Doppler estimation, the effect of coding is less significant. Both double-RIS methods have similar curves and have higher error-floor 10^{-3}–10^{-2} m/s level in high-SNR region. The remaining high-SNR floor is mainly caused by residual Doppler mismatch between different propagation paths rather than by inter-RIS interference alone. The ablation results confirm that the proposed time-orthogonal RIS coding is essential for the double-RIS setup. It separates the two RIS branches, reduces inter-branch interference, and prevents the additional RIS branch from degrading the LoS delay estimation.

Table 5.1: Experiment Simulation Parameters.

Parameter	**Symbol**	**Value**
UE position	$\mathbf{p}$	$[0,\ 10,\ 1.5]^T$ m
RIS1 position	$\mathbf{p}_{R,1}$	$[4,\ 0,\ 10]^T$ m
RIS2 position	$\mathbf{p}_{R,2}$	$[-4,\ 0,\ 10]^T$ m
RIS3 position	$\mathbf{p}_{R,3}$	$[-6,\ 0,\ 8]^T$ m
RIS orientation	$\mathbf{R}_r$	$\mathbf{I}_{3\times3},\ r \in \{1, 2\}$
RIS dimensions	$N_x \times N_z$	10×10
Number of RIS elements	N_r	100
Inter-element spacing	d_{RIS}	$\lambda/2$
LEO satellite orbital altitude	h	600 km
LEO satellite angles	$(\theta_{\text{sat}}^{\text{az}}, \theta_{\text{sat}}^{\text{el}})$	$(90°,\ 45°)$
Carrier frequency	f_c	2 GHz
Wavelength	λ	c/f_c
Number of subcarriers	K	2000
Number of OFDM symbols	L	256
Subcarrier spacing	Δf	15 kHz
System bandwidth	$B = K\Delta f$	30 MHz
Useful OFDM symbol duration	T	$1/\Delta f$
OFDM symbol duration	T_{sym}	$(1 + 0.07)T$
Cyclic prefix duration	T_{CP}	$7\%T$
Time bias	δ	1 ns
CFO factor	δ_f	10^{-6}
Nominal 3GPP transmission power	P_{3GPP}	54 dBm
Noise PSD	N_0	-174 dBm/Hz
Noise figure	N_f	7 dB
Time-orthogonal block number	Γ	2
Time-orthogonal block length	$\tilde{L} = L/\Gamma$	128
IFFT/FFT size	N_K, N_L	2^{13}
MLE grid size	N_g	10
MLE refinement iterations	N_{iter}	10
Monte Carlo runs	N_{MC}	100
LoS scatter paths	M_0	4
RIS1/RIS scatter paths	$M_1,\ M_2$	3
Scatter-cluster centers	$\mathbf{p}_c$	$[2,\ 2,\ 12]^T,\ [-2,\ 2,\ 12]^T$ m
Scatter-cluster radius	R_c	1 m
Scatter RCS coefficient	c_{RCS}	$0.5, 2$
MLE delay grid boundary	$\tau_{\max}$	$\pm 5/c$ s
MLE Doppler grid boundary	$\nu_{\max}$	$\pm 7/c$
MLE AoD grid boundary	$\theta_{\max}$	$\pm 45°$
Location uncertainty for beamforming	$\sqrt{\text{diag}(\mathbf{\Sigma}_p)}$	$[1,\ 1,\ 1]$ m

6 Conclusion

6.1 Conclusion

This thesis studied LEO localization for a single UE using a multi-RIS setup. The considered propagation channel includes the LoS signal, multiple RIS signals, and scatter MP signals. To separate different RIS branches, a time-orthogonal RIS profile based on time-orthogonal coding was adopted, and Doppler compensation was performed before time-orthogonal decoding to preserve the code orthogonality. To avoid high-dimensional joint estimation, a staged channel estimation procedure was developed. The LoS delay and Doppler were first estimated by exploiting the dominant LoS component. Then, the reconstructed LoS signal was subtracted from the received signal, followed by Doppler compensation and time-orthogonal decoding for estimating the RIS delays and AoDs. Finally, the proposed positioning method combines bearing-line positioning and delay-difference positioning based on the SNR-threshold rule. Based on the simulation results, the main conclusions are summarized as follows.

- The double-RIS setup significantly improves low-SNR positioning accuracy compared with the single-RIS setup. In the low-SNR region, the single-RIS methods suffer from severe error brought by RIS delay error, with 3D position errors at the 10^4 m level. In contrast, the double-RIS setup keeps the position error at the 10 m level, reduces the time-bias error from the 10^4 m level to the m level, and reduces the CFO error from the 10^2 m/s level to the 10^{-1} m/s level.
- In the medium- and high-SNR regions, the double-RIS setup maintains competitive accuracy with slight improvement. After the RIS estimation becomes reliable, the RIS delay error decreases from the 10^3–10^4 m level to the 10^{-1} m level, while the AoD errors decrease from the 10^1 degree level to the 10^{-1} degree level. At high SNR, the 3D position error reaches the 10^{-2} m level, the time-bias error remains below the 10^{-1} m level, and the CFO error reaches the 10^{-3} m/s level.
- The MP results show that MP acts as structured interference and introduces high-SNR error floors. Under MP, both single-RIS and double-RIS face the limitation of LoS and RIS delay in medium-/high- SNR region, where the LoS delay reaches at the 10^{-2}–10^{-1} m level, and the 3D position error is limited to the submeter level. Stronger MP further increases the residual error floor and worsen the positioning accuracy. Nevertheless, the double-RIS setup still keeps low-SNR robust positioning under MP, reducing the position error from

the 10^4 m level to the 10^1 m level.
- The ablation study confirms the complementary roles of delay-difference and bearing-line positioning. The delay-difference method is sensitive to unreliable RIS delay estimates at low SNR, leading to position errors at the 10^4 m level, but it becomes accurate at high SNR. The bearing-line method achieves more robust positioning accuracy at low SNR, keeping the position error at the 10^1 m level, but its high-SNR accuracy is slightly worse than delay-difference method. The proposed joint positioning method combines these advantages and provides stable and improved performance across the whole SNR range.
- The time-orthogonal RIS coding is essential for the double-RIS system to reduce the interference for LoS and RIS delay estimation. With coding, the double-RIS setup achieves a LoS delay error floor at the 10^{-2} m level, close to the half-amplitude single-RIS reference. Without coding, double-RIS method achieves even higher error-floor than single-RIS method. This confirms that the proposed coding scheme separates the two reflected branches and reduces inter-branch interference, which is essential for the double-RIS setup.

In summary, the proposed double-RIS localization framework improves positioning accuracy across all-SNR region by combining multiple-RIS, joint positioning, and time-orthogonal RIS coding. The most significant gain appears in the low-SNR region, where the proposed method reduces the 3D position error, time-bias error, and CFO error by several orders of magnitude compared with single-RIS setup. Although MP and residual Doppler mismatch introduce high-SNR error floors, the proposed method still maintains reliable and improved localization accuracy across the evaluated SNR range.

6.2 Limitations

Although the proposed double-RIS localization framework demonstrates clear performance gains, several limitations remain in the current study.
- The MP components are included in the received signal but are not explicitly modeled as unknown channel parameters in the theoretical bound. In the current CRB evaluation, their effect is approximated through an effective noise term, which cannot fully capture the structured interference and estimation bias caused by MP propagation.
- The current simulation assumes a fixed and static UE during the signal transmission period. This assumption simplifies the delay and Doppler models, but it does not fully represent mobile scenarios such as vehicles or other dynamic users.
- The current model considers a single LEO satellite. Although the proposed method exploits multiple RISs, the potential geometric diversity from multiple LEO satellites is not included.
- The joint positioning method is implemented using a relatively simple strategy that combines bearing-line and delay-difference positioning according to the received SNR. This approach verifies the complementary roles of the two positioning methods, but more advanced nonlinear optimization may further improve the final position estimate.

- The RIS response, phase profiles, and element positions are assumed to be perfectly known. In practice, imperfect RIS calibration, phase errors, element position errors, and quantized phase shifts may degrade the reflected-path parameter estimation.
- Practical satellite and receiver imperfections are not fully considered. The satellite ephemeris, satellite clock, synchronization, oscillator instability, phase noise, and other hardware impairments are assumed ideal or only partially represented, although they may affect the delay, Doppler, and CFO estimation accuracy in real systems.

6.3 Future Work

Several research directions can be developed based on the above limitations.

- Future work should explicitly include MP components in the channel estimation and theoretical analysis. Instead of treating MP as effective noise, the MP delays, Doppler shifts, angles, and complex gains can be modeled as nuisance parameters. This would allow the construction of a more complete FIM and a more accurate CRB for evaluating the proposed localization method under structured MP interference.
- The proposed framework can be extended to dynamic UE scenarios. For mobile users, the UE position and velocity should be jointly estimated, and the Doppler model should include both satellite motion and UE motion.
- Multiple LEO satellites can be introduced into the localization model. In practical NTN systems, a terrestrial UE may receive signals from several LEO satellites. Jointly exploiting multiple satellite LoS paths and multiple RIS paths can provide stronger geometric diversity and improve localization robustness.
- More advanced joint positioning optimization methods should be studied. Instead of using a simple SNR-based combination of bearing-line and delay-difference positioning, future work can formulate the final localization problem as a nonlinear problem to jointly use delay, angle, Doppler, clock-bias, and CFO information with proper uncertainty weighting.
- Practical RIS calibration errors should be incorporated. Future studies can analyze the impact of imperfect RIS phase control, element position errors, mutual coupling, finite phase resolution, and imperfect knowledge of the RIS orientation. Robust beamforming profiles and calibration-aware estimation algorithms can then be designed.
- Realistic satellite and hardware impairments should be included. Future work can consider satellite ephemeris errors, satellite clock errors, oscillator phase noise, synchronization errors, sampling-frequency offset, quantization effects, and other transceiver impairments.

6.4 Risk Considerations

This thesis is a simulation-based study and does not involve real satellite data or the collection and processing of high-accuracy locations of real users. Therefore, a detailed privacy impact assessment and practical deployment risk analysis are not included within the scope of this work. High-accuracy localization enabled by LEO satellites and RISs has societal value, including improved emergency response, autonomous navigation, industrial automation, and reliable positioning in environments where conventional GNSS signals are weak or unavailable. At the same time, such technologies are inherently dual-use. High-accuracy positioning capabilities may be misused for unauthorized tracking. Therefore, future practical systems should treat privacy protection, security, energy efficiency, and sustainable space-infrastructure management as explicit design requirements.

- From a privacy perspective, high-accuracy localization may be misused for unauthorized target tracking. Hence, practical deployment should consider access control, user consent, data minimization, and privacy-preserving data processing, especially when localization results are associated with identifiable users.
- From a security perspective, the proposed framework relies on delay, Doppler, and angle-domain measurements. As a result, it may be vulnerable to spoofing, jamming, or malicious reflected paths. Future practical systems should therefore incorporate authentication mechanisms, interference monitoring, spoofing detection, and robust estimation methods to ensure the reliability of localization results.
- From an ecological and infrastructure-deployment perspective, RISs are often regarded as low-power, passive, or nearly passive infrastructures. However, large-scale deployment still requires materials, installation, maintenance, and power supply. Large LEO constellations also raise sustainability concerns, including launch-related emissions, orbital congestion, satellite lifetime, space debris, and end-of-life disposal. Therefore, the localization performance gains should be carefully balanced against infrastructure cost, energy consumption, and environmental impact.

Bibliography

[1] E. Kaplan and C. Hegarty, *Understanding GPS/GNSS: Principles and Applications*, 3rd ed. Norwood, MA, USA: Artech House, 2017.

[2] H. K. Dureppagari, C. Saha, H. S. Dhillon, and R. M. Buehrer, “NTN-based 6G localization: Vision, role of LEOs, and open problems,” *IEEE Wireless Communications*, vol. 30, no. 6, pp. 44–51, 2023, doi: 10.1109/MWC.007.2300224.

[3] F. S. Prol *et al.*, “Position, navigation, and timing (PNT) through low Earth orbit (LEO) satellites: A survey on current status, challenges, and opportunities,” *IEEE Access*, vol. 10, pp. 83971–84002, 2022, doi: 10.1109/ACCESS.2022.3194050.

[4] R. T. Ioannides, T. Pany, and G. Gibbons, “Known vulnerabilities of global navigation satellite systems, status, and potential mitigation techniques,” *Proceedings of the IEEE*, vol. 104, no. 6, pp. 1174–1194, 2016, doi: 10.1109/JPROC.2016.2535898.

[5] L. Meng, L. Yang, W. Yang, and L. Zhang, “A survey of GNSS spoofing and anti-spoofing technology,” *Remote Sensing*, vol. 14, no. 19, Art. no. 4826, 2022, doi: 10.3390/rs14194826.

[6] T. G. R. Reid, A. M. Neish, T. Walter, and P. K. Enge, “Broadband LEO constellations for navigation,” *NAVIGATION*, vol. 65, no. 2, pp. 205–220, 2018, doi: 10.1002/navi.234.

[7] J. J. Khalife and Z. M. Kassas, “Receiver design for Doppler positioning with LEO satellites,” in *Proc. IEEE International Conference on Acoustics, Speech and Signal Processing (ICASSP)*, 2019, pp. 5506–5510, doi: 10.1109/ICASSP.2019.8682554.

[8] A. Behravan, V. Yajnanarayana, M. F. Keskin, H. Chen, D. Shrestha, T. E. Abrudan, T. Svensson, K. Schindhelm, A. Wolfgang, S. Lindberg, and H. Wymeersch, “Positioning and sensing in 6G: Gaps, challenges, and opportunities,” *IEEE Vehicular Technology Magazine*, vol. 18, no. 1, pp. 40–48, 2023, doi: 10.1109/MVT.2022.3219999.

[9] H. Chen, M. F. Keskin, A. Sakhnini, N. Decarli, S. Pollin, D. Dardari, and H. Wymeersch, “6G localization and sensing in the near field: Features, opportunities, and challenges,” *IEEE Wireless Communications*, vol. 31, no. 4, pp. 260–267, 2024, doi: 10.1109/MWC.011.2300359.

[10] W. Saad, M. Bennis, and M. Chen, “A vision of 6G wireless systems: Applications, trends, technologies, and open research problems,” *IEEE Network*, vol. 34, no. 3, pp. 134–142, 2020, doi: 10.1109/MNET.001.1900287.

[11] X. You *et al.*, “Towards 6G wireless communication networks: Vision, enabling technologies, and new paradigm shifts,” *Science China Information Sciences*, vol. 64, no. 1, Art. no. 110301, 2021.

[12] G. Araniti, A. Iera, S. Pizzi, and F. Rinaldi, “Toward 6G non-terrestrial networks,” *IEEE Network*, vol. 36, no. 1, pp. 113–120, 2022, doi: 10.1109/MNET.011.2100191.

[13] F. Rinaldi, H.-L. Maattanen, J. Torsner, S. Pizzi, S. Andreev, A. Iera, Y. Koucheryavy, and G. Araniti, “Non-terrestrial networks in 5G & beyond: A survey,” *IEEE Access*, vol. 8, pp. 165178–165200, 2020, doi: 10.1109/ACCESS.2020.3022981.

[14] M. Giordani and M. Zorzi, “Non-terrestrial networks in the 6G era: Challenges and opportunities,” *IEEE Network*, vol. 35, no. 2, pp. 244–251, 2021, doi: 10.1109/MNET.011.2000493.

[15] H. Sallouha, S. Saleh, S. De Bast, Z. Cui, S. Pollin, and H. Wymeersch, “On the ground and in the sky: A tutorial on radio localization in ground-air-space networks,” *IEEE Communications Surveys & Tutorials*, vol. 27, no. 1, pp. 218–258, 2025, doi: 10.1109/COMST.2024.3417336.

[16] 3GPP, “Solutions for NR to support Non-Terrestrial Networks (NTN),” 3GPP TR 38.821, V16.2.0, Release 16, archive file: 38821-g20.zip, Apr. 2023.

[17] D.-R. Emenonye, H. S. Dhillon, and R. M. Buehrer, “Fundamentals of LEO-based localization,” *IEEE Transactions on Information Theory*, vol. 71, no. 7, pp. 5277–5311, 2025, doi: 10.1109/TIT.2025.3567037.

[18] A. Umer, I. Müürsepp, M. M. Alam, and H. Wymeersch, “Reconfigurable intelligent surfaces in 6G radio localization: A survey of recent developments, opportunities, and challenges,” *IEEE Communications Surveys & Tutorials*, vol. 27, no. 6, pp. 3526–3560, 2025, doi: 10.1109/COMST.2025.3536517.

[19] C. E. Worka, F. A. Khan, Q. Z. Ahmed, P. Sureephong, and T. Alade, “Reconfigurable intelligent surface (RIS)-assisted non-terrestrial network (NTN)-based 6G communications: A contemporary survey,” *Sensors*, vol. 24, no. 21, Art. no. 6958, 2024, doi: 10.3390/s24216958.

[20] M. Di Renzo *et al.*, “Smart radio environments empowered by reconfigurable intelligent surfaces: How it works, state of research, and the road ahead,” *IEEE Journal on Selected Areas in Communications*, vol. 38, no. 11, pp. 2450–2525, 2020, doi: 10.1109/JSAC.2020.3007211.

[21] Q. Wu and R. Zhang, “Intelligent reflecting surface enhanced wireless network via joint active and passive beamforming,” *IEEE Transactions on Wireless Communications*, vol. 18, no. 11, pp. 5394–5409, 2019, doi: 10.1109/TWC.2019.2936025.

[22] Q. Wu, S. Zhang, B. Zheng, C. You, and R. Zhang, “Intelligent reflecting surface-aided wireless communications: A tutorial,” *IEEE Transactions on Communications*, vol. 69, no. 5, pp. 3313–3351, 2021, doi: 10.1109/TCOMM.2021.3051897.

[23] S. Saleh, M. F. Keskin, B. Priyanto, M. Beale, P. Zheng, T. Y. Al-Naffouri, G. Seco-Granados, and H. Wymeersch, “6G RIS-aided single-LEO localization with slow and fast Doppler effects,” in *Proc. 2024 IEEE Globecom Workshops (GC Wkshps)*, 2024, pp. 1–7, doi: 10.1109/GCWkshp64532.2024.11100939.

[24] K. Keykhosravi, M. F. Keskin, G. Seco-Granados, P. Popovski, and H. Wymeersch, "RIS-enabled SISO localization under user mobility and spatial-wideband effects," *IEEE Journal of Selected Topics in Signal Processing*, vol. 16, no. 5, pp. 1125–1140, 2022, doi: 10.1109/JSTSP.2022.3175036.

[25] J. He, H. Wymeersch, and M. Juntti, "Channel estimation for RIS-aided mmWave MIMO systems via atomic norm minimization," *IEEE Transactions on Wireless Communications*, vol. 20, no. 9, pp. 5786–5797, 2021, doi: 10.1109/TWC.2021.3070064.

[26] H. Wymeersch, G. Seco-Granados, G. Destino, D. Dardari, and F. Tufvesson, "5G mmWave positioning for vehicular networks," *IEEE Wireless Communications*, vol. 24, no. 6, pp. 80–86, 2017, doi: 10.1109/MWC.2017.1600374.

[27] Y. Liu, S. Zhang, F. Gao, J. Tang, and O. A. Dobre, "Cascaded channel estimation for RIS assisted mmWave MIMO transmissions," *IEEE Wireless Communications Letters*, vol. 10, no. 9, pp. 2065–2069, 2021, doi: 10.1109/LWC.2021.3092147.

[28] M. Neinavaie, J. Khalife, and Z. M. Kassas, "Acquisition, Doppler tracking, and positioning with Starlink LEO satellites: First results," *IEEE Transactions on Aerospace and Electronic Systems*, vol. 58, no. 3, pp. 2606–2610, 2022, doi: 10.1109/TAES.2021.3127488.

[29] J. Khalife, M. Neinavaie, and Z. M. Kassas, "The first carrier phase tracking and positioning results with Starlink LEO satellite signals," *IEEE Transactions on Aerospace and Electronic Systems*, vol. 58, no. 2, pp. 1487–1491, 2022, doi: 10.1109/TAES.2021.3113880.

[30] T. G. Reid, A. M. Neish, T. F. Walter, and P. K. Enge, "Leveraging commercial broadband LEO constellations for navigating," in *Proc. 29th Int. Tech. Meeting Satell. Div. Inst. Navigat. (ION GNSS+)*, Portland, OR, USA, 2016, pp. 2016–2016.

[31] F. S. Prol *et al.*, "Position, navigation, and timing (PNT) through low earth orbit (LEO) satellites: A survey on current status, challenges, and opportunities," *IEEE Access*, vol. 10, pp. 83971–84002, 2022.

[32] T. Reid *et al.*, "PULSAR: A new generation of commercial satellite navigation," in *Proc. ION GNSS+*, 2022, pp. 11–15.

[33] J. Yuan *et al.*, "Impact of attitude model, phase wind-up and phase center variation on precise orbit and clock offset determination of GRACE-FO and CentiSpace-1," *Remote Sens.*, vol. 13, no. 13, p. 2636, 2021.

[34] P. Zheng, X. Liu, Y. Zhang, J. He, G. Seco-Granados, and T. Y. Al-Naffouri, "LEO satellite and RIS: Two keys to seamless indoor and outdoor localization," *arXiv preprint arXiv:2312.16946*, 2023.

[35] H. Wymeersch and B. Denis, "Beyond 5G wireless localization with reconfigurable intelligent surfaces," in *Proc. IEEE International Conference on Communications (ICC)*, 2020, pp. 1–6, doi: 10.1109/ICC40277.2020.9148744.

[36] T. Ma, Y. Xiao, X. Lei, L. Zhang, Y. Niu, and G. K. Karagiannidis, "Reconfigurable intelligent surface assisted localization: Technologies, challenges, and the road ahead," *IEEE Open J. Commun. Soc.*, vol. 4, pp. 1430–1451, 2023.

[37] A. Fascista, M. F. Keskin, A. Coluccia, H. Wymeersch, and G. Seco-Granados, "RIS-aided joint localization and synchronization with a single-antenna re-

ceiver: Beamforming design and low-complexity estimation," *IEEE Journal of Selected Topics in Signal Processing*, vol. 16, no. 5, pp. 1141–1156, 2022, doi: 10.1109/JSTSP.2022.3177925.

[38] P. Zheng, X. Liu, and T. Y. Al-Naffouri, "LEO- and RIS-empowered user tracking: A Riemannian manifold approach," *IEEE Journal on Selected Areas in Communications*, vol. 42, no. 12, pp. 3445–3461, Dec. 2024, doi: 10.1109/JSAC.2024.3459074.

[39] H. Chen, P. Zheng, M. F. Keskin, T. Al-Naffouri, and H. Wymeersch, "Multi-RIS-enabled 3D sidelink positioning," *IEEE Transactions on Wireless Communications*, vol. 23, no. 8, pp. 8700–8716, 2024, doi: 10.1109/TWC.2024.3353387.

[40] B. Zheng and R. Zhang, "Intelligent reflecting surface-enhanced OFDM: Channel estimation and reflection optimization," *IEEE Wireless Communications Letters*, vol. 9, no. 4, pp. 518–522, 2020, doi: 10.1109/LWC.2019.2961357.

[41] S. W. Ellingson, "Path Loss in Reconfigurable Intelligent Surface-Enabled Channels," in *2021 IEEE 32nd Annual International Symposium on Personal, Indoor and Mobile Radio Communications (PIMRC)*, 2021, pp. 829–835, doi: 10.1109/PIMRC50174.2021.9569465.

[42] F. Wen, H. Wymeersch, B. Peng, W. P. Tay, H. C. So, and D. Yang, "A survey on 5G massive MIMO localization," *Digital Signal Processing*, vol. 94, pp. 21–28, 2019, doi: 10.1016/j.dsp.2019.05.005.

A

Appendix 1

A.1 Numerical Checks for Modelling Assumptions

This appendix provides numerical checks for the main modelling assumptions used in the simulation. The purpose is not to prove that the assumptions hold in all possible deployment scenarios, but to verify that they are reasonable under the parameters used in this thesis.

A.1.1 Observation-Window Duration

The observation duration is determined by the number of OFDM symbols and the OFDM symbol duration. In the simulation, the total symbol duration including CP is

$$T_{\text{sym}} = 1.07T = 71.33\ \mu\text{s}. \tag{A.1}$$

Therefore, the total observation-window duration is

$$T_{\text{obs}} = LT_{\text{sym}} = 256 \times 71.33\ \mu\text{s} \approx 18.26\ \text{ms}. \tag{A.2}$$

For example, a low-mobility user moving at 1.83 cm within one observation block.

$$\Delta d_{\text{u}} = v_{\text{u}} T_{\text{obs}} = 1 \times 18.26\ \text{ms} \approx 1.83\ \text{cm} \tag{A.3}$$

The induced propagation-delay perturbation is upper bounded by

$$\Delta\tau_{\text{u}} \leq \frac{\Delta d_{\text{u}}}{c} = \frac{1.83 \times 10^{-2}}{3 \times 10^{8}} \approx 6.1 \times 10^{-11}\ \text{s} = 0.061\ \text{ns}. \tag{A.4}$$

This value is much smaller than the delay resolution 33.3 ns, so the UE motion within one estimation window has a negligible impact on the range, Doppler, and angular parameters, and the UE position can be treated as constant within one observation block.

A.1.2 Satellite Displacement During One Observation Window

The LEO satellite velocity in the considered setup is approximately $\|\mathbf{v}_{\text{sat}}\| \approx 8.11$ km/s. During one observation window, the satellite position displacement is therefore bounded by

$$\Delta d_{\text{sat}} = \|\mathbf{v}_{\text{sat}}\| T_{\text{obs}} \approx 8.11 \times 10^{3} \times 18.26 \times 10^{-3} \approx 148.1\ \text{m}. \tag{A.5}$$

The satellite displacement Δd_{sat} is small compared with the satellite distance, so the satellite velocity can be approximated as constant during one block.

$$\frac{\Delta d_{\text{sat}}}{d_{\text{sat}}} \approx \frac{148.1}{8.15 \times 10^5} \approx 1.82 \times 10^{-4} \tag{A.6}$$

A conservative upper bound on the angular variation of LEO satellites caused by this displacement can be written as

$$\Delta\psi_{\text{sat}} \lesssim \frac{\Delta d_{\text{sat}}}{d_{\text{sat}}} \approx \frac{148.1}{8.15 \times 10^5} \approx 1.82 \times 10^{-4} \text{ rad} \approx 0.010^\circ, \tag{A.7}$$

In the simulation, the initial angular search range is $\pm 45^\circ$ with $GridSize = 11$, leading to an initial angular grid spacing of

$$\Delta_{\text{AOD},0} = \frac{2 \times 45^\circ}{11 - 1} = 9^\circ. \tag{A.8}$$

After recursive grid refinement with $ctrThr = 10$, the last evaluated angular grid spacing becomes

$$\Delta_{\text{AOD,final}} = \frac{9^\circ}{2^9} \approx 0.0176^\circ. \tag{A.9}$$

$$\frac{\Delta\psi_{\text{sat}}}{\Delta_{\text{AOD,final}}} \approx \frac{0.010^\circ}{0.0176^\circ} \approx 0.57. \tag{A.10}$$

Hence, the satellite-induced angular variation within one observation block is smaller than one final angular grid interval of the MLE refinement. Moreover, it is much smaller than the initial angular search spacing of 9°. Therefore, the satellite-to-RIS angular variation is not resolved as a separate angular change within one estimation window, and it is reasonable to treat the satellite-to-RIS angle as approximately constant over one observation block.

A.1.3 Far-field of the RIS Array–UE

For the carrier frequency $f_c = 2$ GHz, the wavelength λ

$$\lambda = \frac{c}{f_c} = \frac{2.9979 \times 10^8}{2 \times 10^9} \approx 0.1499 \text{ m}. \tag{A.11}$$

Each RIS is a 10×10 uniform rectangular array with inter-element spacing $\lambda/2$. The side length of the active aperture is

$$D_{\text{side}} = (10 - 1)\frac{\lambda}{2} \approx 9 \times 0.07495 \approx 0.6745 \text{ m}. \tag{A.12}$$

Using the side length as the aperture dimension, the Fraunhofer distance is

$$d_{\text{F,side}} = \frac{2D_{\text{side}}^2}{\lambda} \approx \frac{2(0.6745)^2}{0.1499} \approx 6.07 \text{ m}. \tag{A.13}$$

A more conservative choice is to use the diagonal aperture,

$$D_{\text{diag}} = \sqrt{2}D_{\text{side}} \approx 0.954 \text{ m}. \tag{A.14}$$

The corresponding Fraunhofer distance becomes

$$d_{\mathrm{F,diag}} = \frac{2D_{\mathrm{diag}}^2}{\lambda} \approx \frac{2(0.954)^2}{0.1499} \approx 12.1 \text{ m}. \tag{A.15}$$

In the simulation, the UE is located at $\mathbf{p} = [0, 10, 1.5]^T$ m, while the two RISs are located at $\mathbf{p}_{\mathrm{RIS},1} = [4, 0, 10]^T$ m and $\mathbf{p}_{\mathrm{RIS},2} = [-4, 0, 10]^T$ m. Thus,

$$d_{\mathrm{ru},1} = \|\mathbf{p} - \mathbf{p}_{\mathrm{RIS},1}\| = \sqrt{4^2 + 10^2 + 8.5^2} \approx 13.72 \text{ m}, \tag{A.16}$$

$$d_{\mathrm{ru},2} \approx 13.72 \text{ m}. \tag{A.17}$$

Both distances are larger than the conservative diagonal-aperture Fraunhofer distance $d_{\mathrm{F,diag}}$. Therefore, the far-field plane-wave model is suitable for the simulations for RIS–UE paths.

A.1.4 Doppler approximation between LoS and RIS Paths

In the considered simulation geometry, the UE position is

$$\mathbf{p}_{\mathrm{u}} = [0, 10, 1.5]^T \text{ m}, \tag{A.18}$$

and the two RISs are located at

$$\mathbf{p}_{\mathrm{RIS},1} = [4, 0, 10]^T \text{ m}, \qquad \mathbf{p}_{\mathrm{RIS},2} = [-4, 0, 10]^T \text{ m}. \tag{A.19}$$

For the satellite setting with $\theta_{\mathrm{el}} = 45°$, $\theta_{\mathrm{az}} = 90°$, and $h = 600$ km, the orbit function gives

$$\mathbf{p}_{\mathrm{sat}} \approx [0,\ 5.761499 \times 10^5,\ 5.761499 \times 10^5]^T \text{ m}, \tag{A.20}$$

and

$$\mathbf{v}_{\mathrm{sat}} \approx [0,\ -8.083376 \times 10^3,\ 6.703809 \times 10^2]^T \text{ m/s}. \tag{A.21}$$

The speed of light is $c = 2.9979 \times 10^8$ m/s, and the normalized carrier-frequency offset is $\delta_f = 10^{-6}$.
For the LoS satellite–UE path, the propagation distance vector is

$$\mathbf{d}_{\mathrm{su}} = \mathbf{p}_{-}\mathbf{p}_{\mathrm{sat}} \approx [0,\ -5.76140 \times 10^5,\ -5.76148 \times 10^5]^T \text{ m}. \tag{A.22}$$

The corresponding unit direction vector is

$$\mathbf{u}_{\mathrm{su}} = \frac{\mathbf{d}_{\mathrm{su}}}{\|\mathbf{d}_{\mathrm{su}}\|} \approx [0,\ -0.70710,\ -0.70711]^T. \tag{A.23}$$

Therefore, the geometric Doppler factor is

$$\frac{\mathbf{v}_{\mathrm{sat}}^T \mathbf{u}_{\mathrm{su}}}{c} = \frac{5241.73}{2.9979 \times 10^8} \approx 1.74845 \times 10^{-5}. \tag{A.24}$$

Including the common normalized CFO, the direct-path Doppler factor is

$$\nu_{\mathrm{su}} = \frac{\mathbf{v}_{\mathrm{sat}}^T \mathbf{u}_{\mathrm{su}}}{c} + \nu_{\mathrm{CFO}} \approx 1.84845 \times 10^{-5}. \tag{A.25}$$

For the satellite–RIS path, the propagation vector is

$$\mathbf{d}_{\mathrm{sr},1} = \mathbf{p}_{\mathrm{sat}} - \mathbf{p}_{\mathrm{RIS},1} \approx [-4,\ 5.761499 \times 10^5,\ 5.761399 \times 10^5]^T \text{ m.} \tag{A.26}$$

$$-\mathbf{u}_{\mathrm{sr},1} = -\frac{\mathbf{d}_{\mathrm{sr},1}}{\|\mathbf{d}_{\mathrm{sr},1}\|} \approx [4.91 \times 10^{-6},\ -0.7071129,\ -0.7071006]^T. \tag{A.27}$$

$$\nu_{\mathrm{sr},1} = \frac{\mathbf{v}_{\mathrm{sat}}^T(-\mathbf{u}_{\mathrm{sr},1})}{c} = \frac{5241.83}{2.9979 \times 10^8} \approx 1.74849 \times 10^{-5}. \tag{A.28}$$

Since the RIS and the UE are assumed static in the simulation, the RIS–UE branch only contains the common CFO, i.e.,

$$\nu_{\mathrm{ru},1} = \delta_f = 10^{-6}. \tag{A.29}$$

Therefore, the total Doppler factor of the first RIS-assisted path is

$$\nu_{\mathrm{sru},1} = \nu_{\mathrm{sr},1} + \nu_{\mathrm{ru},1} \approx 1.84849 \times 10^{-5}. \tag{A.30}$$

This small phase variation supports the use of approximately common Doppler compensation for the LoS and RIS branches in the considered geometry.

A.2 Details of the CRB Evaluation

This appendix provides the main derivatives used for the numerical evaluation of the CRB. The purpose is to make the mapping from the geometric state vector to the channel parameters explicit and to clarify the treatment of nuisance channel gains and MP components.

A.2.1 Signal Model and Channel-Parameter FIM

Let the noiseless received signal at the kth subcarrier and the lth OFDM symbol be written as

$$y_{k,l} = \alpha_0 z_{0,k,l} + \sum_{r=1}^{R} \alpha_r z_{r,k,l}, \tag{A.31}$$

where the index 0 denotes the direct satellite–UE LoS path and $r = 1, \ldots, R$ denotes the rth RIS-assisted path. Here, α_0 and α_r correspond to α_{su} and $\alpha_{\mathrm{sru},r}$, respectively. The LoS component is

$$z_{0,k,l} = x_{k,l} B_{0,k,l} C_{0,l}, \tag{A.32}$$

and the rth RIS-assisted component is

$$z_{r,k,l} = x_{k,l} B_{r,k,l} C_{r,l} G_{\mathrm{RIS},r,l}. \tag{A.33}$$

Here, $x_{k,l}$ is the pilot symbol, $B_{i,k,l}$ denotes the delay-related subcarrier phase term, $C_{i,l}$ denotes the Doppler-related phase term, and $G_{\mathrm{RIS},r,l}$ is the temporal response of the rth RIS.

The channel-parameter vector is defined as

$$\begin{aligned}\boldsymbol{\eta} = \Big[&\Re\{\alpha_0\}, \Im\{\alpha_0\}, \dots, \Re\{\alpha_R\}, \Im\{\alpha_R\},\\ &\tau_{\text{su}}, \tau_{\text{sru},1}, \dots, \tau_{\text{sru},R},\\ &\nu_{\text{su}}, \nu_{\text{sru},1}, \dots, \nu_{\text{sru},R},\\ &\theta^{az}_{ru,1}, \theta^{el}_{ru,1}, \dots, \theta^{az}_{ru,R}, \theta^{el}_{ru,R}\Big]^T.\end{aligned} \tag{A.34}$$

The complex path gains are included as unknown nuisance parameters. Thus, the final position bound accounts for the uncertainty of the channel gains rather than assuming that the gains are perfectly known.
Assuming circularly symmetric complex Gaussian noise with variance σ^2, the Fisher information matrix of $\boldsymbol{\eta}$ is

$$[\mathbf{I}_\eta]_{a,b} = \frac{2}{\sigma^2}\Re\left\{\sum_{k=0}^{K-1}\sum_{l=0}^{L-1}\left(\frac{\partial y_{k,l}}{\partial \eta_a}\right)^* \frac{\partial y_{k,l}}{\partial \eta_b}\right\}. \tag{A.35}$$

The derivatives with respect to the real and imaginary parts of the complex gain are

$$\frac{\partial y_{k,l}}{\partial \Re\{\alpha_i\}} = z_{i,k,l}, \qquad \frac{\partial y_{k,l}}{\partial \Im\{\alpha_i\}} = \jmath z_{i,k,l}. \tag{A.36}$$

With the phase convention used in the implemented signal model, the delay derivative is

$$\frac{\partial y_{k,l}}{\partial \tau_i} = -\jmath 2\pi k\Delta f\, \alpha_i z_{i,k,l}. \tag{A.37}$$

The Doppler derivative is

$$\frac{\partial y_{k,l}}{\partial \nu_i} = \jmath 2\pi(f_c + k\Delta f)lT_{\text{sym}}\, \alpha_i z_{i,k,l}. \tag{A.38}$$

The factor $(f_c + k\Delta f)$ reflects that the implementation includes both the carrier Doppler phase and the subcarrier-dependent wideband Doppler phase.
Similarly, the known incident unit vector from the rth RIS to the satellite is

$$\mathbf{u}_{rs,r} = \frac{\mathbf{p}_{\text{sat}} - \mathbf{p}_{R,r}}{\|\mathbf{p}_{\text{sat}} - \mathbf{p}_{R,r}\|}. \tag{A.39}$$

Since the RIS array response is evaluated in the local coordinate system of the RIS, the GCS unit vectors are transformed by $\mathbf{R}_r^T$. The local incident and outgoing directions are therefore

$$\mathbf{u}'_{rs,r} = \mathbf{R}_r^T\mathbf{u}_{rs,r}, \qquad \mathbf{u}'_{ru,r} = \mathbf{R}_r^T\mathbf{u}_{ru,r}. \tag{A.40}$$

The temporal RIS response is modeled as

$$G_{\text{RIS},r,l} = \sum_{n=1}^{N_r} a^{\text{rx}}_{r,n} a^{\text{tx}}_{r,n}\omega_{r,n,l}, \tag{A.41}$$

where $\omega_{r,n,l}$ is the phase coefficient of the nth element of the rth RIS. The incident and outgoing steering terms are given by

$$a_{r,n}^{\text{rx}} = \exp\left(\jmath \frac{2\pi}{\lambda} \mathbf{p}_{r,n}^{T} \mathbf{u}_{rs,r}^{'}\right), \tag{A.42}$$

and

$$a_{r,n}^{\text{tx}} = \exp\left(\jmath \frac{2\pi}{\lambda} \mathbf{p}_{r,n}^{T} \mathbf{u}_{ru,r}^{'}\right), \tag{A.43}$$

where $\mathbf{p}_{r,n}$ denotes the position of the nth RIS element in the local coordinate system.
The derivatives of the GCS outgoing unit vector are

$$\frac{\partial \mathbf{u}_{ru,r}}{\partial \theta_{ru,r}^{az}} = \begin{bmatrix} -\cos\theta_{ru,r}^{el} \sin\theta_{ru,r}^{az} \\ \cos\theta_{ru,r}^{el} \cos\theta_{ru,r}^{az} \\ 0 \end{bmatrix}, \tag{A.44}$$

and

$$\frac{\partial \mathbf{u}_{ru,r}}{\partial \theta_{ru,r}^{el}} = \begin{bmatrix} -\sin\theta_{ru,r}^{el} \cos\theta_{ru,r}^{az} \\ -\sin\theta_{ru,r}^{el} \sin\theta_{ru,r}^{az} \\ \cos\theta_{ru,r}^{el} \end{bmatrix}. \tag{A.45}$$

Since $\mathbf{u}_{ru,r}^{'} = \mathbf{R}_r^T \mathbf{u}_{ru,r}$, its derivatives are

$$\frac{\partial \mathbf{u}_{ru,r}^{'}}{\partial \chi} = \mathbf{R}_r^T \frac{\partial \mathbf{u}_{ru,r}}{\partial \chi}, \qquad \chi \in \{\theta_{ru,r}^{az}, \theta_{ru,r}^{el}\}. \tag{A.46}$$

The derivative of the RIS response is

$$\begin{aligned} \frac{\partial G_{\text{RIS},r,l}}{\partial \chi} = & \sum_{n=1}^{N_r} a_{r,n}^{\text{rx}} a_{r,n}^{\text{tx}} \omega_{r,n,l} \\ & \times \jmath \frac{2\pi}{\lambda} \mathbf{p}_{r,n}^{T} \frac{\partial \mathbf{u}_{ru,r}^{'}}{\partial \chi}, \qquad \chi \in \{\theta_{ru,r}^{az}, \theta_{ru,r}^{el}\}. \end{aligned} \tag{A.47}$$

The received-signal derivatives with respect to the RIS angular parameters are then

$$\frac{\partial y_{k,l}}{\partial \theta_{ru,r}^{az}} = \alpha_r x_{k,l} B_{r,k,l} C_{r,l} \frac{\partial G_{\text{RIS},r,l}}{\partial \theta_{ru,r}^{az}}, \tag{A.48}$$

and

$$\frac{\partial y_{k,l}}{\partial \theta_{ru,r}^{el}} = \alpha_r x_{k,l} B_{r,k,l} C_{r,l} \frac{\partial G_{\text{RIS},r,l}}{\partial \theta_{ru,r}^{el}}. \tag{A.49}$$

The MP paths generated by the scatter points are included in the received-signal simulation. For example, the direct MP path uses $\tau_{su,m}$ and $\nu_{su,m}$, while the RIS-related MP path uses $\tau_{sru,r,m}$ and $\nu_{sru,r,m}$. However, these MP delays, Doppler factors, angles, and gains are not explicitly included as nuisance parameters in $\boldsymbol{\eta}$. Instead, their average received power is incorporated into an effective noise variance:

$$\sigma_{\text{eff}}^2 = \sigma^2 + P_{\text{MP,avg}}, \tag{A.50}$$

Therefore, the effective channel-domain FIM under MP is computed by replacing σ^2 with σ^2_{eff}:

$$[\mathbf{I}_\eta^{\text{eff}}]_{a,b} = \frac{2}{\sigma^2_{\text{eff}}} \Re \left\{ \sum_{k=0}^{K-1} \sum_{l=0}^{L-1} \left(\frac{\partial y_{k,l}}{\partial \eta_a} \right)^* \frac{\partial y_{k,l}}{\partial \eta_b} \right\}. \tag{A.51}$$

The channel-domain CRB and the effective channel-domain CRB are obtained as

$$\mathbf{C}_\eta = \mathbf{I}_\eta^{-1}, \qquad \mathbf{C}_\eta^{\text{eff}} = \left(\mathbf{I}_\eta^{\text{eff}} \right)^{-1}. \tag{A.52}$$

The delay, Doppler, and angular error bounds are extracted from the diagonal entries of $\mathbf{C}_\eta$ or $\mathbf{C}_\eta^{\text{eff}}$.

A.2.2 State-to-Channel Jacobian

The positioning-related state vector is defined as

$$\begin{aligned} \mathbf{s} = \Big[&\Re\{\alpha_0\}, \Im\{\alpha_0\}, \ldots, \Re\{\alpha_R\}, \Im\{\alpha_R\}, \\ &p_x, p_y, p_z, \delta, \delta_f \Big]^T, \end{aligned} \tag{A.53}$$

where $\mathbf{p} = [p_x, p_y, p_z]^T$ is the UE position, δ is the receiver clock bias, and δ_f is the normalized CFO. The dependence of the channel parameters on the positioning-related state variables is characterized by the state-to-channel Jacobian matrix

$$\mathbf{J} = \frac{\partial \boldsymbol{\eta}}{\partial \mathbf{s}}. \tag{A.54}$$

The gain-related part of $\mathbf{J}$ is an identity matrix, since the real and imaginary parts of the path gains are included in both $\boldsymbol{\eta}$ and $\mathbf{s}$ as nuisance parameters.
Let $\mathbf{p}_{\text{sat}}$ and $\mathbf{v}_{\text{sat}}$ denote the instantaneous satellite position and velocity within the short observation interval. For the direct path, define

$$\mathbf{d}_{\text{su}} = \mathbf{p} - \mathbf{p}_{\text{sat}}, \qquad d_{\text{su}} = \|\mathbf{d}_{\text{su}}\|, \qquad \mathbf{e}_{\text{su}} = \frac{\mathbf{d}_{\text{su}}}{d_{\text{su}}}. \tag{A.55}$$

The direct-path delay and Doppler are

$$\tau_{\text{su}} = \frac{d_{\text{su}}}{c} + \delta, \tag{A.56}$$

and

$$\nu_{\text{su}} = \frac{\mathbf{v}_{\text{sat}}^T \mathbf{e}_{\text{su}}}{c} + \delta_f. \tag{A.57}$$

Their derivatives are

$$\frac{\partial \tau_{\text{su}}}{\partial \mathbf{p}} = \frac{1}{c} \mathbf{e}_{\text{su}}^T, \qquad \frac{\partial \tau_{\text{su}}}{\partial \delta} = 1, \tag{A.58}$$

and

$$\frac{\partial \nu_{\text{su}}}{\partial \mathbf{p}} = \frac{1}{c d_{\text{su}}} \mathbf{v}_{\text{sat}}^T \left(\mathbf{I}_3 - \mathbf{e}_{\text{su}} \mathbf{e}_{\text{su}}^T \right), \qquad \frac{\partial \nu_{\text{su}}}{\partial \delta_f} = 1. \tag{A.59}$$

For the rth RIS-assisted path, define

$$d_{\text{sr},r} = \|\mathbf{p}_{\text{sat}} - \mathbf{p}_{R,r}\|, \qquad \mathbf{d}_{\text{ru},r} = \mathbf{p} - \mathbf{p}_{R,r}, \tag{A.60}$$

and

$$d_{\mathrm{ru},r} = \|\mathbf{d}_{\mathrm{ru},r}\|, \qquad \mathbf{e}_{\mathrm{ru},r} = \frac{\mathbf{d}_{\mathrm{ru},r}}{d_{\mathrm{ru},r}}. \tag{A.61}$$

The RIS-assisted delay is

$$\tau_{\mathrm{sru},r} = \frac{d_{\mathrm{sr},r} + d_{\mathrm{ru},r}}{c} + \delta. \tag{A.62}$$

Since $d_{\mathrm{sr},r}$ is independent of the UE position, the derivatives are

$$\frac{\partial \tau_{\mathrm{sru},r}}{\partial \mathbf{p}} = \frac{1}{c}\mathbf{e}_{\mathrm{ru},r}^T, \qquad \frac{\partial \tau_{\mathrm{sru},r}}{\partial \delta} = 1. \tag{A.63}$$

According to the Doppler model used in this work, the RIS-branch Doppler is

$$\nu_{\mathrm{sru},r} = -\frac{\mathbf{v}_{\mathrm{sat}}^T \mathbf{u}_{rs,r}}{c} + \delta_f, \tag{A.64}$$

where $\mathbf{u}_{rs,r}$ is the GCS unit vector from the rth RIS to the satellite. For a given satellite–RIS geometry, $\mathbf{u}_{rs,r}$ is known and does not depend on the UE position. Therefore,

$$\frac{\partial \nu_{\mathrm{sru},r}}{\partial \mathbf{p}} = \mathbf{0}_{1\times 3}, \qquad \frac{\partial \nu_{\mathrm{sru},r}}{\partial \delta_f} = 1. \tag{A.65}$$

For the GCS RIS-to-UE angular parameters, define

$$\Delta \mathbf{p}_{\mathrm{ru},r} = \mathbf{p} - \mathbf{p}_{R,r} = [\Delta x_r, \Delta y_r, \Delta z_r]^T. \tag{A.66}$$

Let

$$\rho_r = \sqrt{\Delta x_r^2 + \Delta y_r^2}, \qquad d_{\mathrm{ru},r} = \|\Delta \mathbf{p}_{\mathrm{ru},r}\|. \tag{A.67}$$

The GCS azimuth and elevation angles are

$$\theta_{ru,r}^{az} = \mathrm{atan2}\left(\Delta y_r, \Delta x_r\right), \tag{A.68}$$

and

$$\theta_{ru,r}^{el} = \sin^{-1}\left(\frac{\Delta z_r}{d_{\mathrm{ru},r}}\right). \tag{A.69}$$

Their derivatives with respect to the UE position are

$$\frac{\partial \theta_{ru,r}^{az}}{\partial \mathbf{p}} = \frac{1}{\rho_r^2}\begin{bmatrix} -\Delta y_r & \Delta x_r & 0 \end{bmatrix}, \tag{A.70}$$

and

$$\frac{\partial \theta_{ru,r}^{el}}{\partial \mathbf{p}} = \frac{1}{d_{\mathrm{ru},r}^2 \rho_r}\begin{bmatrix} -\Delta x_r \Delta z_r & -\Delta y_r \Delta z_r & \rho_r^2 \end{bmatrix}. \tag{A.71}$$

The derivatives of $\theta_{ru,r}^{az}$ and $\theta_{ru,r}^{el}$ with respect to δ and δ_f are zero.
Using the above derivatives, the state-domain FIM is obtained by

$$\mathbf{I}_s = \mathbf{J}^T \mathbf{I}_\eta \mathbf{J}. \tag{A.72}$$

The state-domain covariance lower bound is

$$\mathbf{C}_s = \mathbf{I}_s^{-1}. \tag{A.73}$$

The position error bound, the clock-bias error bound, and the CFO error bound are given by

$$\mathrm{PEB} = \sqrt{\mathrm{tr}\left([\mathbf{C}_s]_{\mathbf{p},\mathbf{p}}\right)}, \qquad \mathrm{CEB} = \sqrt{[\mathbf{C}_s]_{\delta,\delta}}, \qquad \mathrm{FEB} = \sqrt{[\mathbf{C}_s]_{\delta_f,\delta_f}}. \tag{A.74}$$

When MP is present, the effective state-domain FIM is obtained using the same Jacobian matrix:

$$\mathbf{I}_s^{\mathrm{eff}} = \mathbf{J}^T \mathbf{I}_\eta^{\mathrm{eff}} \mathbf{J}. \tag{A.75}$$

The corresponding effective state-domain covariance lower bound is

$$\mathbf{C}_s^{\mathrm{eff}} = \left(\mathbf{I}_s^{\mathrm{eff}}\right)^{-1}. \tag{A.76}$$

The effective position error bound, clock-bias error bound, and CFO error bound are given by

$$\mathrm{PEB}_{\mathrm{eff}} = \sqrt{\mathrm{tr}\left([\mathbf{C}_s^{\mathrm{eff}}]_{\mathbf{p},\mathbf{p}}\right)}, \qquad \mathrm{CEB}_{\mathrm{eff}} = \sqrt{[\mathbf{C}_s^{\mathrm{eff}}]_{\delta,\delta}}, \qquad \mathrm{FEB}_{\mathrm{eff}} = \sqrt{[\mathbf{C}_s^{\mathrm{eff}}]_{\delta_f,\delta_f}}. \tag{A.77}$$

In the reported figures, delay-related bounds and clock-bias bounds are converted to meters by multiplying by c. Doppler-related and CFO bounds are reported in equivalent velocity units by multiplying by c.

DEPARTMENT OF ELECTRICAL ENGINEERING
CHALMERS UNIVERSITY OF TECHNOLOGY
Gothenburg, Sweden
www.chalmers.se

CHALMERS
UNIVERSITY OF TECHNOLOGY